Master's Thesis

Power Flow Decoupling Method in Three-Port and Four-Port Dual-Active-Bridge Converters for DC Microgrid Applications

Kwabena Opoku Bempah

Department of Electrical Engineering

Ulsan National Institute of Science and Technology

2022

Power Flow Decoupling Method in Three-Port and Four-Port Dual-Active-Bridge Converters for DC Microgrid Applications

Kwabena Opoku Bempah

Department of Electrical Engineering

Ulsan National Institute of Science and Technology

Power Flow Decoupling Method in Three-Port and Four-Port Dual-Active-Bridge Converters for DC Microgrid Applications

A thesis/dissertation submitted to
Ulsan National Institute of Science and Technology
in partial fulfillment of the
requirements for the degree of
Master of Science

Kwabena Opoku Bempah

07.01.2022
Approved by

Advisor

Jee-Hoon Jung

Power Flow Decoupling Method in Three-Port and Four-Port Dual-Active-Bridge Converters for DC Microgrid Applications

Kwabena Opoku Bempah

This certifies that the thesis/dissertation of Kwabena Opoku Bempah is approved.

07.01.2022

Signature

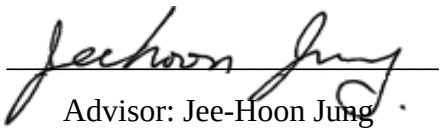

Advisor: Jee-Hoon Jung

Signature

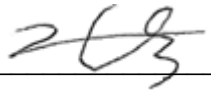

JinGook Kim

Signature

Se-Un Shin

Abstract

DC microgrid systems are gaining attention in recent times for microgrid developments because of associated advantages such as reduced conversion stages, eliminated harmonics, and easy integration of renewable energy resources. To further reduce conversion stages and improve system power density, multiport converters are adapted for DC microgrid applications. Two popular multiport converters being researched for DC microgrid developments are the three-port and four-port Dual-Active-Bridge (DAB) converters which are also referred to as the Triple-Active-Bridge (TAB) and Quadruple-Active-Bridge (QAB) converters. The two converters respectively comprise three and four active-bridge converters interconnected by single multi-winding transformers. The conventional TAB and QAB converter topologies adapt external leakage inductors at all ports which results in the coupling of all the ports. As a result, a change in the power condition of one controlled port affects the power condition in other controlled ports. Port coupling affects the converter's dynamic performance, and the application of the converter under such a condition in DC microgrids negatively affects the overall power balancing, stability, and efficiency of the DC microgrid. Therefore, a power flow decoupling method is proposed in this thesis for the three-port and four-port DAB converters to minimize port coupling for improved dynamic performance and improved DC microgrid performance.

Contents

List of Figures

List of Tables

List of Abbreviations

DAB	Dual-Active-Bridge
TAB	Triple-Active-Bridge
QAB	Quadruple-Active-Bridge
DSP	Digital Signal Processor
ESS	Energy Storage System
EV	Electric Vehicle
PI	Proportional-Integral
SPS	Single-Phase-Shift
LUT	Look-Up Table
SISO	Single-Input Single-Output
DIDO	Dual-Input Dual-Output
MIMO	Multiple-Input Multiple-Output
VSC	Voltage Source Converter

Ⅰ. Introduction

Energy is a key factor in global development and industrialization. The globe has seen a fast pace of industrialization in recent times and to keep up with this pace of growth, energy must be available and sustainable to match up to the energy demand. Microgrid systems are therefore developed to aid in energy generation and serve as backup systems in situations where utility grids are not able to meet energy demands or where they do not function properly due to faults. Microgrids ensure continuous power supply to local and sensitive loads at all grid conditions [1] and by aiding in energy supply to loads, utility grid congestion is reduced. Fig. 1.1 shows a conceptual diagram of a microgrid system.

DC microgrids are gaining attention in recent times as better alternatives to AC microgrids for microgrid development as they appear more advantageous. To generate clean and sustainable energy, renewable energy resources are highly considered for microgrid developments. DC microgrids are preferred for renewable energy integration since most renewable energy resources are DC in nature. DC microgrids are characterized by the absence of harmonics and reactive power and therefore, there is no need to compensate for harmonics or control reactive power [2],[3]. Most household loads are also DC in nature and hence they can be directly connected in DC microgrids, reducing conversion stages by eliminating DC-AC converters as opposed to AC microgrids. Reducing conversion stages leads to low cost on converters and the elimination of reactive current losses leads to high transmission efficiency. In addition, DC microgrids do not require grid synchronization as opposed to the case of AC microgrids [4]. Fig. 1.2 and Fig. 1.3 show conceptual diagrams of an AC microgrid and a DC microgrid, respectively, and they depict conversion stages required when integrating renewable energy sources and DC loads.

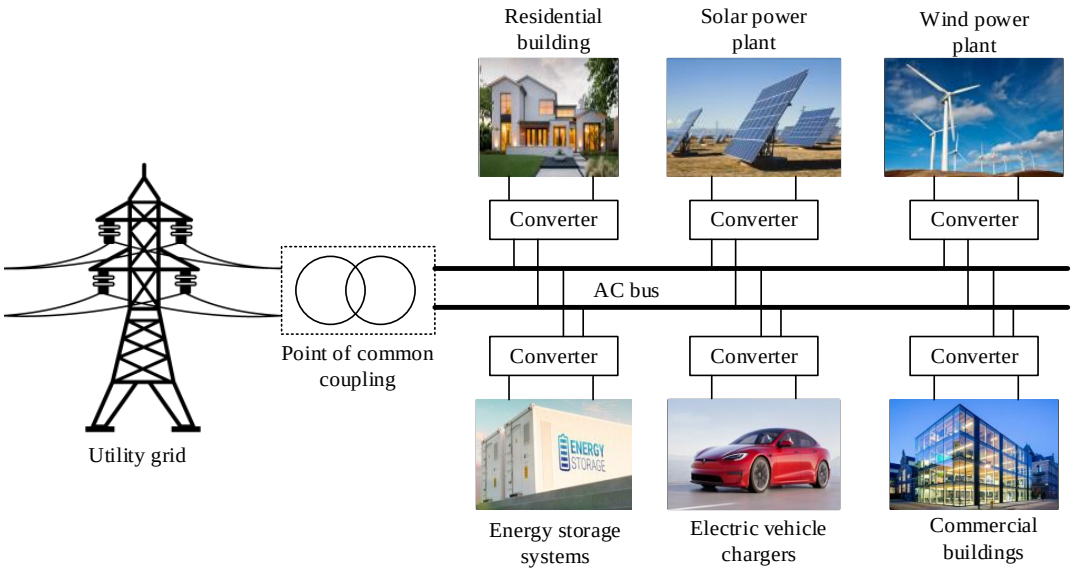

Fig. 1.1 Structure of a conventional microgrid system

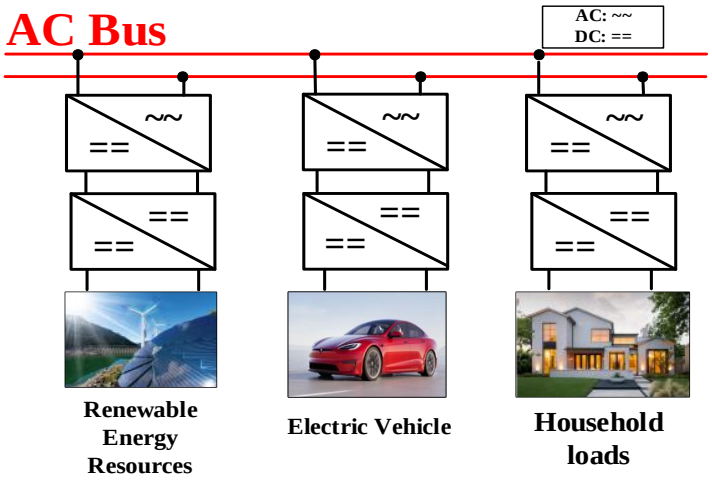

Fig. 1.2 A conceptual diagram of an AC microgrid

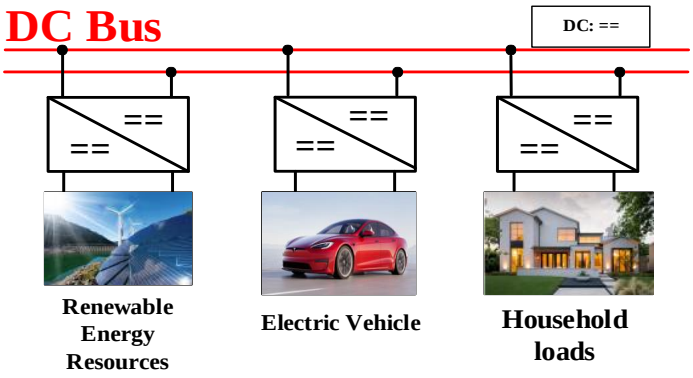

Fig. 1.3 A conceptual diagram of a DC microgrid

To further reduce conversion stages in DC microgrid systems, multi-port converters are considered for integration in DC microgrid implementation. A multiport converter connects two or more energy sources, loads, or combinations while utilizing a single power conversion stage. Two of the popular multiport converters being researched for integration into DC microgrids are the Triple-Active-Bridge (TAB) converter and the Quadruple-Active-Bridge (QAB) converter. The two converters are extensions of the Dual-Active-Bridge (DAB) converter shown in Fig. 1.4 and hence are characterized by features such as bidirectional power flow, galvanic isolation, high conversion efficiency, and high-power density [5],[6],[7]. A conceptual diagram of the conventional DC microgrid system is shown in Fig. 1.5 and a conceptual diagram DC microgrid that integrates a TAB converter and a QAB converter is shown in Fig. 1.6. The conventional TAB converter and QAB converter topologies respectively adapt three and four external bulk inductors for power transfer among ports via a single multi-winding transformer. The transformer's windings together with the external inductors, result in port coupling and coupled power flows. Due to the coupled power flows, a change in the power condition of a controlled port affects the power condition of other controlled ports and this affects power balancing, stability, efficiency, and the

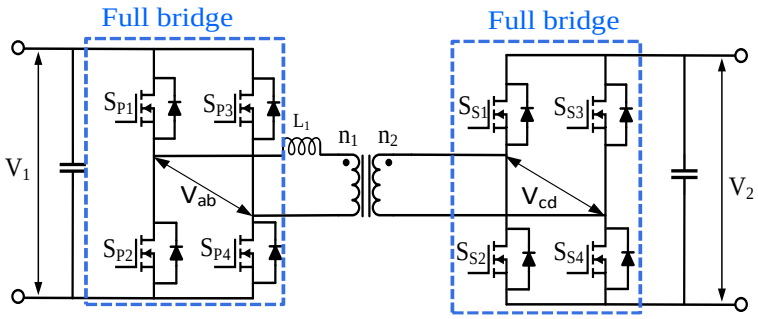

Fig. 1.4 Full circuit of the Dual-Active-Bridge (DAB) converter

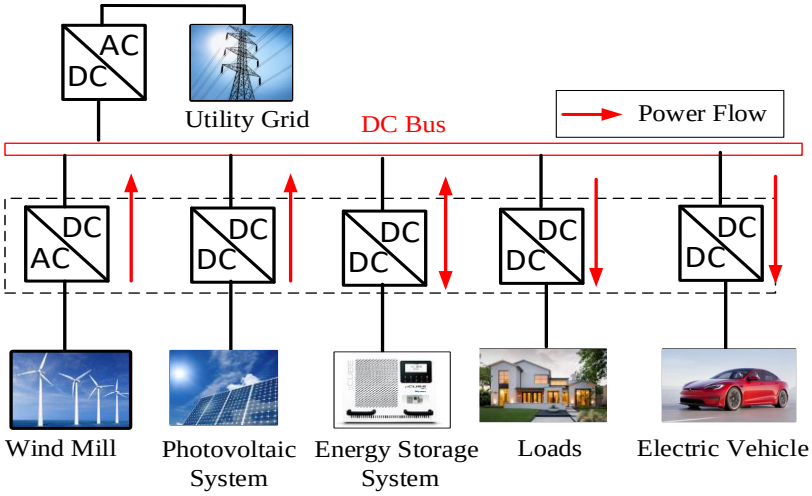

Fig. 1.5 A conceptual diagram of the conventional DC microgrid

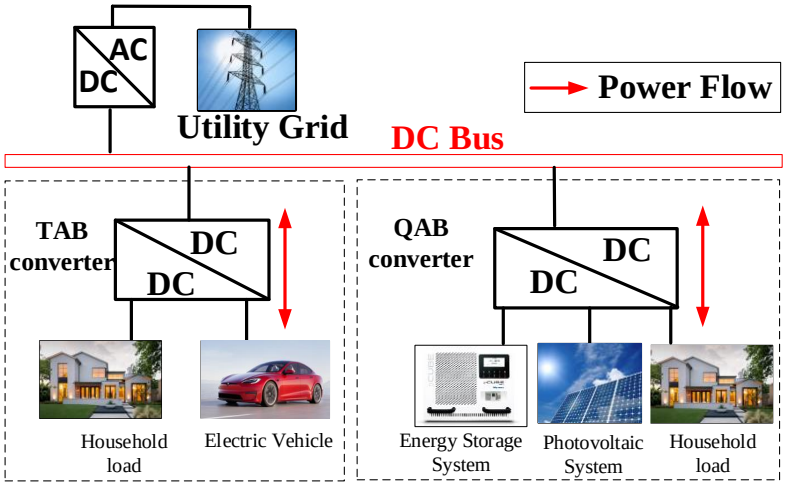

Fig. 1.6 A conceptual diagram of a multiport converter-integrated DC Microgrid

overall performance of DC microgrids, especially in situations where many converters are involved.

Previous research has been done on methods to tackle the power coupling problem. These methods can be categorized into hardware and software methods with each method having its pros and cons. A

hardware method is proposed in [8] to naturally decouple the controlled ports in a TAB converter. It involves the elimination of the external inductor at the reference port and the use of two transformers to connect output ports to the input port. With this method, power density is reduced and there is the presence of circulating current observed in the reference port. A capacitor is inserted in series with the external inductor on the third port of a series resonant-based TAB converter in [9]. This method results in decoupling characteristics between ports, but it is limited to resonant-based TAB converters, and it is characterized by low power density due to the inclusion of extra components.

Under the software decoupling category, a controller is proposed in [10] for a specific proposed TAB converter topology. The controller adapts the conventional decoupling matrix method proposed for distillation columns in [22] and adds it to an optimal operating point duty cycle and phase modulation Proportional Integrator (PI) controller. This method requires 5 control variables to achieve power regulation and decoupling. It is topology specific and requires a lot of computations. Another issue is that it adapts a double loop controller for load regulation which leads to design limitations since the speeds of the current and voltage loops differ. Another method is proposed in [11] by specifically designing phase shift control bandwidths and selecting specific duty cycles to reduce coupling effects between the phase shift and duty cycles. This method is parameter specific and hence may lead to poor performance when parameters are varied, for example when a wide input voltage range is considered. The small-signal analysis of current-fed TAB converters is done to design a constant decoupling matrix and combined with a state feedback controller to achieve better dynamic performance and decoupling characteristics. This method is difficult to implement as it requires complex mathematical modeling, and it also requires a high computation power of digital controllers. It is also specific to current-fed TAB converters.

In this thesis, a simple but effective decoupling method is proposed for power flow decoupling in TAB and QAB converters. The proposed decoupling controller utilizes look-up table (LUT)-based decoupling matrices networks together with PI controllers to dynamically decouple the TAB and QAB converters in real-time. The proposed decoupling controller makes use of only two control variables in TAB converters and three control variables in QAB converters to achieve load regulation and power flow decoupling, hence it is simple and easy to implement. In addition, the use of the LUT results in reduced controller computation burden as opposed to full runtime computations. It can also be applied to both voltage-fed and current-fed TAB converters and QAB converters.

Section II is divided into subsections 2.1 and 2.2. Subsection 2.1 presents the proposed decoupling controller in the TAB converter for applications in the grid-connected mode operation of DC microgrids. Subsection 2.2 presents the proposed controller in the TAB converter for DC bus voltage regulation in the islanding mode operation of DC microgrid systems. Section III discusses the proposed decoupling controller in the QAB converter for application in the grid-connected mode operation of DC microgrid systems. Simulations are conducted under all sections to verify the proposed decoupling controller

followed by experimental verifications. Simulation and experimental results are provided and discussed. The results show the effectiveness of the proposed power flow decoupling controller. Section IV provides concluding remarks according to the verification analysis of the proposed decoupling controller.

Ⅱ. Power Flow Decoupling Method in Triple-Active-Bridge (TAB) Converter for DC Microgrid Applications

2.1 Power Flow Decoupling in TAB Converter DC Microgrid Grid-Connected Mode Operation

In this section, a power flow decoupling control method is proposed in the conventional Triple-Active-Bridge (TAB) converter for grid-connected mode operation in DC microgrid systems. The TAB topology is designed to connect two loads via the output ports to the DC bus via the input port.

2.1.1 DC Microgrid Grid-Connected Mode Operation

In the grid-connected mode operation of DC microgrids, the utility grid via an AC-DC converter, for example, a voltage source converter (VSC), regulates the DC bus voltage and supplies energy to loads and energy storage systems if present. The TAB converter is considered for DC microgrid development in this research, and it connects two loads to the DC bus. One load can be considered as a household load and the other load as an electric vehicle charger, for example. A conceptual diagram of the intended DC microgrid application is shown in Fig. 2.1.1. Due to the coupled nature of the power flows within the TAB converter, power balancing, system stability, efficiency, and performance in the DC microgrid, are significantly affected when load power conditions are varied in the TAB converter. A software decoupling controller is therefore proposed to decouple the controlled output ports of the TAB converter to ensure microgrid stability and power balancing in grid-connected mode.

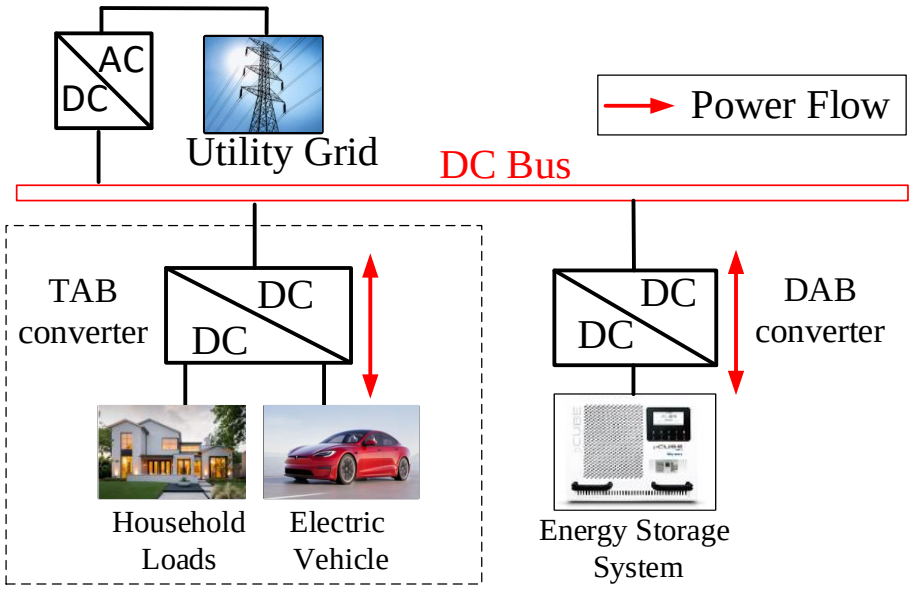

Fig. 2.1.1 A conceptual diagram of a DC microgrid operating in grid-connected mode.

2.1.2 TAB Converter Topology and Modulation

The Triple-Active-Bridge (TAB) converter is an extension of the DAB converter shown in Fig 1.4. The conventional TAB converter consists of three full-bridge converters interconnected by a single high-frequency multi-winding transformer and operates as a single converter unit. Each full-bridge converter has four active power switches that are controlled for port regulation and power transfer. The conventional TAB converter adapts three external bulk inductors (leakage inductors) at each bridge, and they are connected to the high-frequency transformer. The transformer's leakage inductance and the leakage inductance provided by the external bulk inductors are utilized for power transfer among ports. The use of the transformer ensures galvanic isolation, which is a protective mechanism to ensure damage prevention in alternate ports when a fault occurs in a port. Another advantage of the transformer is the ability to match port voltages when the appropriate turn ratios are used.

The full circuit diagram of the conventional TAB topology implemented is shown in Fig. 2.1.2. V_1, V_2, and V_3 represent the primary, secondary and tertiary ports (bridges), respectively. To analyze the operation of the TAB converter, each full-bridge converter can be replaced with a square-wave voltage source and connected to the high-frequency transformer to derive the equivalent circuit model shown in Fig. 2.1.3. As shown in the equivalent circuit, V_1 is replaced by U_{ac1}, V_2 by U_{ac2}, and V_3 by U_{ac3}. The square-wave voltages are generated by the complementary switching of power switches on the same leg in each full-bridge converter at a fixed duty ratio of 50% and a fixed switching frequency.

The implemented TAB converter adapts the single-phase-shift (SPS) modulation method for power transfer among bridges. With this modulation method, power transfer between bridges is dependent on the phase displacement between the bridge-generated square-wave voltages. Between two bridges,

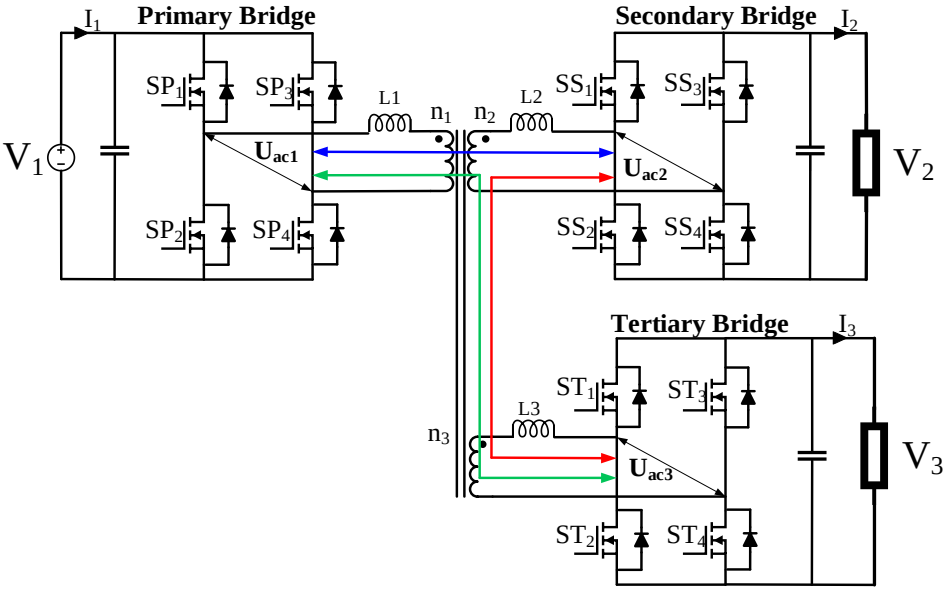

Fig. 2.1.2 Full circuit of the conventional TAB converter

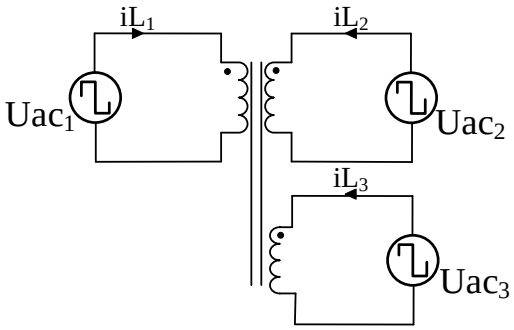

Fig. 2.1.3 Equivalent circuit of the TAB converter

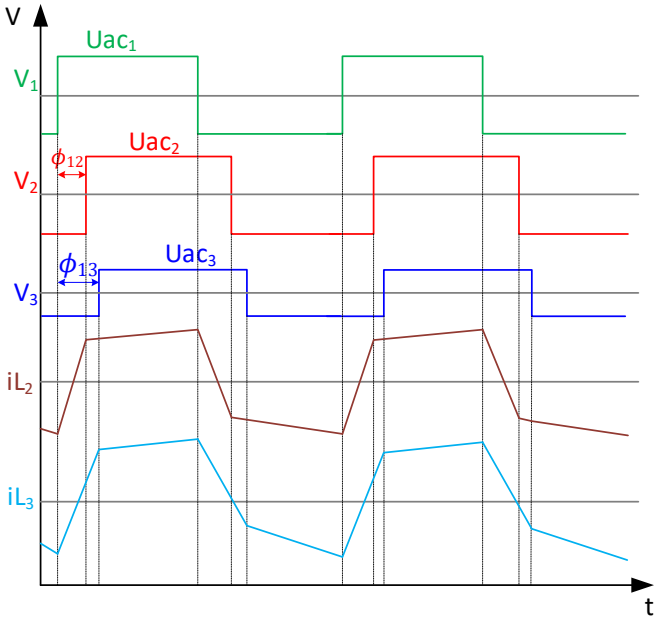

Fig. 2.1.4 Single-phase-shift modulation

power is always transferred from the bridge with the leading square-wave voltage to the bridge with the lagging square-wave voltage. Phase displacement variables are represented as ϕ_{xy} to indicate the phase displacement between bridge x and bridge y. U_{ac1} is set as the reference bridge, and the phase displacement between U_{ac1} and U_{ac2} is denoted as ϕ_{12}. The phase displacement between U_{ac1} and U_{ac3} is denoted as ϕ_{13}. A negative phase displacement value indicates that a bridge leads the reference bridge, and a positive phase displacement value means that a bridge lags the reference bridge. The maximum power transfer between bridges occurs at a phase displacement value of $\phi_{xy} = \pi/2$. The single-phase shift modulation technique is represented in Fig. 2.1.4.

2.1.3 Power Flow Analysis

The power flows among ports in the TAB converter can be analyzed by using the delta-equivalent circuit of the TAB converter derived in [13]. The delta-equivalent circuit shows a network of inductors

obtained from the external bulk inductors and the high-frequency transformer and it is shown in Fig. 2.1.5. The TAB converter power flow structure can be seen according to the delta equivalent circuit model as a network of power flows of three DAB converters. A port-to-port power flow is denoted by P_{xy}, where power is transferred from port x to port y. With U_{ac1} set as the reference, the port-to-port power flows according to the DAB subsystems are P_{12}, P_{13}, and P_{23} and the respective effective equivalent inductance for each port-to-port power flow are L_{12}, L_{13} and L_{23}. The effective equivalent inductance equations also derived in [13] can be mathematically expressed below as:

$$L_{12} = \frac{L_1L_2 + L_1L_3 + L_2L_3}{L_3} \tag{2.1.1}$$

$$L_{13} = \frac{L_1L_2 + L_1L_3 + L_2L_3}{L_2} \tag{2.1.2}$$

$$L_{23} = \frac{L_1L_2 + L_1L_3 + L_2L_3}{L_1} \tag{2.1.3}$$

The port-to-port power transfers P_{12}, P_{13} and P_{23} established in [14] can be expressed below as:

$$P_{12} = \frac{V_1V_2}{2\pi^2 f_{sw}L_{12}}\phi_{12}(\pi - |\phi_{12}|) \tag{2.4}$$

$$P_{13} = \frac{V_1V_3}{2\pi^2 f_{sw}L_{13}}\phi_{13}(\pi - |\phi_{13}|) \tag{2.5}$$

$$P_{23} = \frac{V_2V_3}{2\pi^2 f_{sw}L_{23}}(\phi_{13} - \phi_{12})(\pi - |\phi_{13} - \phi_{12}|) \tag{2.6}$$

The total active power at each port can be derived by considering the individual power flows established in the delta-equivalent circuit. The total active power at each port is a combination of two of the port-to-port power transfer relationships established in (2.1.4) ~ (2.1.6) and they can be derived and expressed as shown below:

$$P_1 = \frac{V_1V_2L_3\phi_{12}(\pi - |\phi_{12}|) + V_1V_3L_2\phi_{13}(\pi - |\phi_{13}|)}{2\pi^2 f_{sw}(L_1L_2 + L_1L_3 + L_2L_3)} \tag{2.1.7}$$

$$P_2 = \frac{V_1V_2L_3\phi_{12}(\pi - |\phi_{12}|) + V_2V_3L_1(\phi_{12} - \phi_{13})(\pi - |\phi_{12} - \phi_{13}|)}{2\pi^2 f_{sw}(L_1L_2 + L_1L_3 + L_2L_3)} \tag{2.1.8}$$

$$P_3 = \frac{V_1V_3L_2\phi_{13}(\pi - |\phi_{13}|) + V_2V_3L_1(\phi_{13} - \phi_{12})(\pi - |\phi_{13} - \phi_{12}|)}{2\pi^2 f_{sw}(L_1L_2 + L_1L_3 + L_2L_3)} \tag{2.1.9}$$

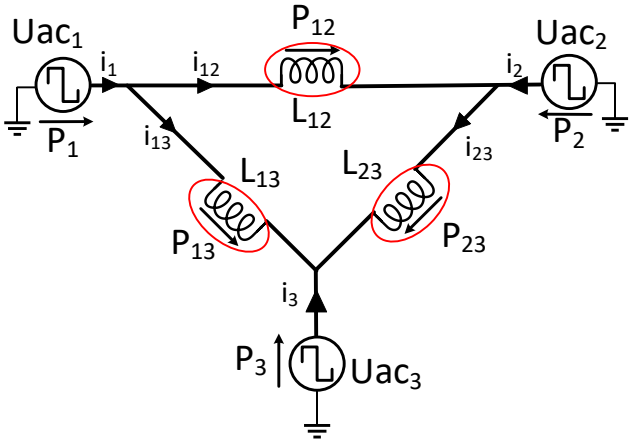

Fig. 2.1.5 Delta-equivalent circuit of the TAB converter

Where, $P_1=P_{12}+P_{13}$, $P_2= -P_{12}+P_{23}$ and $P_3 = -P_{13}-P_{23}$.

2.1.4 Power Flow Decoupling Control

In this section, the power flow coupling of the TAB converter is explained in detail. Without modifying the conventional topology, a software decoupling method is proposed to solve the coupling problem. Firstly, the concept of multivariable control is discussed relating to the TAB converter and the proposed decoupling algorithm is also discussed.

A. Multiple-Input Multiple-Output (MIMO) Controllers

MIMO control under power converter control is a complex controller system involving two or more subsystems that interact towards achieving a control goal. The TAB converter has two controlled ports, and its controller is a Dual-Input Dual-Output (DIDO) controller which is a type of MIMO controller. Fig. 2.1.6 shows a block diagram of a DIDO plant whose inputs are x_1 and x_2 with respective corresponding outputs y_1 and y_2. To regulate y_1 and y_2, a feedback controller is introduced into the plant system. As seen in Fig. 2.1.6, x_1 and y_1 are related by the transfer function, C_{11} and x_2 and y_2 are related by the transfer function C_{22}. The figure depicts an interaction between the two systems via a path of cross-coupling (hidden loops) that affect controller stability [15].

A disturbance in the x_1- to-y_1 loop, affects the x_2-to-y_2 loop via the transfer function C_{12} and a disturbance in the x_2-to-y_2 loop affects the x_1-to-y_1 loop via C_{21}. The interaction that exists between the loops leads to control instability. The control loops should be decomposed into independent loops to independently regulate y_1 and y_2 and this can be done by including a decoupler in the controller. The type of decoupler considered in this research is a feedforward decoupler. The feedforward decoupler is placed before the plant to decouple the control loops. A block diagram of a plant system with a feedforward decoupler is shown in Fig. 2.1.7.

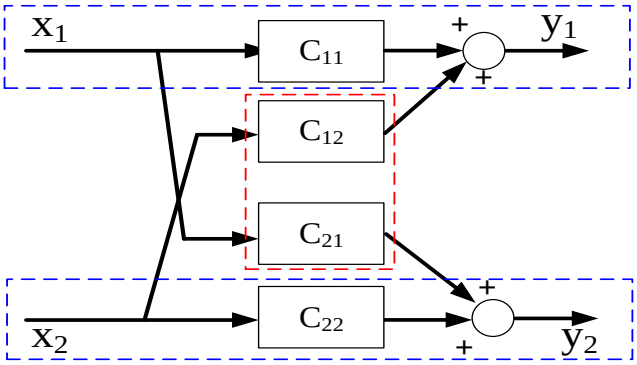

Fig. 2.1.6 Block diagram of a dual-input dual-output controller

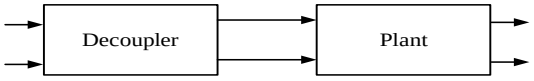

Fig. 2.1.7 Block diagram of a plant system with a decoupler

B. TAB Converter Controller

To determine the control characteristics of the TAB converter, the external coupling inductors, the phase displacement variables ϕ_{12} and ϕ_{13}, and the equivalent circuit of the three-winding transformer are considered. The port-to-port power equations established from the delta-equivalent circuit, include the effective inductance L_{12}, L_{13}, and L_{23}. The mathematical expressions of each effective inductance show both direct and indirect proportional relationships of all the external inductors. This shows that each power transfer path in the system involves all the external bulk inductors resulting in power flow coupling in all the ports. Referencing the discussion in section 2.1.4 A, feedback control is considered in the TAB converter, and the PI controller is chosen for output load regulation. The TAB converter controller block diagram is shown in Fig. 2.1.8. The relationship between the inputs and outputs can be established by a transfer function matrix (H) and the matrix elements are the transfer functions H_{11}, H_{12}, H_{21}, and H_{22}. As seen in the block diagram of the converter's controller, the control variable ϕ_{12} and V_2 are related by the transfer function H_{11} and the PI controller H_{PI_V2} is implemented to regulate V_2. The control variable ϕ_{13} and the output voltage V_3 are related by the transfer function H_{11} and the PI controller H_{PI_V3} is implemented to regulate V_3.

H_{12} and H_{21} are the cross-coupling terms in the system that results in the interaction between the two PI feedback loops. To eliminate the cross-coupling terms, a decoupling matrix network can be used. This decoupling matrix network is a feedforward decoupler that transforms the coupled loops into independent single-input single-output (SISO) loops. V_2 and V_3 can therefore be independently regulated by the SISO loops. The TAB converter controller according to Fig 2.1.8 can be expressed in the matrix equation shown below:

$$\begin{bmatrix} I_2 \\ I_3 \end{bmatrix} = \begin{bmatrix} H_{11} & H_{12} \\ H_{21} & H_{22} \end{bmatrix} \begin{bmatrix} \phi_{12} \\ \phi_{13} \end{bmatrix} = H\vec{\phi} \tag{2.1.10}$$

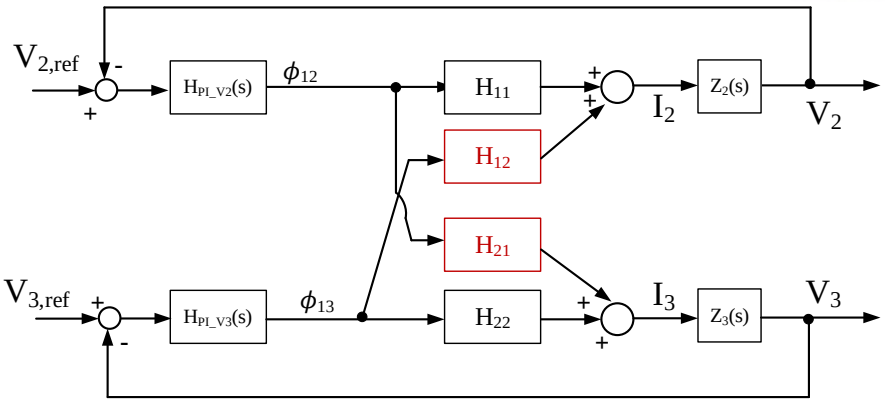

Fig. 2.1.8 Block diagram of the TAB converter controller

To represent the control block diagram of the TAB converter according to (2.1.10), the output capacitor and the load which represents the output impedance are considered since output voltage regulation is considered. The transfer function of the output impedance is denoted as Z(s), and it can be mathematically expressed below as:

$$Z(s) = \frac{R_L}{1 + R_L C_L s} \tag{2.1.14}$$

where C_L represents the output filter capacitor and R_L represents the load. The output impedance in port 2 is represented as $Z_2(s)$ and the output impedance in port 3 is represented as $Z_3(s)$. The transfer functions of the PI controllers are denoted as $H_{PI\_V2}(s)$ for the control loop in port 2 and $H_{PI\_V3}(s)$ for the control loop in port 3.

C. Conventional Power Flow Decoupling Method

The conventional method of decoupling MIMO controllers is the use of a decoupling matrix to eliminate the cross-coupling terms in the plant matrix. The decoupling matrix is an inverse of the plant matrix, and this means that this method can be applied if the plant matrix is a square matrix that has a full rank and if the determinant of the square matrix is not zero. In other words, the inverse matrix method is applicable if the plant matrix is invertible or nonsingular [28], [29]. The determinant of a matrix (H') can be calculated as shown below:

$$\det(H) = H_{11}H_{22} - H_{12}H_{21} \tag{2.1.11}$$

It is important to consider this condition and factor it into the design of the converter parameters to ensure that H is nonsingular. The conditions for decoupling are discussed as theorems with supporting proofs [28],[29], and [30]. If the condition of non-singularity is met, a decoupling matrix can be derived by calculating the inverse of H and included in the controller. The decoupling matrix (N) is calculated

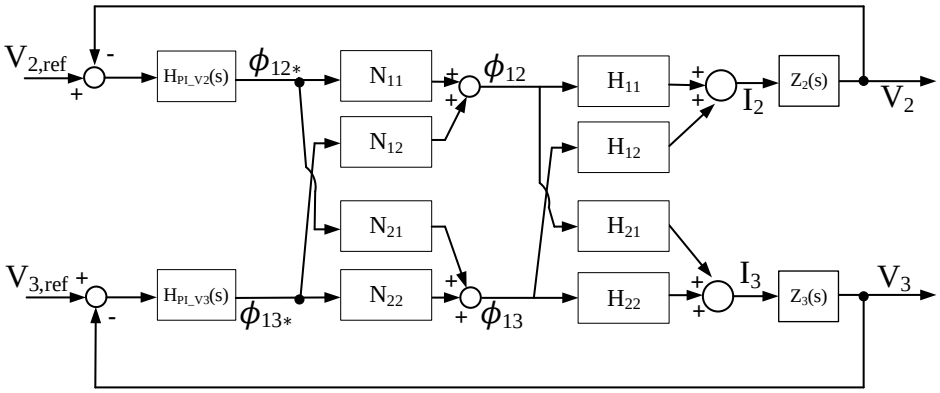

Fig. 2.1.9 Block diagram of the TAB converter controller with decoupling network.

according to the following equation:

$$N = \begin{bmatrix} N_{11} & N_{12} \\ N_{21} & N_{22} \end{bmatrix} = H^{-1} = \frac{1}{H_{11}H_{22} - H_{12}H_{21}} \begin{bmatrix} H_{22} & -H_{12} \\ -H_{21} & H_{11} \end{bmatrix} \tag{2.1.12}$$

By including the decoupling matrix in the system's controller, the cross-coupling terms, H_{12}, and H_{21}, are eliminated and the DIDO controller is decomposed into individual SISO controllers that independently regulate the output loads. The introduction of the decoupling matrix network in the controller generates new phase control variables which are denoted as ϕ_{12*} and ϕ_{13*} and the system control transfer matrix transforms into a unit matrix as shown below:

$$\begin{bmatrix} I_2 \\ I_3 \end{bmatrix} = \begin{bmatrix} H_{11} & H_{12} \\ H_{21} & H_{22} \end{bmatrix} \begin{bmatrix} N_{11} & N_{12} \\ N_{21} & N_{22} \end{bmatrix} \begin{bmatrix} \phi_{12*} \\ \phi_{13*} \end{bmatrix} = \begin{bmatrix} 1 & 0 \\ 0 & 1 \end{bmatrix} \begin{bmatrix} \phi_{12*} \\ \phi_{13*} \end{bmatrix} \tag{2.1.13}$$

The resulting controller which represents the conventional decoupling method is shown in Fig. 2.1.9.

D. Proposed Power Flow Decoupling Method

A power flow decoupling method is proposed in this section to decouple the TAB converter controller for independent regulation of the output ports. The proposed method is a modification of the conventional method to improve decoupling performance and system dynamic performance using only two degrees of freedom as opposed to the use of five degrees of freedom in [10], [11], and [12]. The TAB converter is a DC-DC converter with its dynamics being nonlinear in nature. Therefore, to design the proposed controller, a linearized time-invariant model of the TAB converter should be derived. The conventional state-space averaging technique, if adapted, complicates the derivation of the linearized model because, over one switching cycle, the integral value of the external inductor current is zero. The linearization approach used in this research involves the use of basic equations to generate the system

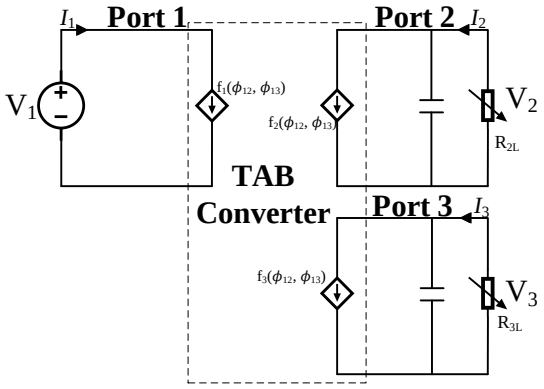

Fig. 2.1.10 Average model of the TAB converter

transfer function under the condition that the dynamics of all passive components are neglected [16].

As stated earlier, the TAB converter can be decomposed into a set of three DAB converters. Each DAB subsystem can be considered as a set of controlled current sources and the average model of the TAB converter shown in Fig. 2.1.10, can be derived based on that. The average current at the output is a function of the phase displacement between the bridges [17] and therefore in the proposed decoupling method, the converter's operating points which are dependent on the output currents are considered. Fig. 2.1.11. shows a plot of current vs phase shift with the operating points ϕ^ indicated along the curve. For each operating point, the transfer function of the system is different. The linearization of the TAB converter is therefore done by considering various operating points represented by (^). With the linearized model, the gain matrix element values can be estimated for all the considered operating points. The average currents at port 2 and port 3 are represented by I_2 and I_3 respectively. The average current can be used to represent the port powers since constant voltage regulation is considered. I_2 is derived from P_2 as shown below:

$$I_2 = \frac{P_2}{V_2} = \frac{P_{12} + P_{23}}{V_2} \tag{2.1.15}$$

$$I_2 = \frac{V_1(\pi - |\phi_{12}|)\phi_{12}}{2\pi^2 f_{sw} L_{12}} + \frac{V_3(\pi - |\phi_{12} - \phi_{13}|)(\phi_{12} - \phi_{13})}{2\pi^2 f_{sw} L_{23}} \tag{2.1.16}$$

Similarly, I_3 can be derived from P_3 as shown below:

$$I_3 = \frac{P_3}{V_3} = \frac{P_{13} + P_{32}}{V_3} \tag{2.1.17}$$

$$I_3 = \frac{V_1(\pi - |\phi_{13}|)\phi_{13}}{2\pi^2 f_{sw} L_{13}} + \frac{V_2(\pi - |\phi_{13} - \phi_{12}|)(\phi_{13} - \phi_{12})}{2\pi^2 f_{sw} L_{23}} \tag{2.1.18}$$

The quadratic terms in the average current equations make the linearization of the TAB converter difficult, therefore the Fourier series sinusoidal approximation [16] shown in (2.1.19) is applied to

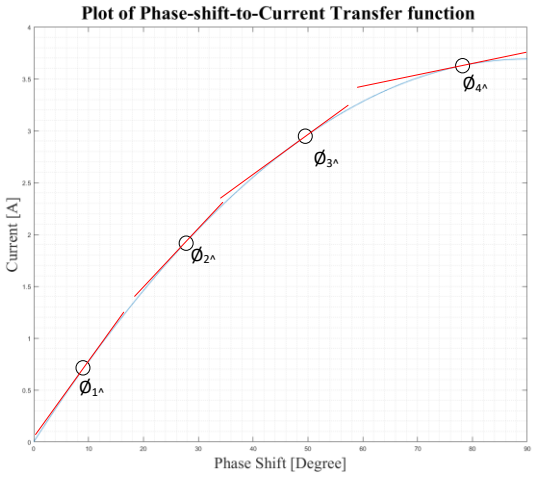

Fig. 2.1.11 A graph showing the relationship between phase shift and current

(2.1.16) and (2.1.18) to simplify them. A graph of approximation comparison is provided in the appendix section.

$$\phi(\pi-\phi)\approx\frac{8}{\pi}\sin\phi \tag{2.1.19}$$

The simplified current equations resulting from the approximation transformation are expressed as follows:

$$I_2=\frac{V_1\sin(\phi_{12})}{\frac{1}{4}\pi^3 f_{sw}L_{12}}+\frac{V_3\sin(\phi_{12}-\phi_{13})}{\frac{1}{4}\pi^3 f_{sw}L_{23}} \tag{2.1.20}$$

$$I_3=\frac{V_1\sin\phi_{13}}{\frac{1}{4}\pi^3 f_{sw}L_{13}}+\frac{V_2\sin(\phi_{13}-\phi_{12})}{\frac{1}{4}\pi^2 f_{sw}L_{23}} \tag{2.1.21}$$

The output current at each controlled port in the TAB converter can be represented as the summation of their steady-state values and small-signal variations, i.e., $I_x=I_{x\wedge}+\Delta I_x$, where, I_x represents the output current of a port, x, $I_{x\wedge}$ represents the steady-state value and ΔI_x represents the small signal variation of I_x. Accordingly, I_2 is represented as (2.1.22), and the Taylor series operation of I_2 about the operating point (^) results in (2.1.23).

$$I_2=I_{2\wedge}+\Delta I_2 \tag{2.1.22}$$

$$I_2=\left[\frac{V_1\sin(\phi_{12\wedge})}{\frac{1}{4}\pi^3 f_{sw}L_{12}}+\frac{V_3\sin(\phi_{12\wedge}-\phi_{13\wedge})}{\frac{1}{4}\pi^3 f_{sw}L_{23}}\right]+\left[\frac{V_1\cos(\phi_{12\wedge})\Delta\phi_{12}}{\frac{1}{4}\pi^3 f_{sw}L_{12}}+\frac{V_3\cos(\phi_{12\wedge}-\phi_{13\wedge})\Delta\phi_{12}}{\frac{1}{4}\pi^3 f_{sw}L_{23}}-\frac{V_3\cos(\phi_{12\wedge}-\phi_{13\wedge})\Delta\phi_{13}}{\frac{1}{4}\pi^3 f_{sw}L_{23}}\right] \tag{2.1.23}$$

Using the same procedure, I_3 is represented as (2.2.24), and the Taylor series operation of I_3 about the operating point (^) results in (2.1.25)

$$I_3 = I_{3\wedge} + \Delta I_3 \tag{2.1.24}$$

$$I_3 = \left[\frac{V_1 \sin(\phi_{12\wedge})}{\frac{1}{4}\pi^3 f_{sw} L_{12}} + \frac{V_3 \sin(\phi_{12\wedge} - \phi_{13\wedge})}{\frac{1}{4}\pi^3 f_{sw} L_{23}} \right] + \left[-\frac{V_2 \cos(\phi_{12\wedge} - \phi_{13\wedge})\Delta\phi_{12}}{\frac{1}{4}\pi^3 f_{sw} L_{23}} + \frac{V_1 \cos(\phi_{13\wedge})\Delta\phi_{13}}{\frac{1}{4}\pi^3 f_{sw} L_{13}} + \frac{V_2 \cos(\phi_{12\wedge} - \phi_{13\wedge})\Delta\phi_{13}}{\frac{1}{4}\pi^3 f_{sw} L_{23}} \right] \tag{2.1.25}$$

The small-signal variations of both I_2 and I_3 can be expressed as a summation of products of varying phase shifts and sub-transfer functions of the system gain matrix. The resulting representations of I_2 and I_3 are shown below:

$$I_2 = I_{2\wedge} + H'_{11}\Delta\phi_{12} + H'_{12}\Delta\phi_{13} \tag{2.1.26}$$

$$I_3 = I_{3\wedge} + H'_{21}\Delta\phi_{12} + H'_{22}\Delta\phi_{13} \tag{2.1.27}$$

The individual operating point-dependent gain matrix (H') elements can be derived from (2.1.23) and (2.1.25) and expressed as follows:

$$H'_{11} = \frac{V_1 L_3 \cos(\phi_{12\wedge}) + V_3 L_1 \cos(\phi_{12\wedge} - \phi_{13\wedge})}{\frac{1}{4}\pi^3 f_{sw}(L_1 L_2 + L_1 L_3 + L_2 L_3)} \tag{2.1.28}$$

$$H'_{12} = \frac{-V_3 L_1 \cos(\phi_{12\wedge} - \phi_{13\wedge})}{\frac{1}{4}\pi^3 f_{sw}(L_1 L_2 + L_1 L_3 + L_2 L_3)} \tag{2.1.29}$$

$$H'_{21} = \frac{-V_2 L_1 \cos(\phi_{13\wedge} - \phi_{12\wedge})}{\frac{1}{4}\pi^3 f_{sw}(L_1 L_2 + L_1 L_3 + L_2 L_3)} \tag{2.1.30}$$

$$H'_{22} = \frac{V_1 L_2 \cos(\phi_{13\wedge}) + V_2 L_1 \cos(\phi_{13\wedge} - \phi_{12\wedge})}{\frac{1}{4}\pi^3 f_{sw}(L_1 L_2 + L_1 L_3 + L_2 L_3)} \tag{2.1.31}$$

The control-to-output transfer function matrix of the TAB converter according to the linearized model is established and expressed below:

$$\begin{bmatrix} \Delta I_2 \\ \Delta I_3 \end{bmatrix} = \begin{bmatrix} H'_{11} & H'_{12} \\ H'_{21} & H'_{22} \end{bmatrix} \begin{bmatrix} \Delta\phi_{12} \\ \Delta\phi_{13} \end{bmatrix} \tag{2.1.32}$$

At a set interval of 10 W, estimated values of the operating points $\phi_{12\wedge}$ and $\phi_{13\wedge}$ across the rated power. are calculated and the numerical values of the gain matrix are calculated using the linearized model equations. The estimation of the operating point values is possible because all other parameters in the port active power equations are fixed. For each set of gain matrix values, the decoupling matrix (N') is

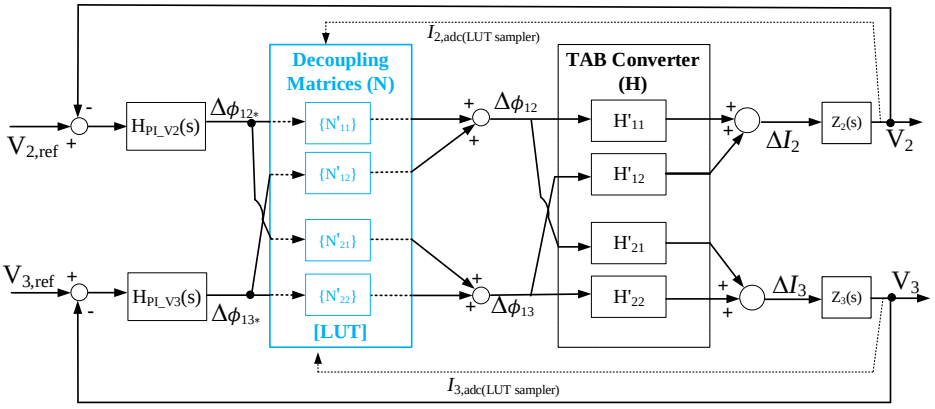

Fig. 2.1.12 Block diagram of the proposed decoupling controller

derived by finding the inverse as shown below:

$$\begin{bmatrix} N'_{11} & N'_{12} \\ N'_{21} & N'_{22} \end{bmatrix} = H'^{-1} = \frac{1}{H'_{11}H'_{22} - H'_{12}H'_{21}} \begin{bmatrix} H'_{22} & -H'_{12} \\ -H'_{21} & H'_{11} \end{bmatrix} \tag{2.1.33}$$

The calculated sets of decoupling matrices are stored in a look-up table as part of the proposed decoupling controller. The inclusion of the decoupling matrix network results in new phase variables denoted as ϕ_{12*} and ϕ_{13*} and the resulting proposed decoupling controller is expressed as follows:

$$\begin{bmatrix} \Delta I_2 \\ \Delta I_3 \end{bmatrix} = \begin{bmatrix} N'_{11} & N'_{12} \\ N'_{21} & N'_{22} \end{bmatrix} \begin{bmatrix} H'_{11} & H'_{12} \\ H'_{21} & H'_{22} \end{bmatrix} \begin{bmatrix} \Delta\phi_{12*} \\ \Delta\phi_{13*} \end{bmatrix} \tag{2.1.34}$$

The proposed decoupling controller is shown as a block diagram representation in Fig. 2.1.12. It is made up of two PI controllers $H_{PI\_V2}(s)$ and $H_{PI\_V3}(s)$ connected to a LUT that stores decoupling matrices extracted for controller decoupling. I_2,adc, and $I_{3,adc}$ shown in the block diagram are the input variables for LUT sampling. Decoupling matrices are selected based on the output current level of each controlled port. The decoupling matrices ensure that the controller is decoupled for all considered operating points with minimal errors. The final matrix equation expressed in (2.1.35) indicates that the system gain matrix transforms into a unit matrix at all system operating conditions. The design and operation of the implemented LUT are further discussed in subsection E.

$$\begin{bmatrix} \Delta I_2 \\ \Delta I_3 \end{bmatrix} = \begin{bmatrix} 1 & 0 \\ 0 & 1 \end{bmatrix} \begin{bmatrix} \Delta\phi_{12*} \\ \Delta\phi_{13*} \end{bmatrix} \tag{2.1.35}$$

The gain matrices for all the considered operating points are checked for singularity by calculating their determinants with MATLAB using the parameters in Table 2.1.1. According to the results, plots of the determinants, gain matrices, and corresponding decoupling matrices are shown in Fig. 2.13 (a),

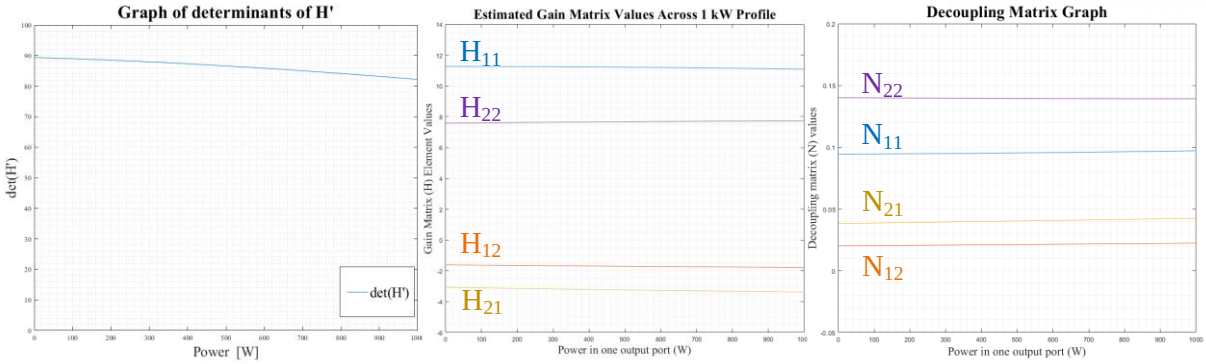

(a) (b) (c)

Fig. 2.1.13 Plots of: (a) determinant of *H'*, (b) gain matrices, (c) decoupling matrices

Fig. 2.13 (b), and Fig. 2.13 (c), respectively. As shown in the plot of det(*H'*), *H'* is nonsingular for all operating points making it possible to derive the decoupling matrices. The above process is repeated for all implemented converters in this thesis. The rank of each matrix is equal to its size and this means that the matrices are full rank.

E. Design and Operation of the Implemented Look-Up Table

A key component of the proposed decoupling controller is the Look-up table (LUT). It is included to store decoupling matrices values for dynamic controller decoupling. Using the look-up table reduces controller computational burden as opposed to runtime computations of gain and decoupling matrices. Moreover, the algorithm applied in designing the lookup table is fast for matrix element extraction, simple, and easy to implement. The structure of the look-up table is shown in Fig. 2.1.14 (a). It is made up of individual arrays that store individual sets of values. The arrays are I_2, I_3, N'_{11}, N'_{12}, N'_{21}, and N'_{22}, where I_2 and I_3 represent index arrays and N'_{11}, N'_{12}, N'_{21}, and N'_{22} represent the decoupling matrices arrays. Each index array is linked to two decoupling matrices arrays. I_2 is linked to N'_{11} and N'_{21}, and I_3 is linked to N'_{12} and N'_{22}. $I_{2,adc}$, and $I_{3,adc}$ are the sampled ADC current values from port 2 and port 3, respectively.

The rated power for each output port is 1 kW, therefore the decoupling matrices are calculated across a 1kW profile. It is cumbersome to calculate the decoupling matrix for every 1 W, therefore, calculation of the decoupling matrix is done for every 10 W. This means that each decoupling matrix element has a set of 101 values across the 1kW power profile. Based on this calculation, the index array elements are calculated to match their respective power levels and hence respective decoupling matrices values for all decoupling matrix elements. The index array elements (I_2 and I_3) values are calculated with the basic power equation which is the product of voltage and current. This estimation is possible because of constant voltage regulation in the steady state.

Regarding the operation of the LUT and decoupling matrices extraction, the C pointer algorithm is used for array element sorting in the LUT. First, the ADC currents are sampled by the controller, and

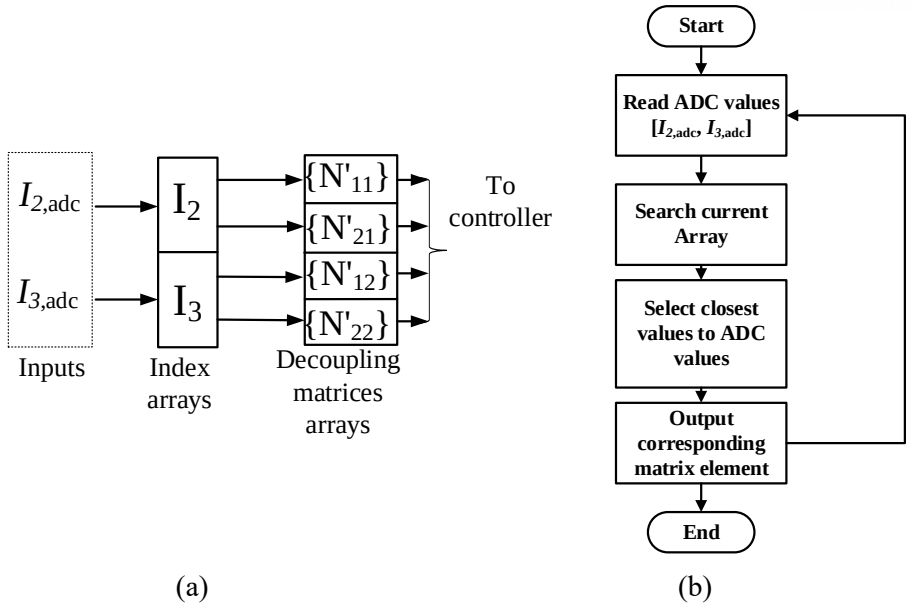

Fig. 2.1.14 Diagrams for the implemented LUT: (a) Structure of the LUT, (b) Flow chart of the look-up table operation

the sampled ADC values, $I_{2,adc}$ and $I_{3,adc}$ are assigned as inputs in the LUT. The algorithm takes in the inputs and searches through the respective index arrays to find values that match the inputs. If an element in the index array matches an input, corresponding decoupling matrices values in the decoupling matrices arrays are returned as outputs to the controller. In practice, it is almost impossible for the sampled ADC values to match with index array values due to decimal point differences, and value differences. The algorithm is therefore modified to find index array values that are closest to the input values. This ensures that there are decoupling matrices extracted to the controller at any time in the TAB converter's operation according to the output current levels. The operation of the LUT is illustrated in the flow chart shown in Fig. 2.1.14 (b). The implemented code for the LUT operation is fast for the LUT elements extraction and it does not require high computation power.

2.1.5 Simulation and Simulation Results

A circuit model of the conventional TAB converter is simulated using the PSIM software as shown in Fig. 2.1.15. Simulation of the TAB converter model is conducted to observe the performance and effectiveness of the proposed decoupling controller before experimenting. Each LUT block stores current index values and a set of decoupling matrices. The value organization per block is similar to the LUT structure discussed in section 2.1.4 E. The simulation is conducted at a switching frequency of 50kHz and with a simulation time step of 1E-7. The input voltage is set at 380 V and port 2 and port 3 have their voltages set at 380 V and 200 V, respectively with a turn ratio of 1:1:0.526. The inductor at the primary port has an inductance value of 59.2μH, and the values of the inductors at the secondary and tertiary ports are 62.3μH and 35.04μH, respectively. The parameters are designed to consider

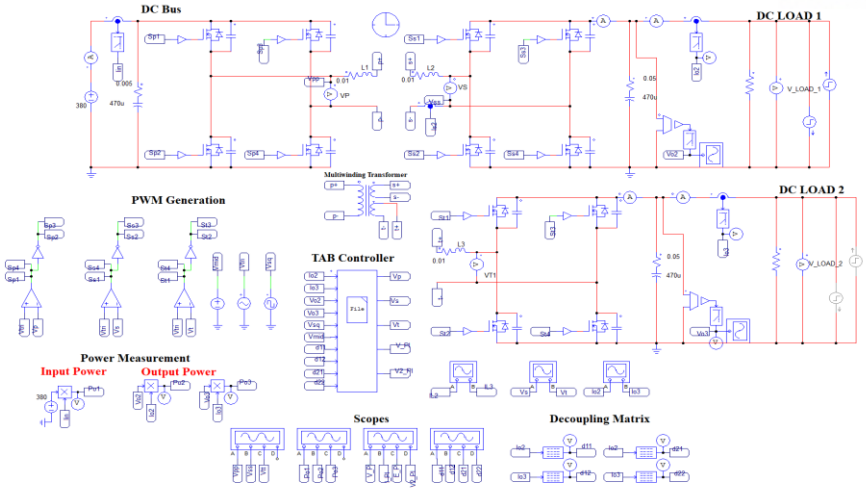

Fig. 2.1.15 Simulation setup using PSIM software

Table 2.1.1: Simulation and Experiment parameters

Parameter	Symbol	Value	Unit
Port 1 voltage (DC bus)	V_1	380	V
Port 2 voltage (Load 1)	V_2	380	V
Port 3 voltage (Load 2)	V_3	200	V
	L_1	59.2	µH
Bulk inductors	L_2	62.3	µH
	L_3	35.04	µH
Switching frequency	f_{sw}	50	kHz
Turn ratio	n1:n2:n3	1:1:0.526	

varying port voltages and leakage inductance values. A summary of the simulation parameters is provided in Table 2.1.1 and the simulation waveforms are captured for all simulation test cases.

In test case 1, power is varied in V_2 from 100 W to 1 kW and then back to 100 W. This test case is conducted with and without the proposed decoupling controller. Without decoupling control, voltage, current, and power waveforms for both V_2 and V_3 are captured and analyzed. In terms of voltage, a voltage undershoot of 9.56 V is observed in V_2, and a voltage undershoot of 5.23 V is captured in V_3 when the power in V_2 is stepped from 100 W to 1kW without decoupling control. When the power in V_2 is stepped down from 1 kW to 100 W, a voltage overshoot of 9.58 V is seen in V_2, and a voltage overshoot of 5.34 V is observed in V_3 also without decoupling control. With the proposed decoupling controller, the initial voltage undershoot in V_3 is reduced to 0.27 V when the power in V_2 is stepped from 100 W to 1 kW. This represents a 94.84% voltage decoupling performance. When the power in V_2 is stepped down from 1 kW to 100 W, the initial voltage overshoot is reduced to 0.31 V with the proposed decoupling controller. This translates to a 94.19% voltage decoupling performance. The voltage simulation results without decoupling control are shown in Fig. 2.1.16 (a) and the voltage simulation results with the proposed decoupling control are shown in Fig. 2.1.16 (b).

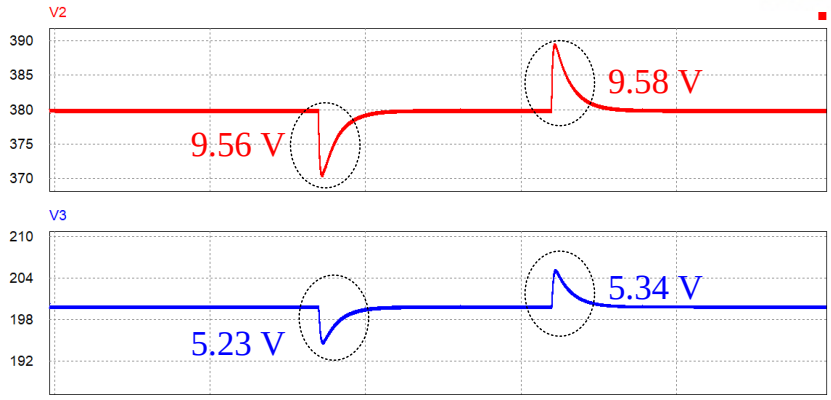

(a)

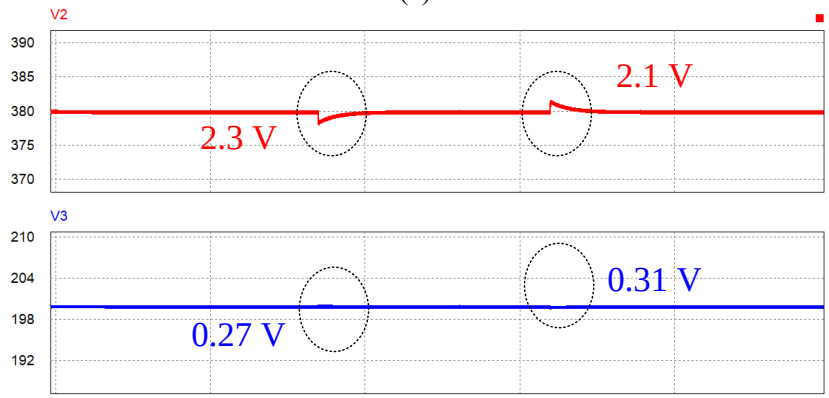

(b)

Fig. 2.1.16 Voltage simulation waveforms for steps in V_2: (a) without decoupling, (b) with decoupling

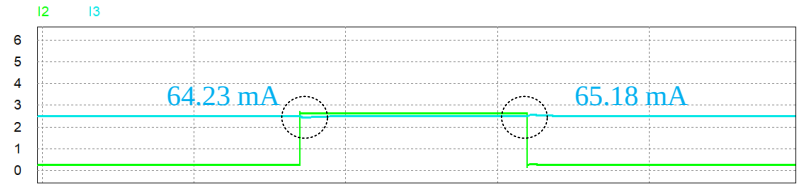

(a)

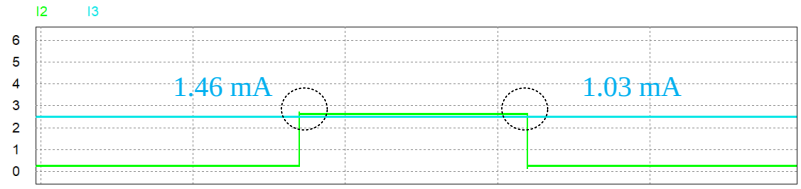

(b)

Fig. 2.1.17 Current simulation waveforms for steps in V_2: (a) without decoupling, (b) with decoupling

On the current simulation, a current undershoot of 64.23 mA is observed in V_3, when the power in V_2 is stepped from 100 W to 1 kW without decoupling control. When the power in V_2 is stepped down from 1 kW to 100 W, a current overshoot of 65.18 mA is seen in V_3, also without decoupling control. The initial current undershoot in V_3 is reduced to 1.46 mA when the power in V_2 is stepped from 100 W to 1 kW with the proposed decoupling controller. This translates to a 97.73% current decoupling performance. When the power in V_2 is stepped down from 1kW to 100 W, the initial current overshoot

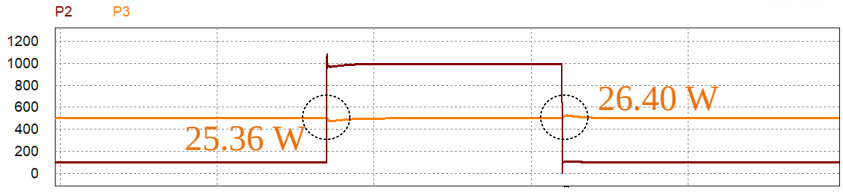

(a)

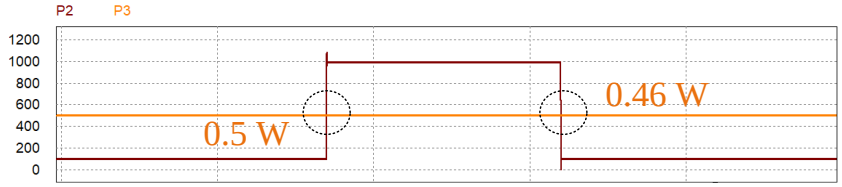

(b)

Fig. 2.1.18 Power simulation waveforms for steps in V_2: (a) without decoupling, (b) with decoupling

is reduced to 1.93 mA with the proposed decoupling controller. This represents a 97.04% current decoupling performance. The current simulation results without decoupling control are shown in Fig. 2.1.17 (a) and the current simulation results with the proposed decoupling control are shown in Fig. 2.1.17 (b).

For power simulation, a power undershoot of 25.36 W is observed in V_3, when the power in V_2 is stepped from 100 W to 1kW without decoupling control. Under the same condition, when the power in V_2 is stepped down from 1 kW to 100 W, a power overshoot of 26.4 W is seen in V_3. With the proposed decoupling controller, the initial power undershoot in V_3 is reduced to 0.51 W when the power in V_2 is stepped from 100 W to 1 kW. This represents a 97.99% power decoupling performance. When the power in V_2 is stepped down from 1 kW to 100 W, the initial power overshoot is reduced to 0.46 W with the proposed decoupling controller. This translates to a 98.26% power decoupling performance. The power simulation results without decoupling control are shown in Fig. 2.1.18 (a) and the power simulation results with decoupling control are shown in Fig. 2.1.18 (b).

In test case 2, power is varied in V_3 from 100 W to 1 kW and then back to 100 W with and without the proposed decoupling controller. Power step times are the same as in test case 1. A voltage undershoot of 13.72 V is seen in V_3 when its power is stepped from 100 W to 1 kW without the decoupling controller. Corresponding coupling effects are observed in V_2, where a 5.24 V voltage undershoot is observed. With the proposed decoupling controller, the initial voltage undershoot in V_2 is reduced to 0.93 V. This shows an 82.25% voltage decoupling performance. When the power is stepped down from 1 kW to 100W, a voltage overshoot of 5.43 V is observed in V_2 without decoupling control. With the proposed decoupling controller initial voltage overshoot in V_2 is reduced to 1.05 and this represents an 80.66% voltage decoupling performance. The voltage simulation results without decoupling control are shown in Fig. 2.1.19 (a) and the voltage simulation results with the proposed decoupling control are shown in Fig. 2.1.19 (b). Another observation is the reduction in the undershoot and overshoot of V_2 and V_3 according to load variations. The initial undershoots are reduced to 2.3 V for V_2 and 5.43 V for V_3. The

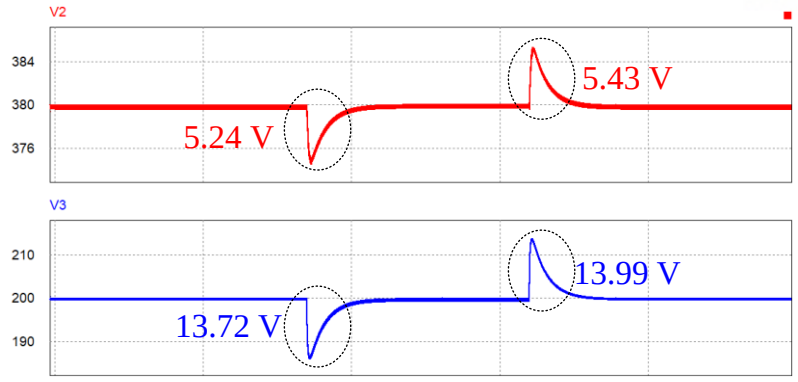

(a)

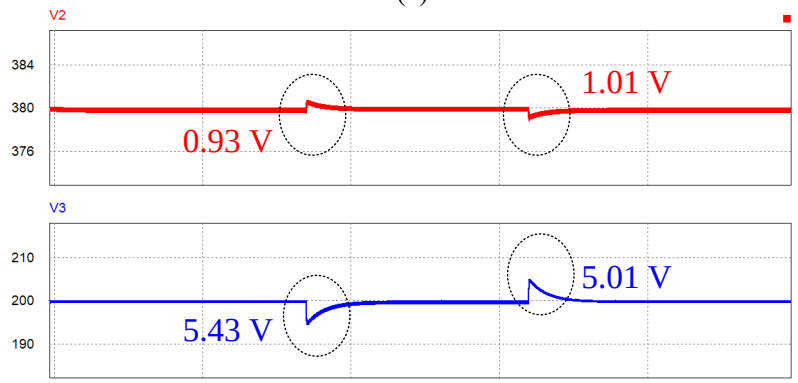

(b)

Fig. 2.1.19 Voltage simulation waveforms for steps in V_3: (a) without decoupling, (b) with decoupling

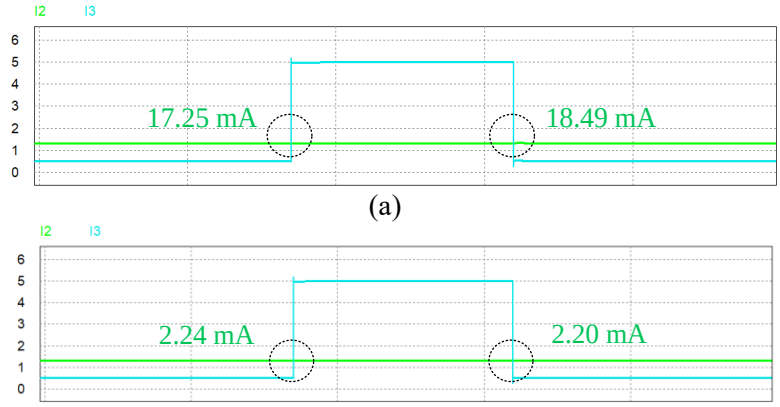

(a)

(b)

Fig. 2.1.20 Current simulation waveforms for steps in V_3: (a) without decoupling, (b) with decoupling

initial overshoots are reduced to 2.1 V for V_2 and 5.01 V for V_3.

For the current simulation, a current undershoot of 17.25 mA is captured in V_2, when the power in V_3 is stepped from 100 W to 1 kW without decoupling control. When the power in V_3 is stepped down from 1 kW to 100 W, a current overshoot of 18.49 mA is seen in V_2. With the proposed decoupling controller, the initial current undershoot in V_2 is reduced to 2.24 mA when the power in V_3 is stepped from 100 W to 1 kW. This represents an 87.01% power decoupling performance. When the power in V_3 is stepped down from 1 kW to 100 W, the initial current overshoot in V_2 is reduced to 2.20 mA with the

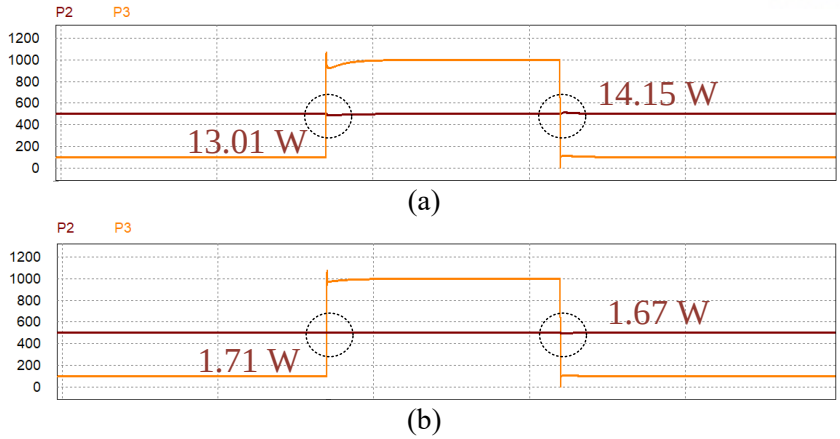

Fig. 2.1.21 Power simulation waveforms for steps in V_3: (a) without decoupling, (b) with decoupling

proposed decoupling controller. This translates to an 88.10% power decoupling performance. The current simulation results without decoupling control are shown in Fig. 2.1.20 (a) and the current simulation results with the proposed decoupling control are shown in Fig. 2.1.20 (b).

For power simulation, a power undershoot of 13.01 W is observed in V_2, when power in V_3 is stepped from 100 W to 1 kW without decoupling control. When the power in V_3 is stepped down from 1 kW to 100 W, a power overshoot of 14.15 W is seen in V_2 also without decoupling control. The initial power undershoot in V_2 is reduced to 1.17 W when the power in V_3 is stepped from 100 W to 1 kW with the proposed decoupling controller. This translates to an 86.86% power decoupling performance. When the power in V_3 is stepped down from 1 kW to 100 W, the initial power overshoot in V_2 is reduced to 1.67 W with the proposed decoupling controller. This represents an 88.20% power decoupling performance. The simulation results without decoupling and with the proposed controller are shown in Fig. 2.1.21 (a) and Fig. 2.1.21 (b), respectively. All the simulation results are summarized in tables 2.2.2, 2.2.3, and 2.2.4.

Table 2.1.2: Voltage simulation results in alternate port according to load variation

	Power Step	**Without Decoupling (V)**	**With Decoupling (V)**	**Decoupling performance**
Step in V_2	100 W – 1 kW	5.23	0.27	94.84%
	1 kW – 100 W	5.34	0.31	94.19%
Step in V_3	100 W – 1 kW	5.24	0.93	82.25%
	1 kW – 100 W	5.43	1.05	80.66%

Table 2.1.3: Current simulation results in alternate port according to load variation

	Power Step	**Without Decoupling (mA)**	**With Decoupling (mA)**	**Decoupling performance**
Step in V_2	100 W – 1 kW	64.23	1.46	97.73%
	1 kW – 100 W	65.18	1.93	97.04%
Step in V_3	100 W – 1k W	17.25	2.24	87.01%
	1k W – 100 W	18.49	2.2	88.10%

Table 2.1.4: Power simulation results in alternate port according to load variation

	Power Step	Without decoupling (W)	With Decoupling (W)	Decoupling performance
Step in V_2	100 W – 1 kW	25.36	0.51	97.99%
	1 kW – 100 W	26.4	0.46	98.26%
Step in V_3	100 W – 1k W	13.01	1.71	86.86%
	1k W – 100 W	14.15	1.67	88.20%

2.1.6 Experiment and Experimental Results

To confirm the simulation results and verify the effectiveness of the proposed decoupling controller, a physical model of the TAB converter is developed. Similar to the simulation, the converter prototype is developed using the parameters shown in Table 2.1.1. The developed TAB converter prototype is rated at 2kW and the experimental setup is shown in Fig. 2.1.22. The setup comprises a 2kW TAB converter prototype, voltage and current sensors, a DSP controller, two digital loads, and a power supply unit. The DSP controller's real-time MCU is the TMS320F28335 by Texas Instruments. The converter is set to operate at a frequency of 50 kHz. The LUT discussed in section 2.1.4 E is implemented in the DSP code. The Size of each array is limited, therefore 51 respective values are stored in each array. The PI controllers and the decoupling algorithm are implemented in the code. Four test cases of experiments are conducted under considerably worst-case scenarios with and without the proposed decoupling controller.

In test case 1, the power in V_2 is stepped up from 121 W to 927 W with and without the proposed decoupling controller. The experimental waveforms for test case 1 without the decoupling controller, are shown in Fig. 2.1.24 (a). From the waveforms, it is observed that port coupling causes a voltage undershoot of 11.2 V, and a current undershoot of 134 mA in V_3. When the proposed decoupling controller is implemented, the initial voltage undershoot is reduced to 1 V which represents a 91.07% voltage decoupling performance. The initial current undershoot is reduced to 8 mA which represents a 94.03% current decoupling performance. The estimated power decoupling performance for this test

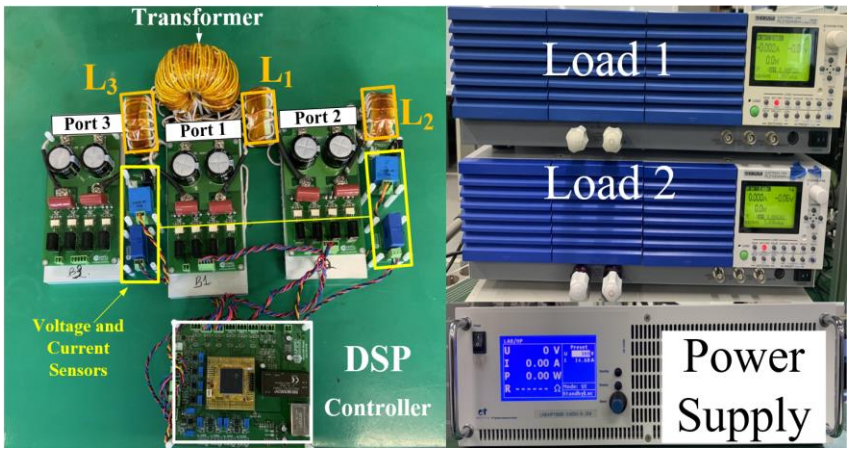

Fig. 2.1.22 Hardware setup: 2 kW TAB converter prototype, power supply unit, DC loads.

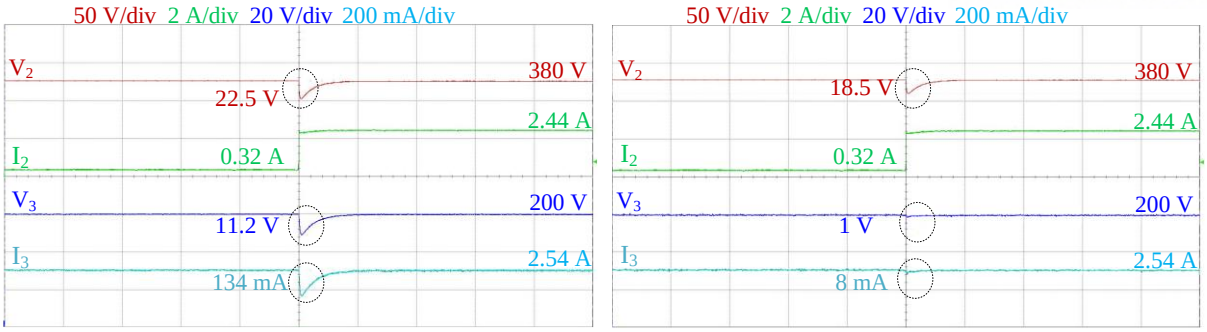

(a) (b)

Fig. 2.1.23 Experimental waveforms for test case 1 (a) without decoupling control, (b) with the proposed decoupling controller

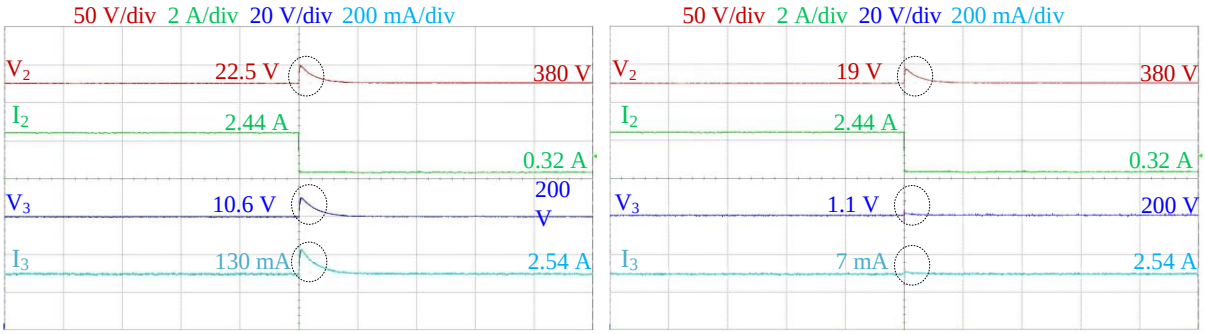

(a) (b)

Fig. 2.1.24 Experimental waveforms for test case 2 (a) without decoupling control, (b) with the proposed decoupling controller

case is about 98.67%. The experimental waveforms for test case 1 with the proposed decoupling controller are shown in Fig. 2.2.24 (b).

In test case 2, the power in V_2 is stepped down from 927 W to 121 W with and without the proposed decoupling controller. Without the decoupling controller, a voltage undershoot of 10.6 V and a current undershoot of 130 mA are observed in V_3. The experimental waveforms for test case 2 without the decoupling controller are shown in Fig 2.1.25 (a). With the proposed decoupling controller, the initial voltage undershoot is reduced to 1.1 V and the initial current undershoot is reduced to 7 mA. The results translate to an 89.62% voltage decoupling performance and a 94.62% current decoupling performance. Power decoupling performance is estimated to be 97.92%. The experimental waveforms for test case 2 without the proposed decoupling controller are shown in Fig. 2.1.25 (b).

In test case 3, the power in V_3 is stepped up from 96 W to 880 W with and without the decoupling controller. After the power step in V_3, a voltage undershoot of 9.8 V and a current undershoot of 42 mA are observed in V_2. These observations are made for the experiment without the decoupling controller. The experimental waveforms are shown in Fig. 2.1.26 (a). The proposed decoupling controller is applied in this test case and the observations are captured as shown in Fig. 2.1.26 (b). From the waveforms, the initial voltage undershoot is reduced to 1 V and the initial current undershoot is reduced to 4 mA. These results show an 89.80% voltage decoupling performance and a 90.48% current

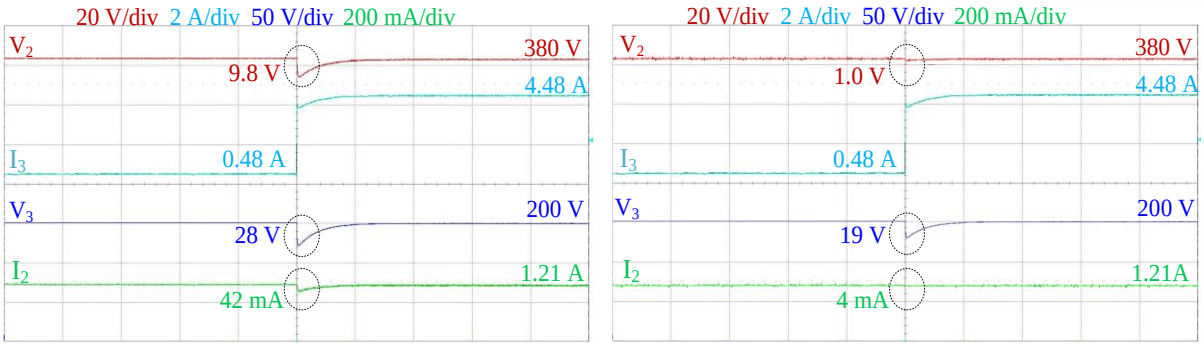

(a) (b)

Fig. 2.1.25 Experimental waveforms for test case 3 (a) without decoupling control, (b) with the proposed decoupling controller

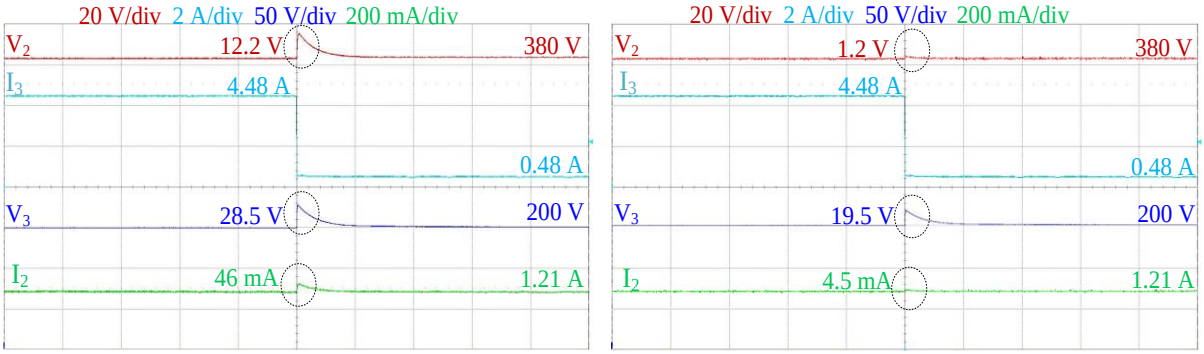

(a) (b)

Fig. 2.1.26 Experimental waveforms for test case 4 (a) without decoupling control, (b) with the proposed decoupling controller

decoupling performance. The estimated power decoupling performance is about 98.06%.

In test case 4, the power in V_3 is stepped down from 880 W to 96 W with and without the inclusion of the decoupling controller. Without the proposed decoupling controller, the step change in V_3 causes a voltage overshoot of 12.2 V and a current overshoot of 46 mA in the alternate load, V_2. The experimental waveforms for this test are shown in Fig. 2.1.27 (a). With the inclusion of the proposed decoupling controller, the initial overshoot is reduced to 1.2 V and the initial current overshoot is reduced to 4.5 mA. These results translate to a 90.16% voltage decoupling performance and a 90.22% current decoupling performance. The experimental waveforms for test case 4 with the proposed decoupling controller are shown in Fig. 2.1.27 (b). The power decoupling performance for test case 4 is estimated to be 99.04%. From the experimental results for all the 4 test cases, the proposed decoupling shows reduced coupling effects between port 2 and port 3.

Summaries of all the experimental results are provided in tables, 2.2.4 and 2.2.5. Tables 2.2.6 and 2.2.7 compare simulation and experimental results based on voltage and current, respectively. The summary tables provide experimental results captured in alternate ports according to load variations in selected ports.

Table 2.1.5: Voltage experimental results in alternate port according to load variations in selected port

	Power Step	Without decoupling (V)	With Decoupling (V)	Decoupling performance
Step in V_2	100 W – 900 W	11.2	1	91.07%
	900 W – 100 W	10.6	1.1	89.62%
Step in V_3	204 W – 900 W	9.8	1	89.80%
	900 W – 240 W	12.2	1.2	90.16%

Table 2.1.6: Voltage experimental results in alternate port according to load variations in selected port

	Power Step	Without Decoupling (mA)	With Decoupling (mA)	Decoupling performance
Step in V_2	100 W – 900 W	134	8	94.03%
	900 W – 100 W	130	7	94.62%
Step in V_3	204 W – 900 W	42	4	90.48%
	900 W – 240 W	46	4.5	90.22%

Table 2.1.7: Comparison between voltage simulation and experimental results in alternate ports according to load variations in selected port

		Simulation		Experiment	
	Power Step	Without Decoupling (V)	With Decoupling (V)	Without Decoupling (V)	With Decoupling (V)
Step in V_2	100 W – 900 W	5.23	0.27	11.2	1.0
	900 W – 100 W	5.34	0.31	10.6	1.1
Step in V_3	204 W – 900 W	5.24	0.93	9.8	1.0
	900 W – 240 W	5.43	1.05	12.2	1.2

Table 2.1.8: Comparison between current simulation and experimental results in alternate ports according to load variations in selected port

		Simulation		Experiment	
	Power Step	Without Decoupling (mA)	With Decoupling (mA)	Without Decoupling (mA)	With Decoupling (mA)
Step in V_2	100 W – 900 W	64.23	1.46	134	8
	900 W – 100 W	65.18	1.93	130	7
Step in V_3	204 W – 900 W	17.25	2.24	42	4
	900 W – 240 W	18.49	2.20	46	4.5

2.2 Power Flow Decoupling in TAB Converter for DC Microgrid Islanding Mode Operation

In this subsection, a power flow decoupling algorithm is proposed in the Triple-Active-Bridge (TAB) converter specifically for the islanding operation mode of DC microgrid systems since previous research focuses on the TAB converter decoupling for application in DC microgrid grid-connected mode operation. The bidirectional power flow property of the TAB converter makes it a good candidate for DC bus voltage regulation during islanding mode operation. For this and other benefits of the TAB converter discussed in 2.1, the TAB converter is selected in this research to regulate DC bus voltage during islanding mode. However, due to the coupling nature of all the ports, it is crucial to develop a decoupling controller for proper DC bus voltage regulation. Subsequent sections discuss the islanding operation mode of DC microgrids, DC bus voltage regulation, power flow analysis of the TAB converter in islanding mode, and the proposed power flow decoupling algorithm. Simulation and experimental results are also provided to show the effectiveness and performance of the proposed decoupling controller for DC bus voltage regulation and TAB converter power flow decoupling in the islanding mode operation of the DC microgrid.

2.2.1 DC Microgrid Operation in Islanding Mode

Islanding operation as related to DC microgrid systems is when a DC microgrid is unintentionally or intentionally disconnected from the utility grid and runs autonomously. Unintended disconnection of the microgrid may be due to fault situations in the main grid such as blackouts. Such faults can disrupt the operation of the microgrid, its distributed generations, and loads. In grid-connected mode operation, the DC bus voltage is regulated by the utility grid via an AC-DC converter. When a fault occurs in the

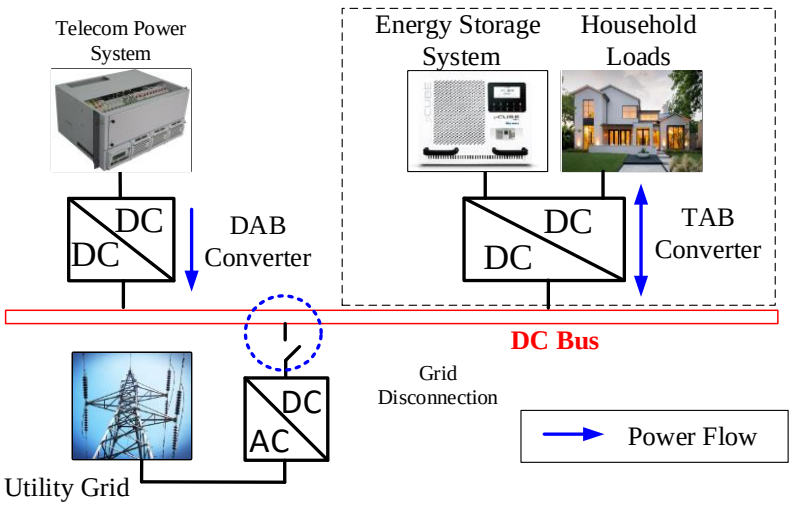

Fig. 2.2.1 A conceptual diagram of a DC microgrid operating in islanding mode

utility grid, the DC microgrid is disconnected from the utility grid and the DC microgrid operates autonomously. In this condition, the DC bus voltage must be tightly regulated to prevent the collapse of the system and to prevent damage to sensitive loads. To maximize the power density and overall efficiency of the DC microgrid, the TAB converter is selected to connect an energy source to regulate the DC bus voltage. In this research, an energy storage system (ESS) is selected to regulate the DC bus voltage during islanding mode. The inclusion of the ESS in microgrid systems aids in reducing power flow fluctuations [23]. An ESS can store and release energy to support the utility grid in grid-connected mode and it can also single-handedly supply energy to loads in DC microgrid islanding operation mode.

A conceptual diagram of the intended DC microgrid application is shown in Fig.2.2.1. The figure shows a simplified version of a DC microgrid with two loads, an ESS, a utility grid, and a VSC converter. The ESS and a load that represents a household load are connected to the DC bus using the TAB converter. Connected to the same bus is another load which is considered a sensitive load.

2.2.2 DC Bus Voltage Regulation in DC Microgrids Islanding Mode Operation

DC microgrids usually operate at a set allowable DC bus voltage range [24]. The set range allows for power balancing and high system efficiency and system stability. A DC distribution system referenced in [25] is considered for analysis. The allowable operating DC bus voltage range is from 360 V to 400 V and the nominal DC bus voltage is 380 V. Fig. 2.2.2 shows the DC bus voltage regulation scheme for the referenced DC distribution system. In grid-connected mode, when the DC bus voltage falls outside this operation range, the DC microgrid detects it as a fault and disconnects from the main grid. After disconnection from the main grid, the DC bus voltage should be regulated by a voltage source. As stated previously, an ESS is selected in this research as the voltage source device. The ESS regulates the DC bus voltage using the primary port of the TAB converter. The DC bus voltage is regulated such that it does not fall outside the nominal operating range. This ensures the continuous operation of loads, and

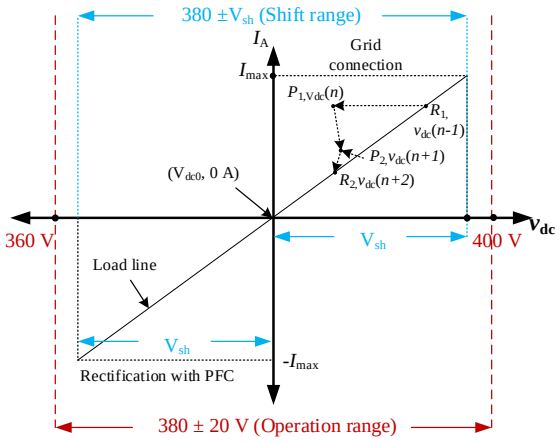

Fig. 2.2.2 Reference DC bus voltage operation range for a distribution system [25]

distributed generations and prevents the DC microgrid from collapsing.

The intended DC microgrid is a low-voltage DC microgrid, which is most suitable for applications that include sensitive loads, for example, telecom power systems [26]. Sensitive loads connected directly or indirectly to the DC bus are programmed with Undervoltage and Overvoltage protection functions that disable their operation when the DC bus voltage falls outside the allowable operating range [26]. In general, it is inimical for the DC bus voltage to exceed the allowable limits since it affects sensitive load operation, limits the DC microgrid's performance, and results in unbalanced power and system instability. It is, therefore, cardinal to regulate the DC bus voltage and keep it within the allowable operating limit. A decoupling controller is therefore proposed considering all the above-mentioned factors and the coupling nature of the TAB converter to tightly regulate DC bus voltage in islanding mode operation.

2.2.3 TAB Converter Topology and Modulation for Islanding Operation

A detailed analysis of the TAB converter topology has been provided in 2.1. The conventional TAB converter topology, which adapts three bulk inductors, is still adapted in this subsection. The implemented TAB converter is the full bridge TAB converter topology. Port 1 is connected to the DC bus, port 2 connects a load and port three connects an ESS. In grid-connected mode, port 1 is set as the reference port and port 2 and port 3 are regulated. The load's voltage is regulated, and the ESS current is regulated to charge or discharge it. In islanding mode, the ESS port is set as the reference port and ports 1 and 2 are regulated in terms of voltage. The regulation of the voltage at port 1 results in the regulation of the DC bus voltage and the implemented TAB converter is shown in Fig. 2.2.3. As established earlier, the TAB equivalent circuit model shown in Fig. 2.2.4 is used to represent the full

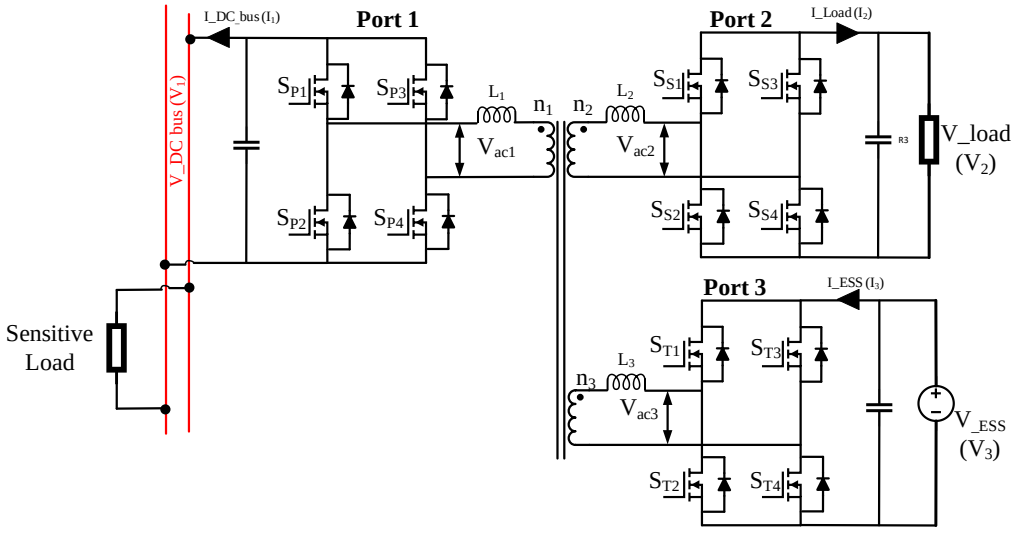

Fig. 2.2.3 Full circuit of the conventional TAB converter for Islanding mode operation.

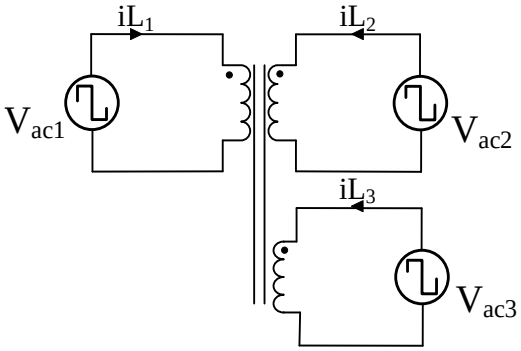

Fig. 2.2.4 Equivalent circuit model of the TAB converter

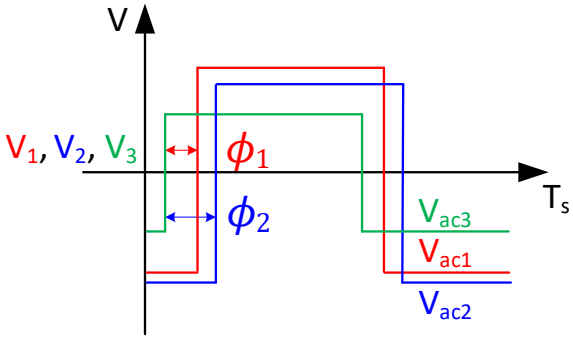

Fig. 2.2.5 Single-phase-shift modulation

topology to simplify the converter operation analysis. V_{ac1} V_{ac2} and V_{ac3} represent bridges (ports) 1, 2, and 3 respectively. With V_{ac3} set as the reference bridge, the phase displacement between V_{ac3} and V_{ac1} is represented by ϕ_1, and the phase displacement between V_{ac3} and V_{ac2} is represented by ϕ_2. The implemented TAB converter adapts the single-phase-shift modulation method for power transfer. The single-phase shift modulation in the implemented TAB converter is shown in Fig. 2.2.5. It shows the phase displacements between the square-wave voltages with V_{ac3} being the reference bridge.

2.2.4 Power Flow Analysis of the TAB Converter in Islanding Mode Operation

The delta-equivalent circuit of the TAB converter shown in Fig. 2.2.6 is used in analyzing the TAB converter's power flow in islanding mode operation. The equivalent circuit is developed by refering all ports to the tertiary port (V_3) to describe the TAB converter's power flow in DC microgrid islanding mode operation. From the model, the effective inductance equations can be established, and they are expressed below:

$$L_{32} = \frac{L_1L_2 + L_1L_3 + L_2L_3}{L_1} \tag{2.2.1}$$

$$L_{31} = \frac{L_1L_2 + L_1L_3 + L_2L_3}{L_2} \tag{2.2.2}$$

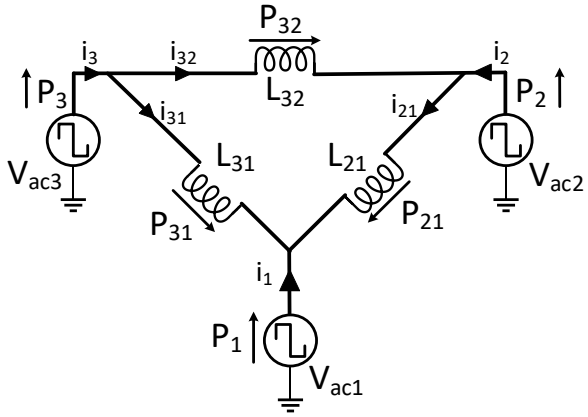

Fig. 2.2.6 Delta-equivalent circuit of the TAB converter

$$L_{21} = \frac{L_1L_2 + L_1L_3 + L_2L_3}{L_3} \tag{2.2.3}$$

Port-to-port equations established from the model are P_{32}, P_{31}, and P_{21} and they can are expressed as follows:

$$P_{31} = \frac{V_1V_3\phi_1(\pi - |\phi_1|)}{2\pi^2 f_{sw}L_{31}} \tag{2.2.4}$$

$$P_{32} = \frac{V_3V_2\phi_2(\pi - |\phi_2|)}{2\pi^2 f_{sw}L_{32}} \tag{2.2.5}$$

$$P_{21} = \frac{V_1V_3(\phi_2 - \phi_1)(\pi - |\phi_2 - \phi_1|)}{2\pi^2 f_{sw}L_{21}} \tag{2.2.6}$$

The total active powers at ports 3, 2, and 1 are represented as P_3, P_2, and P_1 respectively, and can be expressed as follows:

$$P_1 = \frac{V_1V_3L_2\phi_1(\pi - |\phi_1|) + V_1V_2L_3(\phi_1 - \phi_2)(\pi - |\phi_1 - \phi_2|)}{2\pi^2 f_{sw}(L_1L_2 + L_1L_3 + L_2L_3)} \tag{2.2.9}$$

$$P_2 = \frac{V_2V_3L_1\phi_2(\pi - |\phi_2|) + V_1V_2L_3(\phi_2 - \phi_1)(\pi - |\phi_2 - \phi_1|)}{2\pi^2 f_{sw}(L_1L_2 + L_1L_3 + L_2L_3)} \tag{2.2.8}$$

$$P_3 = \frac{V_2V_3L_1\phi_2(\pi - |\phi_2|) + V_1V_3L_2\phi_1(\pi - |\phi_1|)}{2\pi^2 f_{sw}(L_1L_2 + L_1L_3 + L_2L_3)} \tag{2.2.7}$$

Where, $P_1 = -P_{31}-P_{21}$, $P_2 = -P_{32}+P_{21}$ and $P_3 = P_{32}+ P_{31}$

2.2.5 Proposed Decoupling Controller

As discussed in subsection 2.1, a linearized model of the TAB converter is derived to design the proposed decoupling controller. In islanding mode, the controlled ports are port 1 and port 2 and based on the topology of the TAB converter shown in Fig. 2.2.3, an average model is derived as represented in Fig. 2.2.7. The linearization process is similar to the linearization of the TAB converter done in section 2.1. The output currents I_1 and I_2 of the respective controlled ports, are derived from (2.2.8) and (2.2.9) and expressed below:

$$I_2 = \frac{V_3 L_1 \phi_2 (\pi - |\phi_2|)}{2\pi^2 f_{sw} L_{32}} + \frac{V_1 L_3 (\phi_2 - \phi_1)(\pi - |\phi_2 - \phi_1|)}{2\pi^2 f_{sw} L_{21}} \tag{2.2.10}$$

$$I_1 = \frac{V_3 L_2 \phi_1 (\pi - |\phi_1|)}{2\pi^2 f_{sw} L_{31}} + \frac{V_2 L_3 (\phi_1 - \phi_2)(\pi - |\phi_1 - \phi_2|)}{2\pi^2 f_{sw} L_{21}} \tag{2.2.11}$$

The quadratic terms in the equations (2.2.10) and (2.2.10) are simplified using the sinusoidal approximation, (2.1.19) and the resulting simplified current equations are expressed as follows:

$$I_2 = \frac{V_3 L_1 \sin(\phi_2)}{2\pi^2 f_{sw} L_{32}} + \frac{V_1 L_3 \sin(\phi_2 - \phi_1)}{2\pi^2 f_{sw} L_{21}} \tag{2.2.12}$$

$$I_1 = \frac{V_3 L_2 \sin(\phi_1)}{2\pi^2 f_{sw} L_{31}} + \frac{V_2 L_3 \sin(\phi_1 - \phi_2)}{2\pi^2 f_{sw} L_{21}} \tag{2.2.13}$$

I_2 is expressed as a sum of its steady-state value and small-signal variations as shown in (2.2.14) and the Taylor series operation of I_2 about an operating point (^) leads to (2.2.15).

$$I_2 = I_{2^\wedge} + \Delta I_2 \tag{2.2.14}$$

$$I_2 = \left[\frac{V_3 \sin(\phi_{2^\wedge})}{\frac{1}{4}\pi^3 f_{sw} L_{32}} + \frac{V_1 \sin(\phi_{2^\wedge} - \phi_{1^\wedge})}{\frac{1}{4}\pi^3 f_{sw} L_{21}} \right] + \left[\frac{V_3 \cos(\phi_{2^\wedge})\Delta\phi_2}{\frac{1}{4}\pi^3 f_{sw} L_{32}} + \frac{V_1 \cos(\phi_{2^\wedge} - \phi_{1^\wedge})\Delta\phi_2}{\frac{1}{4}\pi^3 f_{sw} L_{21}} - \frac{V_1 \cos(\phi_{2^\wedge} - \phi_{1^\wedge})\Delta\phi_1}{\frac{1}{4}\pi^3 f_{sw} L_{21}} \right] \tag{2.2.15}$$

In a similar procedure, I_1 is expressed as a sum of the steady-state value and small-signal variations as shown in (2.2.16) and the Taylor series operation of I_1 about an operating point (^) result in (2.2.17).

$$I_1 = I_{1^\wedge} + \Delta I_1 \tag{2.2.16}$$

$$I_1 = \left[\frac{V_3 \sin(\phi_{1^\wedge})}{\frac{1}{4}\pi^3 f_{sw} L_{31}} + \frac{V_2 \sin(\phi_{1^\wedge} - \phi_{2^\wedge})}{\frac{1}{4}\pi^3 f_{sw} L_{21}} \right] + \left[-\frac{V_2 \cos(\phi_{1^\wedge} - \phi_{2^\wedge})\Delta\phi_2}{\frac{1}{4}\pi^3 f_{sw} L_{21}} + \frac{V_3 \cos(\phi_{1^\wedge})\Delta\phi_1}{\frac{1}{4}\pi^3 f_{sw} L_{31}} + \frac{V_2 \cos(\phi_{1^\wedge} - \phi_{2^\wedge})\Delta\phi_1}{\frac{1}{4}\pi^3 f_{sw} L_{21}} \right] \tag{2.2.17}$$

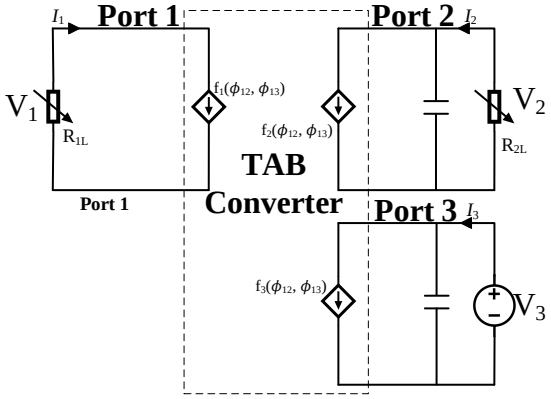

Fig. 2.2.7 Average model of the implemented TAB converter

The current equations are expressed in terms of their steady-state values and gain matrix transfer function-phase relationship as shown below:

$$I_2 = I_{2\wedge} + H'_{11}\Delta\phi_2 + H'_{12}\Delta\phi_1 \tag{2.1.28}$$

$$I_1 = I_{1\wedge} + H'_{21}\Delta\phi_2 + H'_{22}\Delta\phi_1 \tag{2.1.29}$$

Deducing from (2.2.15), (2.217), (2.2.28), and (2.2.29), the individual gain matrix element equations of the operating point-based linearized model of the TAB converter can be expressed as follows:

$$H'_{11} = \frac{V_3 L_1 \cos(\phi_{2\wedge}) + V_1 L_3 \cos(\phi_{2\wedge} - \phi_{1\wedge})}{\frac{1}{4}\pi^3 f_{sw}(L_1L_2 + L_1L_3 + L_2L_3)} \tag{2.2.30}$$

$$H'_{12} = \frac{-V_1 L_3 \cos(\phi_{2\wedge} - \phi_{1\wedge})}{\frac{1}{4}\pi^3 f_{sw}(L_1L_2 + L_1L_3 + L_2L_3)} \tag{2.2.31}$$

$$H'_{21} = \frac{-V_2 L_3 \cos(\phi_{1\wedge} - \phi_{2\wedge})}{\frac{1}{4}\pi^3 f_{sw}(L_1L_2 + L_1L_3 + L_2L_3)} \tag{2.2.32}$$

$$H'_{22} = \frac{V_3 L_2 \cos(\phi_{1\wedge}) + V_2 L_3 \cos(\phi_{1\wedge} - \phi_{2\wedge})}{\frac{1}{4}\pi^3 f_{sw}(L_1L_2 + L_1L_3 + L_2L_3)} \tag{2.2.33}$$

The control-to-output matrix equation of the linearized model is established as follows:

$$\begin{bmatrix} \Delta I_2 \\ \Delta I_1 \end{bmatrix} = \begin{bmatrix} H'_{11} & H'_{12} \\ H'_{21} & H'_{22} \end{bmatrix} \begin{bmatrix} \phi_2 \\ \phi_1 \end{bmatrix} = H' \vec{\phi} \tag{2.2.34}$$

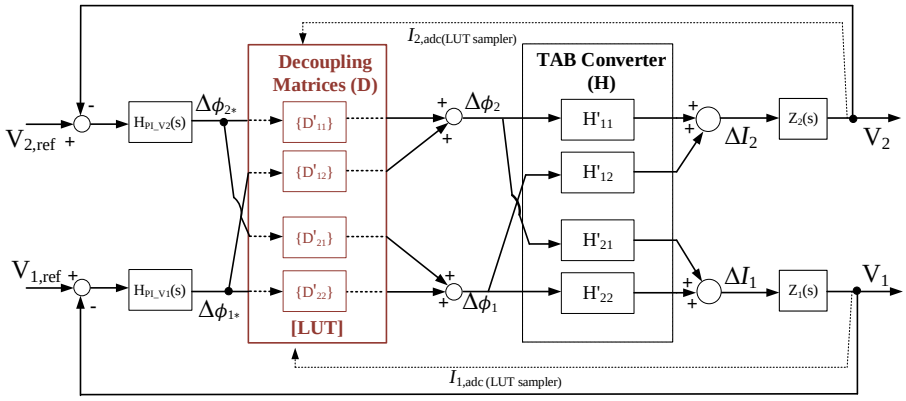

Fig. 2.2.8 Block diagram of the proposed decoupling controller.

To decouple the controller, the inverse of the gain matrix (H') for each selected operating point (^) is calculated to represent networks of operating point-dependent decoupling matrices. A decoupling matrix (D') is calculated as follows:

$$D' = \begin{bmatrix} D'_{11} & D'_{12} \\ D'_{21} & D'_{22} \end{bmatrix} = H'^{-1} = \frac{1}{H'_{11}H'_{22} - H'_{12}H'_{21}} \begin{bmatrix} H'_{22} & -H'_{12} \\ -H'_{21} & H'_{11} \end{bmatrix} \tag{2.2.35}$$

The inclusion of the decoupling matrix network results in new phase displacement variables ϕ_{1*} and ϕ_{2*} and the decoupling controller can be expressed as the control-to-output system matrix shown below:

$$\begin{bmatrix} \Delta I_2 \\ \Delta I_1 \end{bmatrix} = \begin{bmatrix} D'_{11} & D'_{12} \\ D'_{21} & D'_{22} \end{bmatrix} \begin{bmatrix} H'_{11} & H'_{12} \\ H'_{21} & H'_{22} \end{bmatrix} \begin{bmatrix} \Delta\phi_{2*} \\ \Delta\phi_{1*} \end{bmatrix} = \begin{bmatrix} 1 & 0 \\ 0 & 1 \end{bmatrix} \begin{bmatrix} \Delta\phi_{2*} \\ \Delta\phi_{1*} \end{bmatrix} \tag{2.2.36}$$

The resulting proposed decoupling controller is shown in Fig. 2.2.8. It consists of a LUT that stores pre-calculated decoupling matrices and two PI controllers for regulating power and voltage at the controlled ports 1 and 2. The two PI controllers are represented by $H_{PI\_V1}(s)$ and $H_{PI\_V2}(s)$. The output impedance of port 1 is represented by $Z_1(s)$ and the output impedance of port 2 is represented by $Z_2(s)$. The decoupling controller ensures dynamic decoupling of the TAB for effective DC bus voltage regulation.

The implemented Look-Up table (LUT) in this subsection is similar to the implemented LUT in section 2.1 except for changes in values and array matching. The structure of the implemented LUT is shown in Fig 2.2.9 (a). In this LUT, the individual arrays are I_1, I_2, D_{11}, D_{12}, D_{21}, and D_{22}. I_1 and I_2 represent the index arrays used for sorting through the decoupling matrix arrays. I_1 is paired with D_{12} and D_{22}, and I_2 is paired with D_{11} and D_{21}. With the C pointer algorithm, the sampled ADC currents, $I_{1,adc}$ and $I_{2,adc}$, which represent the inputs are referenced to sort matching values in the index arrays. The corresponding array pair elements are returned as outputs which are sent to the controller. The index values are calculated according to the port voltage and power level to match the corresponding

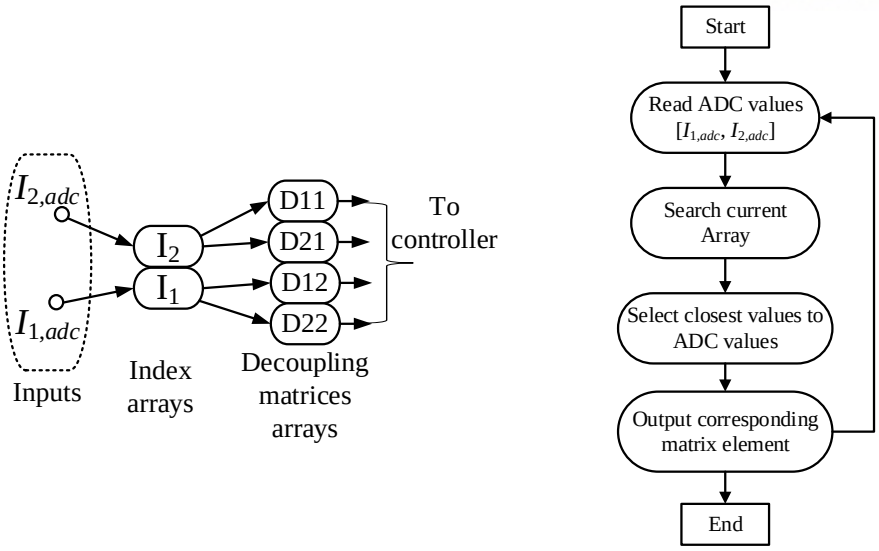

Fig. 2.2.9 Diagrams of the implemented LUT: (a) Structure of the LUT, (b) Flowchart of the look-up table operation

decoupling matrices values. From the LUT operational flowchart shown in Fig. 2.2.9 (b), the sampled current values, $I_{1,adc}$ and $I_{2,adc}$ are read by the controller, and matrix element extraction is done according to the C pointer search algorithm but with a modification, whereby the selected index values are the closest to the input values. This makes up for value differences that result from different decimal points. It also ensures that decoupling matrices are returned to the controller at any operating point in the TAB converter operation.

2.2.6 Simulation and Simulation Results

A model of the intended TAB converter topology for application in the islanding operation mode of the DC microgrid is simulated using PSIM. The simulation is conducted for the TAB converter to operate at a frequency of 50 kHz. The ESS voltage is set at 200 V, the secondary port's load (V_2) is set at 380 V and the DC bus nominal voltage is set at 380 V. The external inductors at ports 1,2. and 3 have inductance values of 62µH, 59µH, and 35µH, respectively. A summary of the simulation parameters is provided in Table 2.2.1. V_1 is displayed as V_DC_bus and V_2 is displayed as V_load (V_2) and corresponding power values as P_DC_bus (P_1) and P_load (P_2) and corresponding current values as I_DC_bus (I_1) and I_load (I_2). To imitate the simplified DC microgrid shown in Fig 2.2.1, a sensitive load is connected directly to the DC bus, as shown in Fig. 2.2.3. With this setup, the proposed decoupling controller is tested for its effectiveness and performance for DC bus voltage regulation and port power flow decoupling. Fig. 2.2.10 shows the PSIM simulation model for verifying the proposed decoupling controller. For the simulation conducted, power was varied in V_2 from 100 W to 1 kW and then back to 100 W with and without the proposed decoupling controller. The sensitive load is set to operate at a power level of 500 W. Simulation waveforms are captured for voltage, current, and power

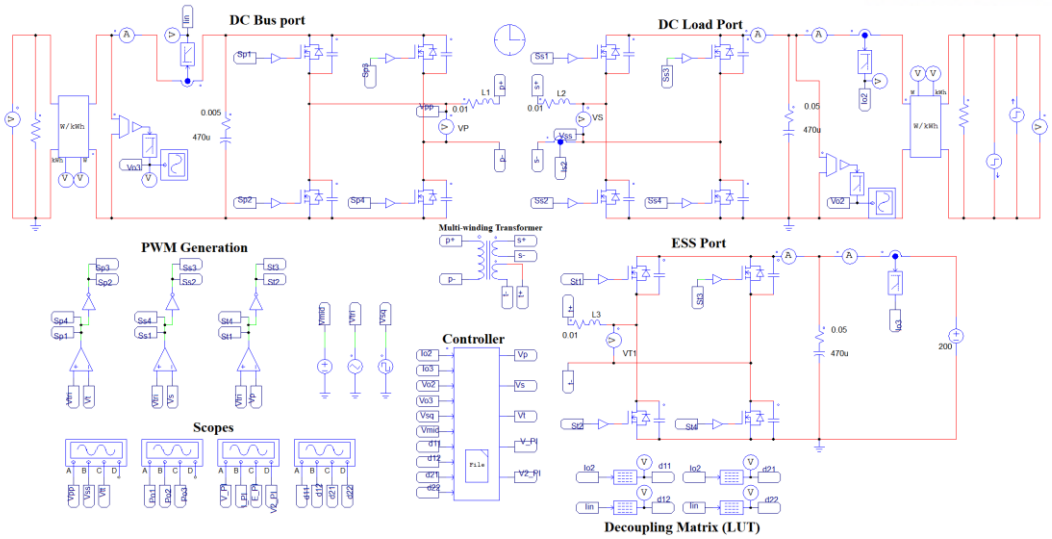

Fig. 2.2.10 Simulation setup using PSIM software

Table 2.2.1: Simulation and Experiment Parameters

Parameter	Symbol	Value	Unit
Port 1 voltage (DC bus)	V_1	380	V
Port 2 voltage (load)	V_2	380	V
Port 3 voltage (ESS)	V_3	200	V
Bulk inductors	L_1	62	µH
	L_2	59	µH
	L_3	35	µH
Switching frequency	f_{sw}	50	kHz
Turn ratio	n1:n2:n3	1:1:0.526	

profiles in the TAB converter operation. Power is stepped up in V_2 at 1s and stepped down at 1.7s. Without decoupling control, the power step from 100 W to 1 kW in V_2 causes a voltage undershoot of 31.66 V in V_2. Due to port coupling, a corresponding voltage undershoot of 2 V is observed in the DC bus. When the power in V_2 is stepped down from 1 kW to 100 W, a voltage overshoot of 36.71 V is observed in V_2 without the decoupling controller. The coupling nature of the ports also results in a voltage overshoot of 29.67 V in the DC bus. The simulation waveforms for the voltages without decoupling control are shown in Fig. 2.2.11 (a). With the proposed decoupling controller, the initial DC bus voltage undershoot for power step-up (100 W -1 kW) is reduced to 1.61 V which represents a 93.55 % voltage decoupling performance. For power step down (1 kW -100 W), the initial DC bus voltage undershoot is reduced to 1.69 V which represents a 94.30% voltage decoupling performance. The simulation waveforms for the voltages with decoupling control are shown in Fig. 2.2.11 (b).

For the current simulation, a current undershoot of 86 mA is observed in the Dc bus when power in V_2 is stepped up from 100 W to 1 kW without decoupling control. When the power is stepped down from 1 kW to 100 W, a current overshoot of 102 mA is observed in the DC bus. The simulation

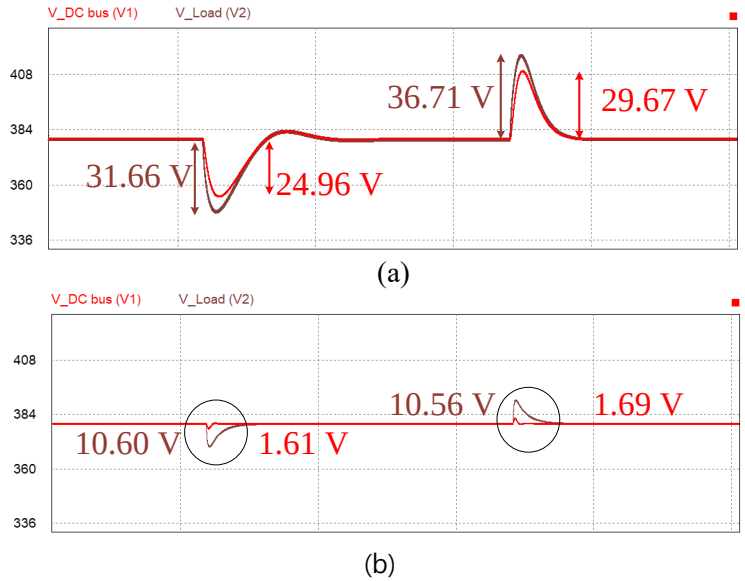

Fig. 2.2.11 Simulated DC bus and load voltage waveforms under load steps: (a) without decoupling control (b) with decoupling control.

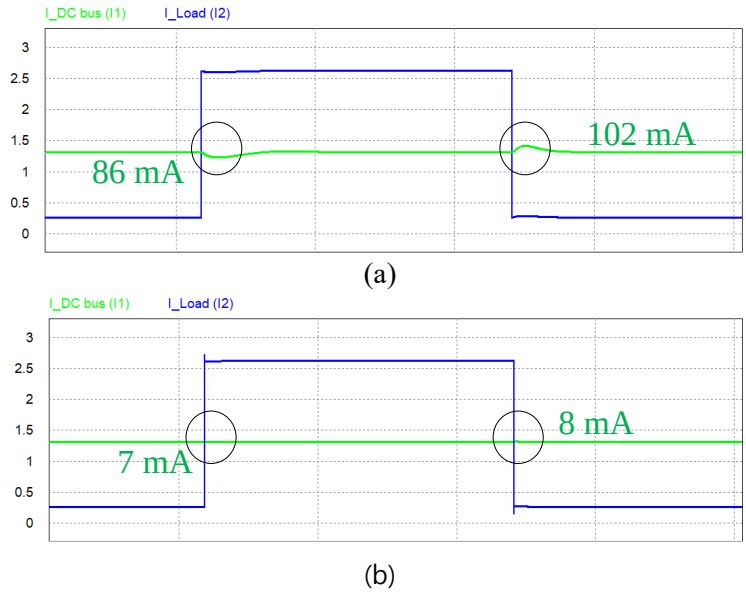

Fig. 2.2.12 Simulated DC bus and load current waveforms under load steps: (a) without decoupling control (b) with decoupling control.

waveform for the current without decoupling control is shown in Fig. 2.2.12 (a). When the power in V_2 is stepped up (100 W – 1 kW) with the decoupling controller, the initial current undershoot is reduced to 7 mA which represents a 91.86% current decoupling performance. For power step down (1 kW – 100 W) in V_2, the initial current overshoot is reduced to 8 mA which represents a 92.16% current decoupling performance. The simulation waveform for the current with the proposed decoupling control is shown in Fig. 2.2.12 (b).

In terms of power, a power undershoot of 63.4 W is observed in the DC bus when the power in V_2 is stepped up from 100 W to 1 k W without decoupling control. A power overshoot of 80.1 W is captured

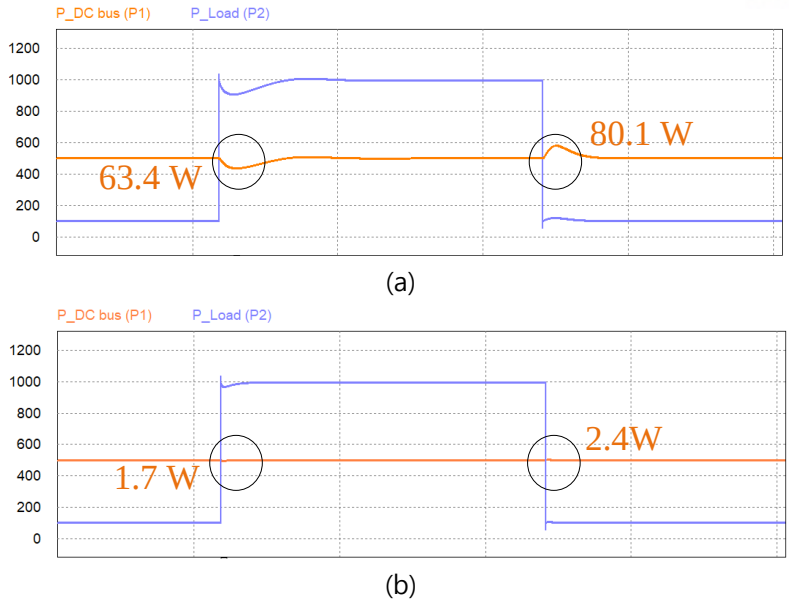

Fig. 2.2.13 Simulated DC bus and load power waveforms under load steps: (a) without decoupling control (b) with decoupling control.

in the DC bus when the power in V_2 is stepped down from 1 kW to 100 W. The simulation waveforms for the power without decoupling control are shown in Fig. 2.2.13 (a). With the decoupling controller, the initial DC bus power undershoot is reduced to 1.7 W which translates to a 97.32 % power decoupling performance. For power step down in V_2 (1 kW – 100 W), the initial power overshoot is reduced to 2.4 W which represents a 97.00 % power decoupling performance. The simulation waveforms for the power with decoupling control are shown in Fig. 2.2.13 (b). As an additional advantage of the proposed decoupling controller, improved dynamic performance of the system is observed as the initial voltage undershoot and overshoots in V_2 are reduced to 10.60 V and 10.56 V, respectively. These represent a 66.52 % undershoot reduction and a 71.20 % overshoot reduction. This condition is investigated in the experiment. Summaries of the simulation results are provided in tables 2.2.2, 2.2.3, and 2.2.4.

Table 2.2.2: Voltage simulation results in DC bus according to load variation in V_2

	Power Step	Without decoupling	With decoupling	Decoupling performance
Step in Load 1	100 W – 1 kW	24.96 V	1.61 V	93.55 %
	1 kW – 100 W	29.67 V	1.69 V	94.30 %

Table 2.2.3: Current simulation results in DC bus according to load variation in V_2

	Power Step	Without decoupling	With decoupling	Decoupling performance
Step in Load 1	100 W – 1 kW	86 mA	7 mA	91.86 %
	1 kW – 100 W	102 mA	8 mA	92.16 %

Table 2.2.4 Power simulation results in DC bus according to load variation in V_2

	Power Step	Without decoupling	With decoupling	Decoupling performance
Step in Load 1	100 W – 1 kW	63.4 W	1.7 W	97.32 %
	1 kW – 100 W	80.1 W	2.4 W	97.00 %

2.2.7 Experiment and Experimental Waveforms

A 2 kW TAB hardware prototype is implemented to verify the proposed decoupling controller by experiment. The hardware setup for the experiment is shown in Fig 2.2.14. It consists of the TAB converter prototype, a PCUBE ESS emulator, and two DC loads. One of the DC loads represents V_2 and the other represents a sensitive load. Like the simulation model, the sensitive load is connected to the DC bus, and it is set to operate at 501.6 W. The decoupling algorithm is implemented in the DSP controller and the experiment is conducted with the TAB converter operating at 50 kHz. Two test cases are carried out and in each of the test cases, the converter operates with and without the decoupling controller. Step changes are carried out in V_2 to observe the coupling effects on the DC bus voltage and current. The experiment is conducted considering worst-case scenarios and the resulting experimental waveforms are captured and analyzed.

In test case 1, power in V_2 is stepped up from 101.8 W to 900.98 W with and without the proposed decoupling controller. Without the decoupling controller, a voltage undershoot of 38 V is observed in V_2. In the DC bus, a corresponding voltage undershoot of 28.5 V is captured and a current undershoot of 100 mA is also observed. The experimental waveform for this test case without the decoupling controller is shown in Fig 2.2.15 (a). When the decoupling controller is applied, the initial DC bus voltage undershoot is reduced to 2.3 V. This translates to a 91.93 % voltage decoupling performance. The initial current undershoot is also reduced to 13 mA and this represents an 87.00 % current decoupling performance. The experimental waveform for this test case with the decoupling controller

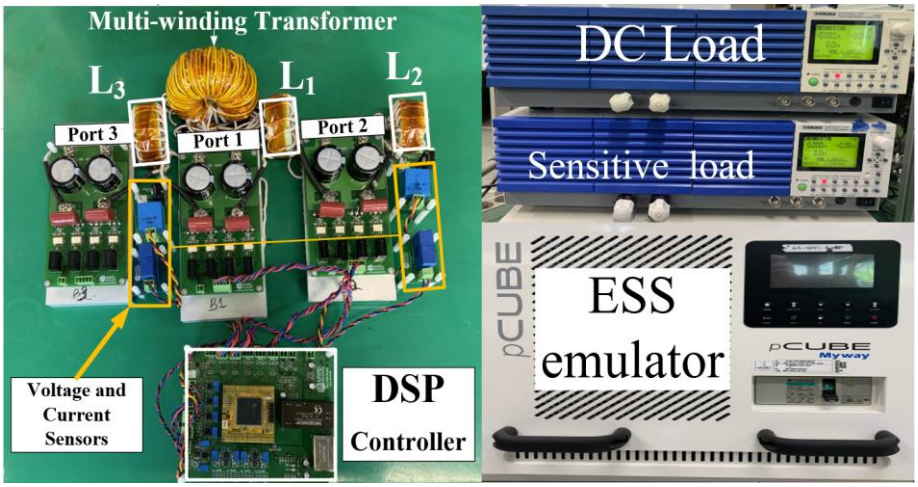

Fig. 2.2.14 Experimental setup: 2kW TAB converter prototype, PCUBE ESS emulator, DC loads.

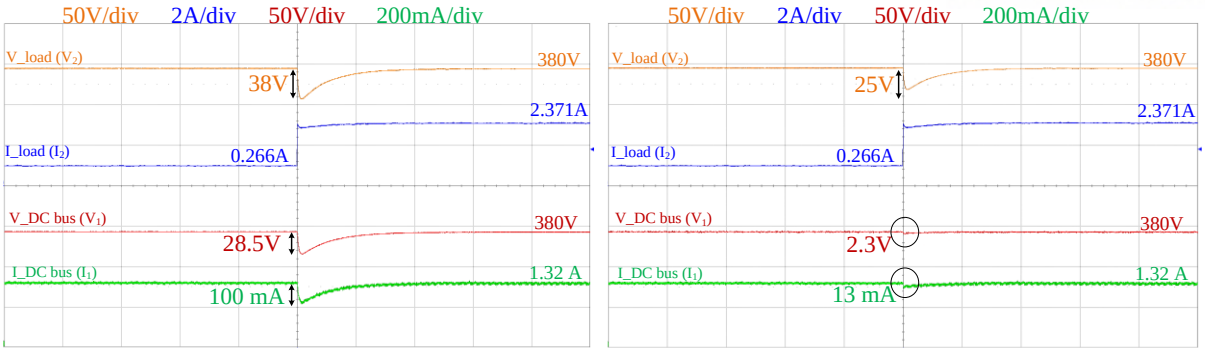

(a) (b)

Fig. 2.2.15 Experimental waveforms for step-up in V_2: (a) without decoupling control (b) with proposed decoupling controller.

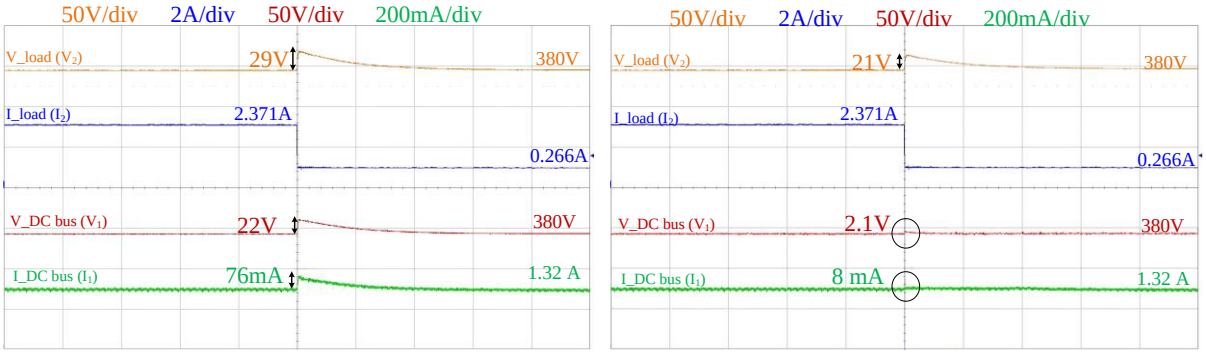

(a) (b)

Fig. 2.2.16 Experimental waveforms for step-down in V_2: (a) without decoupling control (b) with proposed decoupling controller.

is shown in Fig. 2.2.15 (b). Power decoupling performance can be estimated to be 98.95%. As observed in the simulation, the initial undershoot in V_2 is also reduced to 25 V which translates into a 34.21% undershoot reduction.

In test case 2, power in V_2 was stepped down from 900.98 W to 101.8 W with and without the proposed decoupling controller. A voltage overshoot of 29 V is observed in V_2 without the decoupling controller. A 22 V overshoot and a corresponding current overshoot of 76 mA are captured in the DC bus. The experimental waveform for this test case without the decoupling controller is shown in Fig 2.2.16 (a). With the decoupling Controller, the initial voltage overshoot in the DC bus is reduced to 2.1 V and this represents a 90.45 % voltage decoupling performance. The initial current overshoot is reduced to 8 mA which represents an 89.47 % current decoupling performance. The experimental waveform for this test case with the decoupling controller is shown in Fig 2.2.16 (b). Power decoupling performance can be estimated to be 95.47 %. Again, the voltage overshoot in V_2 is reduced to 21 V which represents a 27.59 % overshoot reduction.

Table 2.2.5 DC bus voltage experimental results according to load variation in V_2

	Power Step	Without decoupling	With decoupling	Decoupling performance
Step in V_2	104 W – 901 W	28.5 V	2.3 V	91.93%
	901 W – 104 W	22.0 V	2.1 V	90.45%

Table 2.2.6 DC bus current experimental results according to load variation in V_2

	Power Step	Without decoupling	With decoupling	Decoupling performance
Step in V_2	104 W – 901 W	100 mA	13 mA	87.00%
	901 W – 104 W	76 mA	8 mA	89.47%

Table 2.2.7: Comparison between DC bus voltage simulation and experimental results

		Simulation		Experiment	
	Power Step	Without Decoupling	With Decoupling	Without Decoupling	With Decoupling
Step in V_2	100 W – 900 W	24.96 V	1.61 V	28.5 V	2.3 V
	900 W – 100 W	29.67 V	1.69 V	22.0 V	2.1 V

Table 2.2.8: Comparison between DC bus current simulation and experimental results

		Simulation		Experiment	
	Power Step	Without Decoupling	With Decoupling	Without Decoupling	With Decoupling
Step in V_2	100 W – 900 W	86 mA	7 mA	100 mA	13 mA
	900 W – 100 W	102 mA	8 mA	76 mA	8 mA

overshoot reduction.

Summaries of all the experimental results are provided in tables 2.2.5 and 2.2.6. Tables 2.2.7 and 2.2.8 compares the simulation and experimental results according to voltage and current, respectively. The experimental results show the effectiveness of the proposed decoupling algorithm in TAB converters for DC bus voltage regulation. Without the decoupling controller, all the voltage shoots in the DC bus exceed the allowable operating limits referred to in [25]. With the decoupling controller, the DC bus voltage is well regulated and kept within the allowable operating range. Also, the controller improves the overall dynamic performance of the TAB converter by reducing all step-related voltage undershoots and overshoots consequently improving the converter's power efficiency.

The improved TAB converter dynamic response which is featured by the reduction of voltage undershoots and overshoots in the stepped loads can be attributed to the decomposition of the DIDO controller into SISO controllers. When power is stepped down or up, the variation in output impedance according to the power level results in voltage overshoot and undershoot, respectively. The controller increases or decreases phase shift values to match up to the new power levels. Due to the hidden feedback loops that characterize the coupled controller, the phase shifts are also coupled. The coupled controller leads to phase shift adjustments that are more or lesser than required, leading to higher voltage undershoots and overshoots. With the decoupled controller, the phase shift adjustments are close to their expected due to minimal to no interaction between the feedback loops.

For all the sections, the difference that exists between the simulation and experimental results is due to the inability to replicate the exact experimental environment in the simulation model. Other factors include errors in the converter model, inherent impedances in load and power source, PCB, parasitic components, and ADC sampling differences.

2.2.8 Comparison with Existing Decoupling Methods.

The proposed decoupling controller is compared to existing decoupling methods according to metrics such as design complexity, decoupler type, degrees of freedom, type of feedback controller used, and the computational burden on digital controllers. All other methods are complicated in design and difficult to implement as compared to the proposed method. [10] adapts the decoupling matrix method but the decoupler design is based on the optimum operating point and hence may fail if the converter operates at different operating points. The proposed decoupling matrices networks consider various operating points and therefore dynamically decouple the converter. Simulations of comparison of the proposed decoupling controller are provided in Appendix C. Compared to the methods referenced, the proposed controller utilizes only two degrees of freedom to achieve decoupling and port regulation whiles the other methods use five degrees of freedom. Moreover, the proposed method makes use of the least number of feedback controllers as compared to the other methods. A summary of the comparison is provided in table 2.2.9.

Table 2.2.9: Comparison with existing decoupling methods

Decoupling method	**Design complexity**	**Decoupler type**	**Degrees of freedom**	**Feedback controller**	**Controller computation burden**
Zhao, et al. [10]	High	Constant decoupling matrix	Duty cycle (3) Phase (2)	PI controller (3)	Medium
Wang.et al. [11]	High	Controller bandwidth design	Duty cycle (3) Phase (2)	PI controller (4)	Medium
I. Bisis.et al. [12]	Very high	Small signal model-based constant decoupling matrix	Duty cycle (3) Phase (2)	State feedback controller: PI controller (5)	Very high
Proposed method	Low	Dynamic decoupling matrices	Phase (2)	PI controller (2)	Low

III. Power Flow Decoupling in Quadruple-Active-Bridge (QAB) Converter for DC Microgrid Grid-Connected Mode Operation.

3.1 Quadruple-Active-Bridge Converter Topology and Modulation

The Quadrupled-Active-Bridge (QAB) converter is an extended version of the DAB converter. It is made up of four active bridge converters interconnected by a single four-winding transformer and functions as a single converter unit. In the full bridge model employed in this research, the converter makes use of four external bulk inductors which represent leakage inductance elements. The converter makes use of the transformer's inherent leakage inductance together with the external bulk inductors as energy transfer elements. Because the QAB converter is an extension of the DAB converter, it also possesses qualities such as bidirectional flow and high power density. The use of magnetic coupling in the QAB's topology ensures galvanic isolation and port voltage matching capability [19]. The full bridge QAB converter model used in this research has four power switches per full bridge, and switches on the same leg in a bridge operate in a complementary manner to generate AC square wave voltages at the transformer terminals. The implemented QAB converter topology is shown in Fig. 3.1.

The QAB converter topology can be replaced with a simplified equivalent model shown in Fig. 3.2 for operational analysis. Each full bridge converter can be replaced with a square wave voltage interconnected by the high-frequency transformer. According to Fig. 3.2, the primary bridge is represented by U_1, the secondary bridge by U_2, the tertiary bridge by U_3, and the quaternary bridge by U_4. For power transfer among bridges, the implemented QAB converter adapts the single-phase-shift (SPS) modulation method. The concept of the SPS modulation technique according to power transfer

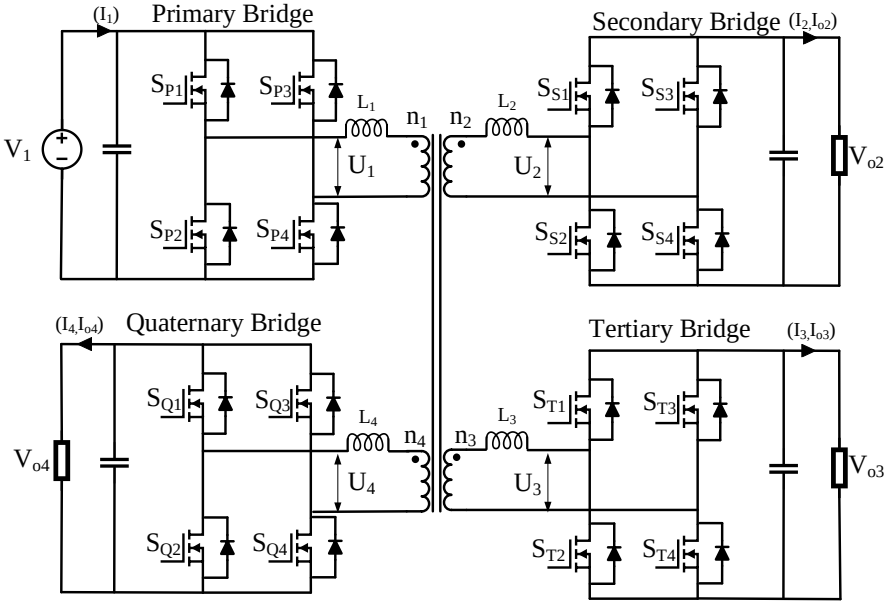

Fig. 3.1 Full circuit of the quadruple-active-bridge (QAB) converter

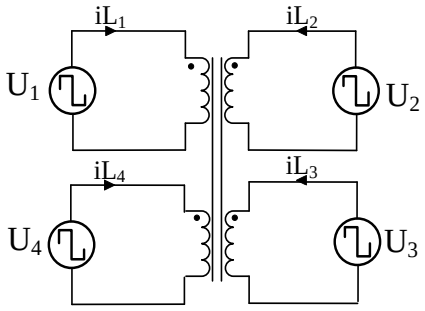

Fig. 3.2 Equivalent circuit of the QAB converter

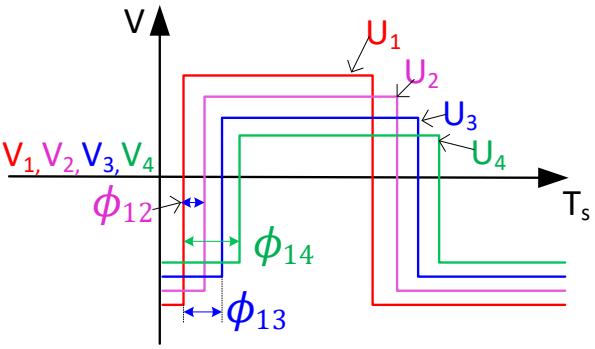

Fig. 3.3 Single-Phase-Shift modulation

in the QAB converter is shown in Fig. 3.3. The phase displacements between U_1 and U_2, between U_1 and U_3, and between U_1 and U_4 are represented denoted as ϕ_{12}, ϕ_{13}, and ϕ_{14}, respectively. Power is delivered from the reference bridge (U_1) to the other bridges and the magnitude of power transfer between two bridges is directly proportional to the phase displacement values between them. The QAB converter is designed to keep maximum power at a phase displacement angle of $\pi/2$.

3.2 Power Flow Analysis

The QAB converter can be represented as a network of inductors that are linked to the bridges by the high-frequency multi-winding transformer. The QAB has a more complicated network of inductors as related to power flow. An equivalent cantilever model [20] is used to represent the complex power flow structure of the converter. The model depicts the power flow via a network of inductors and the total active power at each port is a summation of the power flows through the inductors linked to respective ports. The cantilever equivalent model shown in Fig. 3.4 is derived by referring all parameters to U_1. The effective inductances responsible for power flow between the bridges can be expressed mathematically as follows:

$$L_{12} = \frac{L_1L_2L_3 + L_1L_2L_4 + L_1L_3L_4 + L_2L_3L_4}{L_3L_4} \tag{3.1}$$

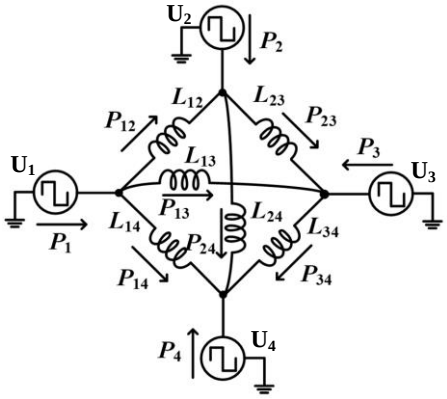

Fig. 3.4 Equivalent cantilever model of the QAB converter.

$$L_{13} = \frac{L_1L_2L_3 + L_1L_2L_4 + L_1L_3L_4 + L_2L_3L_4}{L_2L_4} \tag{3.2}$$

$$L_{14} = \frac{L_1L_2L_3 + L_1L_2L_4 + L_1L_3L_4 + L_2L_3L_4}{L_2L_3} \tag{3.3}$$

$$L_{23} = \frac{L_1L_2L_3 + L_1L_2L_4 + L_1L_3L_4 + L_2L_3L_4}{L_1L_4} \tag{3.4}$$

$$L_{24} = \frac{L_1L_2L_3 + L_1L_2L_4 + L_1L_3L_4 + L_2L_3L_4}{L_1L_3} \tag{3.5}$$

$$L_{34} = \frac{L_1L_2L_3 + L_1L_2L_4 + L_1L_3L_4 + L_2L_3L_4}{L_1L_2} \tag{3.6}$$

According to the cantilever model, the port-to-port power flows can be derived and expressed based on the primary equations established in [21] as follows:

$$P_{12} = \frac{V_1V_2}{2\pi^2 f_{sw}L_{12}}\phi_{12}(\pi - |\phi_{12}|) \tag{3.7}$$

$$P_{13} = \frac{V_1V_3}{2\pi^2 f_{sw}L_{13}}\phi_{13}(\pi - |\phi_{13}|) \tag{3.8}$$

$$P_{14} = \frac{V_1V_4}{2\pi^2 f_{sw}L_{14}}\phi_{14}(\pi - |\phi_{14}|) \tag{3.9}$$

$$P_{23} = \frac{V_2V_3}{2\pi^2 f_{sw}L_{23}}(\phi_{13} - \phi_{12})(\pi - |\phi_{13} - \phi_{12}|) \tag{3.10}$$

$$P_{24} = \frac{V_2V_4}{2\pi^2 f_{sw}L_{24}}(\phi_{14} - \phi_{12})(\pi - |\phi_{14} - \phi_{12}|) \tag{3.11}$$

$$P_{34} = \frac{V_3V_4}{2\pi^2 f_{sw}L_{34}}(\phi_{14} - \phi_{13})(\pi - |\phi_{14} - \phi_{13}|) \tag{3.12}$$

By the summation of power flows referenced from Fig. 3.4, the total active powers at each port can be derived and expressed below:

$$P_1 = \frac{V_1V_2L_3L_4\phi_{12}(\pi - |\phi_{12}|) + V_1V_3L_2L_4\phi_{13}(\pi - |\phi_{13}|) + V_1V_4L_2L_3\phi_{14}(\pi - |\phi_{14}|)}{2\pi^2 f_{sw}(L_1L_2L_3 + L_1L_2L_4 + L_1L_3L_4 + L_2L_3L_4)} \tag{3.13}$$

$$P_2 = \frac{-V_1V_2L_3L_4\phi_{12}(\pi - |\phi_{12}|) + V_2V_3L_1L_4\phi_{23}(\pi - |\phi_{23}|) + V_2V_4L_1L_3\phi_{24}(\pi - |\phi_{24}|)}{2\pi^2 f_{sw}(L_1L_2L_3 + L_1L_2L_4 + L_1L_3L_4 + L_2L_3L_4)} \tag{3.14}$$

$$P_3 = \frac{-V_1V_3L_2L_4\phi_{13}(\pi - |\phi_{13}|) - V_2V_3L_1L_4\phi_{23}(\pi - |\phi_{23}|) + V_3V_4L_1L_2\phi_{34}(\pi - |\phi_{34}|)}{2\pi^2 f_{sw}(L_1L_2L_3 + L_1L_2L_4 + L_1L_3L_4 + L_2L_3L_4)} \tag{3.15}$$

$$P_4 = \frac{-V_1V_4L_2L_3\phi_{14}(\pi - |\phi_{14}|) - V_2V_4L_1L_3\phi_{24}(\pi - |\phi_{24}|) - V_3V_4L_1L_2\phi_{34}(\pi - |\phi_{34}|)}{2\pi^2 f_{sw}(L_1L_2L_3 + L_1L_2L_4 + L_1L_3L_4 + L_2L_3L_4)} \tag{3.16}$$

where $P_1 = P_{12}+P_{13}+P_{14}$, $P_2 = -P_{12}+P_{23}+P_{24}$, $P_3 = -P_{13}-P_{23}+P_{34}$, $P_4 = -P_{14}-P_{24}-P_{34}$.

The complex network of inductors results in a highly coupled nature of the ports in the QAB converter. The power condition at one port if varied, affects all other ports due to the port coupling. A power decoupling controller is proposed for power flow decoupling in the QAB converter. The proposed power flow decoupling method is an expanded form of the decoupling method proposed in Section 2. Even though it is an extension of the method used for the TAB converter, the extended port number, and the complicated coupled power flow network make it more challenging to design.

3.3 Proposed Decoupling control Method

In this section, the proposed decoupling controller in section 2 for TAB converters is expanded and proposed for power flow decoupling in the QAB converter. The design procedure for implementing the proposed controller in the QAB converter is similar to the procedure for the TAB decoupling method except that there are more parameters involved which makes it more complicated. A linearized model of the QAB converter is derived using the same linearization approach in section 2. Just as in the TAB converter, the ports in the QAB converter can be represented as current sources, and the output powers

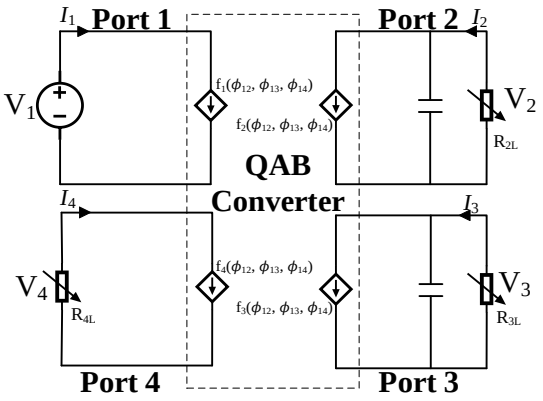

Fig. 3.5 Average model of the QAB converter.

can be represented as the average current over one switching cycle. The average model of the QAB converter is derived and shown in Fig. 3.5 according to the QAB converter topology in Fig. 3.1. The output current equations can be derived from the active power equations of the controlled ports as follows:

$$I_2 = \frac{V_1(|\phi_{12}|-\pi)(\phi_{12})}{2\pi^2 f_{sw} L_{12}} + \frac{V_3(\phi_{12}-\phi_{13})(|\phi_{12}-\phi_{13}|-\pi)}{2\pi^2 f_{sw} L_{23}} + \frac{V_4(\phi_{12}-\phi_{14})(|\phi_{12}-\phi_{14}|-\pi)}{2\pi^2 f_{sw} L_{24}} \tag{3.17}$$

$$I_3 = \frac{V_1(|\phi_{13}|-\pi)(\phi_{13})}{2\pi^2 f_{sw} L_{13}} + \frac{V_2(|\phi_{13}-\phi_{12}|-\pi)(\phi_{13}-\phi_{12})}{2\pi^2 f_{sw} L_{23}} + \frac{V_4(|\phi_{13}-\phi_{14}|-\pi)(\phi_{13}-\phi_{14})}{2\pi^2 f_{sw} L_{34}} \tag{3.18}$$

$$I_4 = \frac{V_1(|\phi_{14}|-\pi)(\phi_{14})}{2\pi^2 f_{sw} L_{14}} + \frac{V_2(\phi_{14}-\phi_{12})(|\phi_{14}-\phi_{12}|-\pi)}{2\pi^2 f_{sw} L_{24}} + \frac{V_3(\phi_{14}-\phi_{13})(|\phi_{14}-\phi_{13}|-\pi)}{2\pi^2 f_{sw} L_{34}} \tag{3.19}$$

The quadratic terms in the output current equations are eliminated using the sinusoidal approximation in (2.1.19) and the resulting simplified equations are expressed below:

$$I_2 = \frac{V_1 \sin(\phi_{12})}{\frac{1}{4}\pi^3 f_{sw} L_{12}} + \frac{V_3 \sin(\phi_{12}-\phi_{13})}{\frac{1}{4}\pi^3 f_{sw} L_{23}} + \frac{V_4 \sin(\phi_{12}-\phi_{14})}{\frac{1}{4}\pi^3 f_{sw} L_{24}} \tag{3.21}$$

$$I_3 = \frac{V_1 \sin(\phi_{13})}{\frac{1}{4}\pi^3 f_{sw} L_{13}} + \frac{V_2 \sin(\phi_{13}-\phi_{12})}{\frac{1}{4}\pi^3 f_{sw} L_{23}} + \frac{V_4 \sin(\phi_{13}-\phi_{14})}{\frac{1}{4}\pi^3 f_{sw} L_{34}} \tag{3.22}$$

$$I_4 = \frac{V_1 \sin(\phi_{14})}{\frac{1}{4}\pi^3 f_{sw} L_{14}} + \frac{V_2 \sin(\phi_{14}-\phi_{12})}{\frac{1}{4}\pi^3 f_{sw} L_{24}} + \frac{V_3 \sin(\phi_{14}-\phi_{13})}{\frac{1}{4}\pi^3 f_{sw} L_{34}} \tag{3.23}$$

To derive a linearized model of the QAB converter, the output ports are represented as sums of their steady-state and small-signal variations. I_2 is represented accordingly as shown in (3.24) and the Taylor series of I_2 about the operating point (^) result in the expressions of $I_{2^\wedge}$ and ΔI_2 as shown in (3.25) and (3.26), respectively.

$$I_2 = I_{2^\wedge} + \Delta I_2 \tag{3.24}$$

$$I_{2^\wedge} = \left[\frac{V_1 \sin(\phi_{12^\wedge})}{\frac{1}{4}\pi^3 f_{sw} L_{12}} + \frac{V_3 \sin(\phi_{12^\wedge}-\phi_{13^\wedge})}{\frac{1}{4}\pi^3 f_{sw} L_{23}} + \frac{V_4 \sin(\phi_{12^\wedge}-\phi_{14^\wedge})}{\frac{1}{4}\pi^3 f_{sw} L_{24}} \right] \tag{3.25}$$

$$\Delta I_2 = \left[\frac{V_1 \cos(\phi_{12^\wedge})\Delta\phi_{12}}{\frac{1}{4}\pi^3 f_{sw} L_{12}} + \frac{V_3 \cos(\phi_{12^\wedge}-\phi_{13^\wedge})\Delta\phi_{12}}{\frac{1}{4}\pi^3 f_{sw} L_{23}} + \frac{V_4 \cos(\phi_{12^\wedge}-\phi_{14^\wedge})\Delta\phi_{12}}{\frac{1}{4}\pi^3 f_{sw} L_{24}} - \frac{V_3 \cos(\phi_{12^\wedge}-\phi_{13^\wedge})\Delta\phi_{13}}{\frac{1}{4}\pi^3 f_{sw} L_{23}} - \frac{V_3 \cos(\phi_{12^\wedge}-\phi_{14^\wedge})\Delta\phi_{14}}{\frac{1}{4}\pi^3 f_{sw} L_{24}} \right] \tag{3.26}$$

By the same procedure, (3.27) and (3.30) are established and the Taylor series of I_3 and I_4 results in the

expressions of $I_{3\wedge}$ and ΔI_3 as shown in (3.28) and (3.29), and the expressions of $I_{4\wedge}$ and ΔI_4 as shown in (3.28) and (3.29) respectively.

$$I_3 = I_{3\wedge} + \Delta I_3 \tag{3.27}$$

$$I_{3\wedge} = \left[\frac{V_1 \sin(\phi_{13\wedge})}{\frac{1}{4}\pi^3 f_{sw} L_{13}} + \frac{V_2 \sin(\phi_{13\wedge} - \phi_{12\wedge})}{\frac{1}{4}\pi^3 f_{sw} L_{23}} + \frac{V_4 \sin(\phi_{13\wedge} - \phi_{14\wedge})}{\frac{1}{4}\pi^3 f_{sw} L_{34}} \right] \tag{3.28}$$

$$\Delta I_3 = \left[-\frac{V_2 \cos(\phi_{13\wedge} - \phi_{12\wedge})\Delta\phi_{12}}{\frac{1}{4}\pi^3 f_{sw} L_{23}} + \frac{V_1 \cos(\phi_{13\wedge})\Delta\phi_{13}}{\frac{1}{4}\pi^3 f_{sw} L_{12}} + \frac{V_2 \cos(\phi_{13\wedge} - \phi_{12\wedge})\Delta\phi_{13}}{\frac{1}{4}\pi^3 f_{sw} L_{23}} + \frac{V_4 \cos(\phi_{13\wedge} - \phi_{14\wedge})\Delta\phi_{13}}{\frac{1}{4}\pi^3 f_{sw} L_{34}} - \frac{V_4 \cos(\phi_{13\wedge} - \phi_{14\wedge})\Delta\phi_{14}}{\frac{1}{4}\pi^3 f_{sw} L_{24}} \right] \tag{3.29}$$

$$I_4 = I_{4\wedge} + \Delta I_4 \tag{3.30}$$

$$I_{4\wedge} = \left[\frac{V_1 \sin(\phi_{14\wedge})}{\frac{1}{4}\pi^3 f_{sw} L_{14}} + \frac{V_2 \sin(\phi_{13\wedge} - \phi_{12\wedge})}{\frac{1}{4}\pi^3 f_{sw} L_{23}} + \frac{V_3 \sin(\phi_{14\wedge} - \phi_{13\wedge})}{\frac{1}{4}\pi^3 f_{sw} L_{34}} \right] \tag{3.31}$$

$$\Delta I_4 = \left[-\frac{V_2 \cos(\phi_{14\wedge} - \phi_{12\wedge})\Delta\phi_{12}}{\frac{1}{4}\pi^3 f_{sw} L_{24}} - \frac{V_3 \cos(\phi_{14\wedge} - \phi_{13\wedge})\Delta\phi_{13}}{\frac{1}{4}\pi^3 f_{sw} L_{34}} + \frac{V_1 \cos(\phi_{14\wedge})\Delta\phi_{14}}{\frac{1}{4}\pi^3 f_{sw} L_{12}} + \frac{V_2 \cos(\phi_{14\wedge} - \phi_{12\wedge})\Delta\phi_{14}}{\frac{1}{4}\pi^3 f_{sw} L_{23}} + \frac{V_3 \cos(\phi_{14\wedge} - \phi_{13\wedge})\Delta\phi_{14}}{\frac{1}{4}\pi^3 f_{sw} L_{34}} \right] \tag{3.32}$$

From (3.330, (3.34), and (3.35), the linearized model of the QAB converter can be established with the small-signal variations expressed in terms of the gain matrix elements and the corresponding phase shift variables.

$$I_2 = I_{2\wedge} + H'_{11}\Delta\phi_{12} + H'_{12}\Delta\phi_{13} + H'_{13}\Delta\phi_{14} \tag{3.33}$$

$$I_3 = I_{3\wedge} + H'_{21}\Delta\phi_{12} + H'_{22}\Delta\phi_{13} + H'_{23}\Delta\phi_{14} \tag{3.34}$$

$$I_4 = I_{4\wedge} + H'_{31}\Delta\phi_{12} + H'_{32}\Delta\phi_{13} + H'_{33}\Delta\phi_{14} \tag{3.35}$$

Where,

$$H'_{11} = \frac{V_1 L_3 L_4 \cos(\phi_{12\wedge}) + V_3 L_1 L_4 \cos(\phi_{12\wedge} - \phi_{13\wedge}) + V_4 L_1 L_3 \cos(\phi_{12\wedge} - \phi_{14\wedge})}{\frac{1}{4}\pi^3 f_{sw}(L_1 L_2 L_3 + L_1 L_2 L_4 + L_1 L_3 L_4 + L_2 L_3 L_4)} \tag{3.36}$$

$$H'_{12} = \frac{-V_3 L_1 L_4 \cos(\phi_{12\wedge} - \phi_{13\wedge})}{\frac{1}{4}\pi^3 f_{sw}(L_1 L_2 L_3 + L_1 L_2 L_4 + L_1 L_3 L_4 + L_2 L_3 L_4)} \tag{3.37}$$

$$H'_{13} = \frac{-V_4 L_1 L_3 \cos(\phi_{12^\wedge} - \phi_{14^\wedge})}{\frac{1}{4}\pi^3 f_{sw}(L_1L_2L_3 + L_1L_2L_4 + L_1L_3L_4 + L_2L_3L_4)} \tag{3.38}$$

$$H'_{21} = \frac{-V_2 L_1 L_4 \cos(\phi_{13^\wedge} - \phi_{12^\wedge})}{\frac{1}{4}\pi^3 f_{sw}(L_1L_2L_3 + L_1L_2L_4 + L_1L_3L_4 + L_2L_3L_4)} \tag{3.39}$$

$$H'_{22} = \frac{V_1 L_2 L_4 \cos(\phi_{13^\wedge}) + V_2 L_1 L_4 \cos(\phi_{13^\wedge} - \phi_{12^\wedge}) + V_4 L_1 L_2 \cos(\phi_{13^\wedge} - \phi_{14^\wedge})}{\frac{1}{4}\pi^3 f_{sw}(L_1L_2L_3 + L_1L_2L_4 + L_1L_3L_4 + L_2L_3L_4)} \tag{3.40}$$

$$H'_{23} = \frac{-V_4 L_1 L_2 \cos(\phi_{13^\wedge} - \phi_{14^\wedge})}{\frac{1}{4}\pi^3 f_{sw}(L_1L_2L_3 + L_1L_2L_4 + L_1L_3L_4 + L_2L_3L_4)} \tag{3.41}$$

$$H'_{31} = \frac{-V_2 L_1 L_3 \cos(\phi_{14^\wedge} - \phi_{12^\wedge})}{\frac{1}{4}\pi^3 f_{sw}(L_1L_2L_3 + L_1L_2L_4 + L_1L_3L_4 + L_2L_3L_4)} \tag{3.42}$$

$$H'_{32} = \frac{-V_3 L_1 L_2 \cos(\phi_{14^\wedge} - \phi_{13^\wedge})}{\frac{1}{4}\pi^3 f_{sw}(L_1L_2L_3 + L_1L_2L_4 + L_1L_3L_4 + L_2L_3L_4)} \tag{3.43}$$

$$H'_{33} = \frac{V_1 L_2 L_3 \cos(\phi_{14^\wedge}) + V_2 L_1 L_3 \cos(\phi_{14^\wedge} - \phi_{12^\wedge}) + V_3 L_1 L_2 \cos(\phi_{14^\wedge} - \phi_{13^\wedge})}{\frac{1}{4}\pi^3 f_{sw}(L_1L_2L_3 + L_1L_2L_4 + L_1L_3L_4 + L_2L_3L_4)} \tag{3.44}$$

$$\begin{bmatrix} \Delta I_2 \\ \Delta I_3 \\ \Delta I_4 \end{bmatrix} = \begin{bmatrix} H'_{11} & H'_{12} & H'_{13} \\ H'_{21} & H'_{22} & H'_{23} \\ H'_{31} & H'_{32} & H'_{33} \end{bmatrix} = \begin{bmatrix} \phi_{12} \\ \phi_{13} \\ \phi_{14} \end{bmatrix} \tag{3.45}$$

The control-to-output transfer matrix of the linearized model of the QAB converter can be established as shown in (3.45) and the QAB converter according to the linearized model is shown in Fig. 3.6. The controller is made up of three PI controllers represented as $H_{PI\_Vo2}(s)$ for port 2, $H_{PI\_Vo3}(s)$ for port 3, and $H_{PI\_Vo4}(s)$ for port 4. The output impedance of port 2 is represented by $Z_2(s)$, $Z_3(s)$ for port 3, and $Z_4(s)$ for port 4. The PI loops are coupled via the transfer functions H'_{12}, H'_{13}, H'_{21}, H'_{23}, H'_{31}, and H'_{32}. To decompose the coupled controllers into SISO controllers, the cross-coupling transfer functions should be eliminated. For all operating points considered, the equations of the sub-transfer functions of (H') can be used to calculate their numerical values corresponding inverse matrices are calculated to represent the decoupling matrices (N'). N' can be calculated using the equation below:

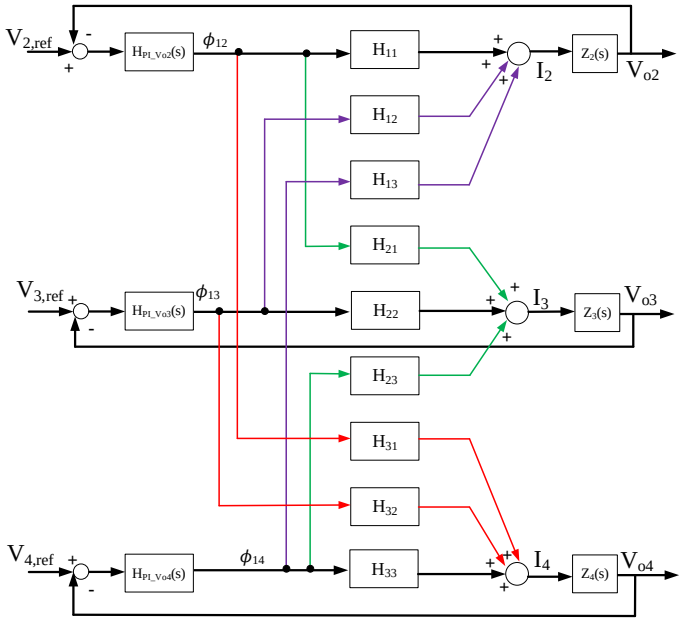

Fig. 3.6 Block diagram of the QAB converter controller.

$$N' = H'^{-1} = \frac{1}{|H'|}\begin{bmatrix} \begin{vmatrix} H'_{22} & H'_{23} \\ H'_{32} & H'_{33} \end{vmatrix} & \begin{vmatrix} H'_{13} & H'_{12} \\ H'_{33} & H'_{32} \end{vmatrix} & \begin{vmatrix} H'_{12} & H'_{13} \\ H'_{22} & H'_{23} \end{vmatrix} \\ \begin{vmatrix} H'_{23} & H'_{21} \\ H'_{33} & H'_{31} \end{vmatrix} & \begin{vmatrix} H'_{11} & H'_{13} \\ H'_{31} & H'_{33} \end{vmatrix} & \begin{vmatrix} H'_{13} & H'_{11} \\ H'_{23} & H'_{21} \end{vmatrix} \\ \begin{vmatrix} H'_{21} & H'_{22} \\ H'_{31} & H'_{32} \end{vmatrix} & \begin{vmatrix} H'_{12} & H'_{11} \\ H'_{32} & H'_{31} \end{vmatrix} & \begin{vmatrix} H'_{11} & H'_{12} \\ H'_{21} & H'_{22} \end{vmatrix} \end{bmatrix} \tag{3.46}$$

The inclusion of N results in new phase displacement variables ϕ_{12*}, ϕ_{13*}, and ϕ_{14*} and the control-to-output transfer matrix equation of the proposed decoupling controller is expressed as follows:

$$\begin{bmatrix} \Delta I_2 \\ \Delta I_3 \\ \Delta I_4 \end{bmatrix} = \begin{bmatrix} N'_{11} & N'_{12} & N'_{13} \\ N'_{21} & N'_{22} & N'_{23} \\ N'_{31} & N'_{32} & N'_{33} \end{bmatrix} \begin{bmatrix} H'_{11} & H'_{12} & H'_{13} \\ H'_{21} & H'_{22} & H'_{23} \\ H'_{31} & H'_{32} & H'_{33} \end{bmatrix} \begin{bmatrix} \Delta\phi_{12*} \\ \Delta\phi_{13*} \\ \Delta\phi_{14*} \end{bmatrix} = \begin{bmatrix} 1 & 0 & 0 \\ 0 & 1 & 0 \\ 0 & 0 & 1 \end{bmatrix} \begin{bmatrix} \Delta\phi_{12*} \\ \Delta\phi_{13*} \\ \Delta\phi_{14*} \end{bmatrix} \tag{3.47}$$

The proposed decoupling controller is shown in Fig. 3.7. It is made up of three PI controllers and a LUT that stores nine sets of decoupling matrices values. (3.47) shows that the system's gain matrix becomes a unit matrix at all operating points with the decoupling controller. The LUT designed in the digital controller is similar to the LUT discussed in section 2 but an expanded form. The structure of the LUT is shown in Fig 3.9. It is made up of 12 individual arrays that store different sets of values. The individual arrays are I_2, I_3, I_4, N_{11}, N_{12}, N_{13}, N_{21}, N_{22}, N_{23}, N_{31}, N_{32}, and N_{33}. I_2, I_3, and I_4 represent the

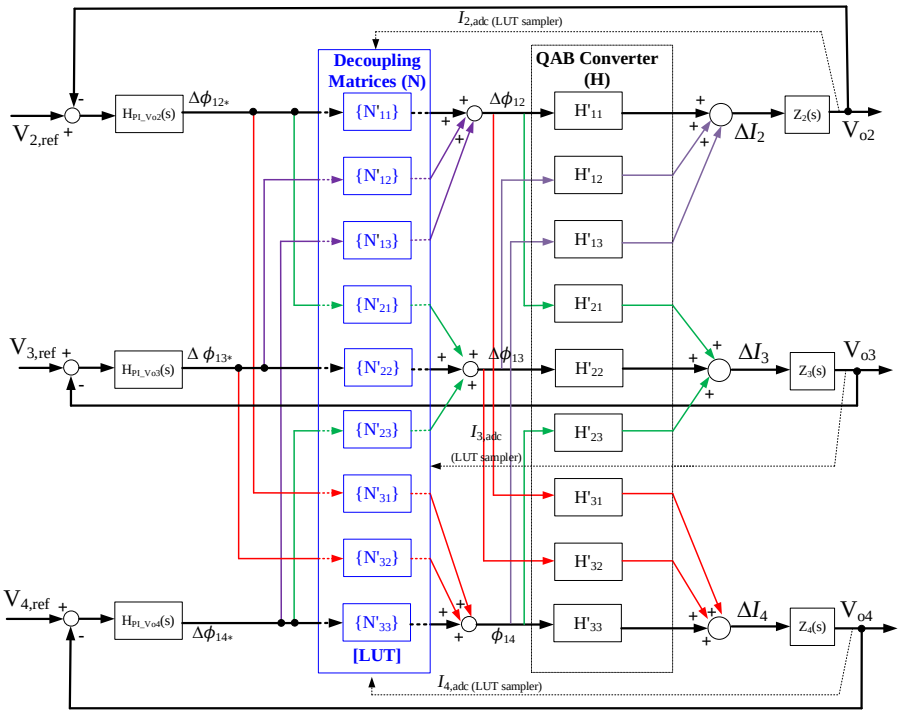

Fig. 3.7 Block diagram of the proposed decoupling controller.

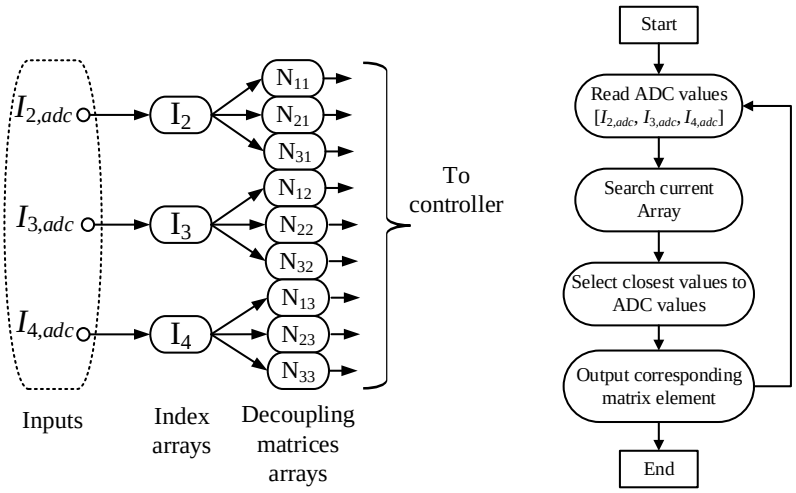

Fig. 3.8 Diagrams for the implemented LUT: (a) Structure of the LUT, (b) Flow chart of the LUT operation

index arrays for sorting decoupling matrices arrays. N_{11}, N_{12}, N_{13}, N_{21}, N_{22}, N_{23}, N_{31}, N_{32}, and N_{33} represent the decoupling matrices arrays. I_2 is linked to N_{11}, N_{21}, N_{31}, I_3 is linked to N_{12}, N_{22}, and N_{32}, and I_4 is linked to N_{13}, N_{23}, and N_{33}. $I_{2,adc}$, $I_{3,adc}$, and $I_{4,adc}$ are the sampled ADC current values at ports 2, 3, and 4, respectively, and they are used as inputs to the C pointer algorithm used. The current index values are derived with the basic power equation as discussed in section 2.1. The inputs are taken and matching pairs in the index arrays are sorted for. Selected matching index array elements return corresponding decoupling matrices values to the controller. To make up for value mismatches and to

ensure that decoupling matrices are returned to the controller at any operating point, the algorithm selects the closest index values to the inputs and returns corresponding decoupling matrices. The flowchart that represents the operation of the implemented LUT is shown in Fig. 3.10.

3.4 Simulation and Simulation Results

A simulation is conducted using PSIM software. A QAB converter model is developed, and the proposed decoupling controller is also implemented in the model as shown in Fig. 3.9. The model is developed based on the parameters shown in table 3.1. The converter model is rated at 2 kW with ports 1, 2, 3, and 4 voltages rated at 200 V and the converter operates at a frequency of 20 kHz. Three test cases are conducted in the simulation model.

In test case 1, power in V_{o2} is stepped up from 100 W to 1 kW and stepped down from 1 kW to 100 W with and without the proposed decoupling algorithm. When power is stepped up in V_{o2} from 100 W to 1 kW, voltage undershoots of 4.96 V and 5.03 V are observed in V_{o3} and V_{o4}, respectively without

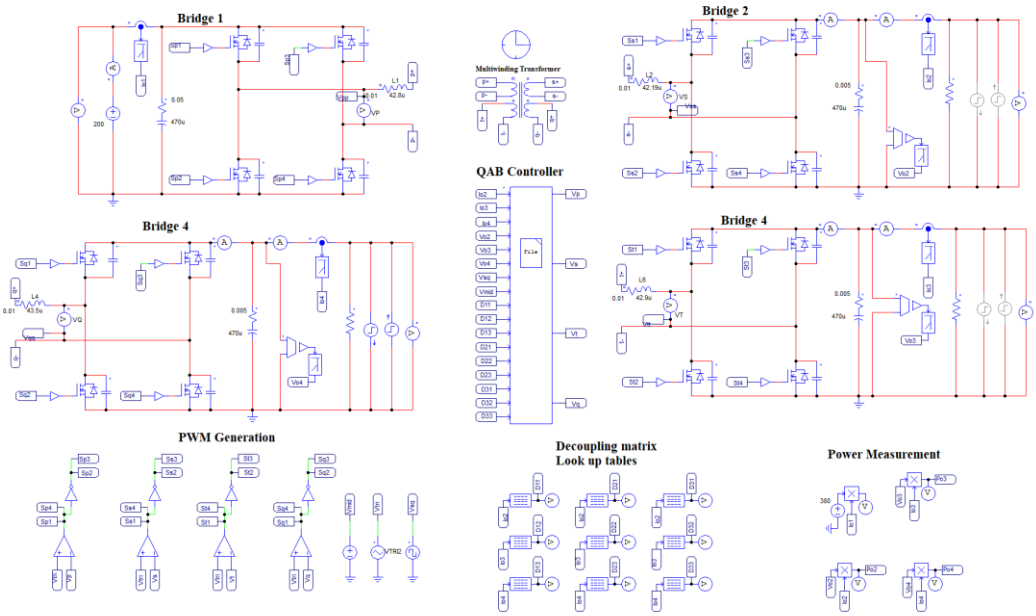

Fig. 3.9 Simulation setup using PSIM software

Table 3.1: Simulation and Experiment parameters

Parameter	Symbol	Value	Unit
Port 1 voltage	V_1	200	V
Port 2 voltage	V_{o2}	200	V
Port 3 voltage	V_{o3}	200	V
Port 4 voltage	V_{o4}	200	V
Turn ratio	n_1: n_2: n_3: n_4	1:1:1:1	
Inductors	L_1, L_2, L_3, L_4	42.8, 42.19, 42.9, 43.5	µH
Switching frequency	f_{sw}	20	kHz

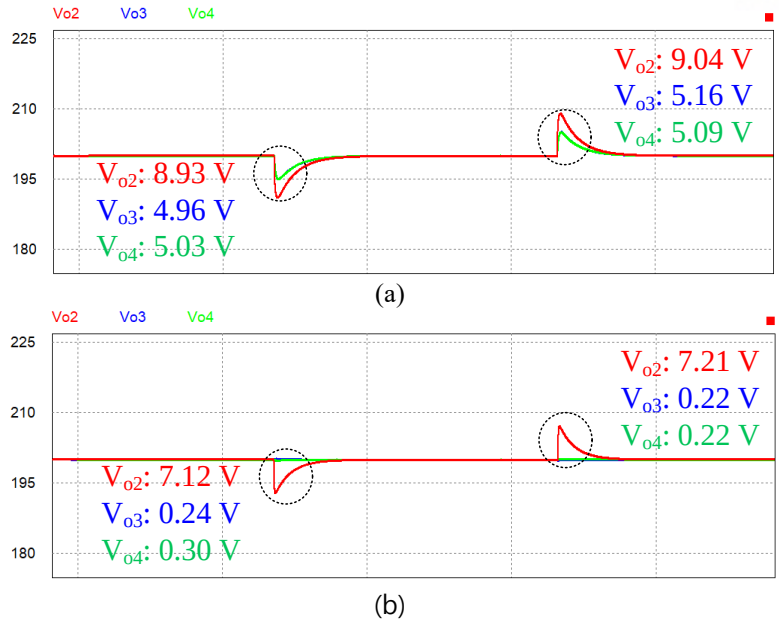

Fig. 3.10 Simulated voltage waveforms for power step in V_{o2}: (a) without decoupling control (b) with the proposed decoupling controller.

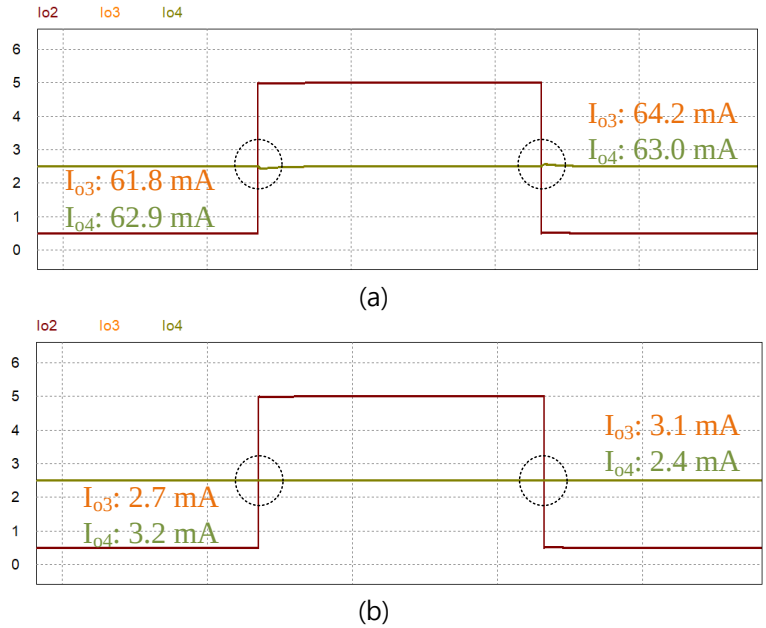

Fig. 3.11 Simulated current waveforms for power step in V_{o2}: (a) without decoupling control (b) with the proposed decoupling controller.

decoupling control. When V_{o2}'s power is stepped down (1 kW - 100 W), voltage overshoots of 5.16 V and 5.09 V are observed in V_{o3} and V_{o4}, respectively without decoupling control. The simulation waveforms for voltage without decoupling control are shown in Fig. 3.10 (a). With the proposed decoupling controller, the initial voltage undershoots observed in V_{o3} and V_{o4} are reduced to 0.24 V and 0.30 V, respectively, when V_{o2}'s power is stepped up (100 W - 1 kW). The results represent 95.16% and 94.04% voltage decoupling performances in V_{o3} and V_{o4}, respectively. For power step down (1 kW –

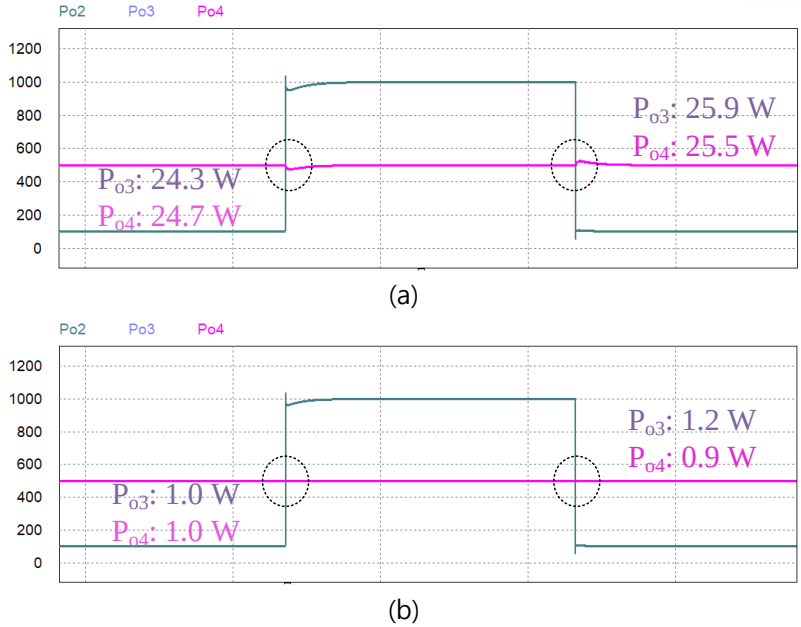

Fig. 3.12 Simulated power waveforms for power step in V_{o2}: (a) without decoupling control (b) with the proposed decoupling controller.

100 W) in V_{o2}, the initial voltage overshoots in V_{o3} and V_{o4} are reduced to 0.22 V and 0.22 V, respectively with the proposed decoupling controller. The results represent 95.74% and 95.68% voltage decoupling performances in V_{o3} and V_{o4}, respectively. The voltage simulation waveforms with the proposed decoupling controller are shown in Fig. 3.10 (b).

In terms of current, current undershoots of 61.8 mA and 62.9 mA are observed in V_{o3} and V_{o4} when power in V_{o2} is stepped up (100 W – 1 kW) without decoupling control. For power step down (1 kW – 100 W) in V_{o2}, current overshoots of 64.2 mA and 63.0 mA are captured in V_{o3} and V_{o4} without decoupling control. The current simulation waveforms without decoupling control are shown in Fig. 3.11 (a). For power step-up (100 W - 1k W) in V_{o2}, the initial current undershoots in V_{o3} and V_{o4} are reduced to 2.7 mA and 3.2 mA, respectively with the proposed decoupling controller. The results represent 95.63% and 94.91% of current decoupling performances in V_{o3} and V_{o4}, respectively. With the proposed decoupling controller, the initial current overshoots observed in V_{o3} and V_{o4} are reduced to 3.1 mA and 2.4 mA, respectively, when V_{o2}'s power is stepped down (1 kW – 100 W). The results represent 95.17% and 96.19% of current decoupling performances in V_{o3} and V_{o4}, respectively. The current simulation waveforms with the proposed decoupling controller are shown in Fig. 3.11 (b).

In terms of power simulation, power undershoots of 24.3 W and 24.7 W are observed in V_{o3} and V_{o4} when power in V_{o2} is stepped up from 100 W to 1 kW without decoupling control. For power step down (1 kW – 100 W) in Vo2, power overshoots of 25.9 W and 25.5 W are seen in Vo3 and Vo4 without decoupling control. The power simulation waveforms without decoupling control are shown in Fig. 3.12 (a). The initial power undershoots in Vo3 and Vo4 for power step-up (100 W - 1k W) in Vo2, are reduced to 1.0 W and 1.0 W, respectively with the proposed decoupling controller. The results represent

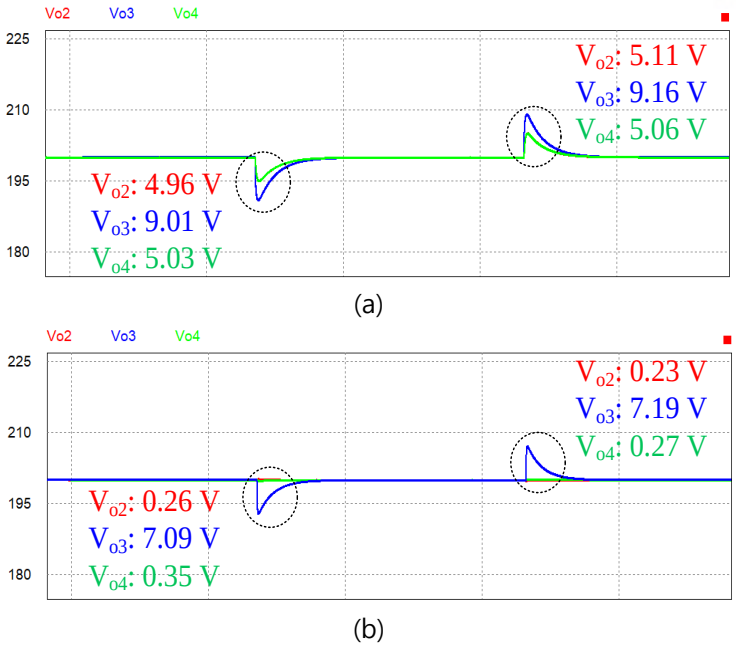

Fig. 3.13 Simulated voltage waveforms for power step in V_{o3}: (a) without decoupling control (b) with the proposed decoupling controller.

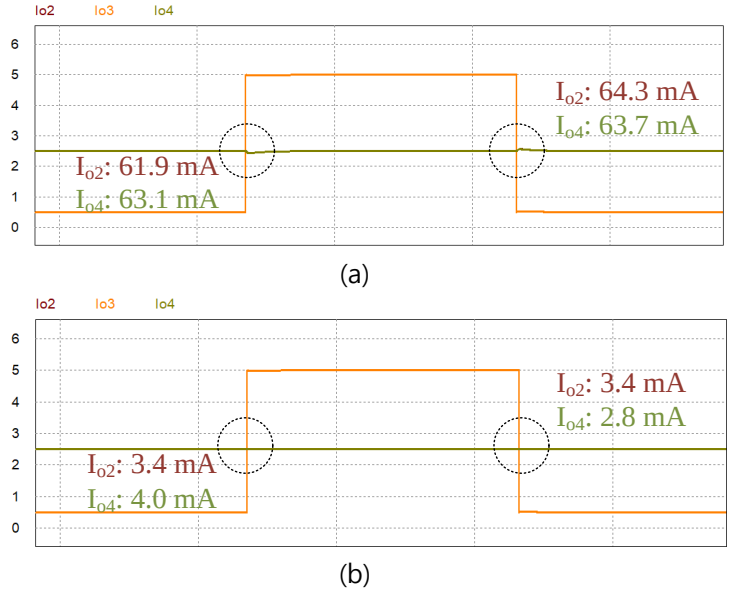

Fig. 3.14 Simulated current waveforms for power step in V_{o3}: (a) without decoupling control (b) with the proposed decoupling controller.

95.88% and 95.95% power decoupling performances in Vo3 and Vo4, respectively. With the proposed decoupling controller, the initial power overshoots observed in Vo3 and Vo4 are reduced to 1.2 W and 0.9 W, respectively, when Vo2's power is stepped down (1 kW – 100 W). The results represent 95.37% and 96.47% power decoupling performances in V_{o3} and V_{o4}, respectively. The power simulation waveforms with the proposed decoupling controller are shown in Fig. 3.12 (b).

In test case 2, power in V_{o3} is stepped up from 100 W to 1 kW and stepped down from 1 kW to 100 W with and without the proposed decoupling algorithm. When the power in V_{o3} is stepped up (100 W -

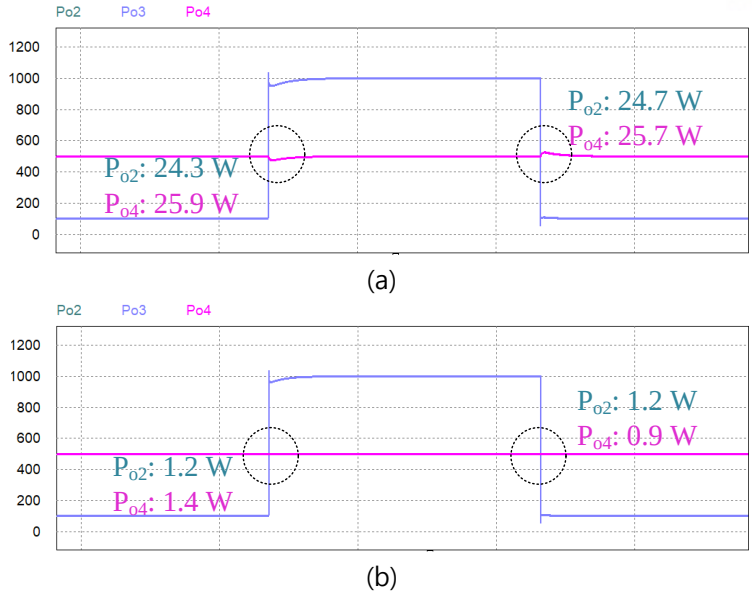

Fig. 3.15 Simulated power waveforms for power step in V_{o3}: (a) without decoupling control (b) with the proposed decoupling controller.

1k W), voltage undershoots of 4.96 V and 5.03 V are captured in V_{o2} and V_{o4}, respectively without decoupling control. When V_{o3}'s power is stepped down from 1 kW to 100 W, voltage overshoots of 56.11 V and 5.06 V are captured in V_{o2} and V_{o4}, respectively without decoupling control. The simulation waveforms for voltage without decoupling control are shown in Fig. 3.13 (a). With the proposed decoupling controller, the initial voltage undershoots observed in V_{o2} and V_{o4} are reduced to 0.26 V and 0.35 V, respectively, when V_{o3}'s power is stepped up from 100 W to 1 kW. The results represent 94.76% and 93.04% voltage decoupling performances in V_{o2} and V_{o4}, respectively. For power step down from 1 kW to 100 W in V_{o3}, the initial voltage overshoots in V_{o2} and V_{o4} are reduced to 0.23 V and 0.27 V, respectively with the proposed decoupling controller. The results represent 95.05% and 94.66% voltage decoupling performances in V_{o2} and V_{o4}, respectively. The voltage simulation waveforms with the proposed decoupling controller are shown in Fig. 3.13 (b).

For the current simulation, current undershoots of 61.9 mA and 63.1 mA are observed in V_{o2} and V_{o4} when power in V_{o3} is stepped up from 100 W to 1 kW without decoupling control. When V_{o3}'s power is stepped down from 1 kW to 100 W, current overshoots of 64.3 mA and 63.7 mA are captured in V_{o2} and V_{o4} without decoupling control. The current simulation waveforms without decoupling control are shown in Fig. 3.14 (a). For power step-up (100 W - 1k W) in V_{o2}, the initial current undershoots in V_{o3} and V_{o4} are reduced to 3.4 mA and 4.0 mA, respectively with the proposed decoupling controller. The results represent 94.51% and 93.66% of current decoupling performances in V_{o2} and V_{o4}, respectively. When V_{o2}'s power is stepped down (1 kW – 100 W) with the proposed decoupling controller, the initial current overshoots observed in V_{o2} and V_{o4} are reduced to 3.4 mA and 2.8 mA, respectively. The results represent 94.71% and 95.60% of current decoupling performances in V_{o3} and V_{o4}, respectively. The current simulation waveforms with the proposed decoupling controller are shown in Fig. 3.14 (b).

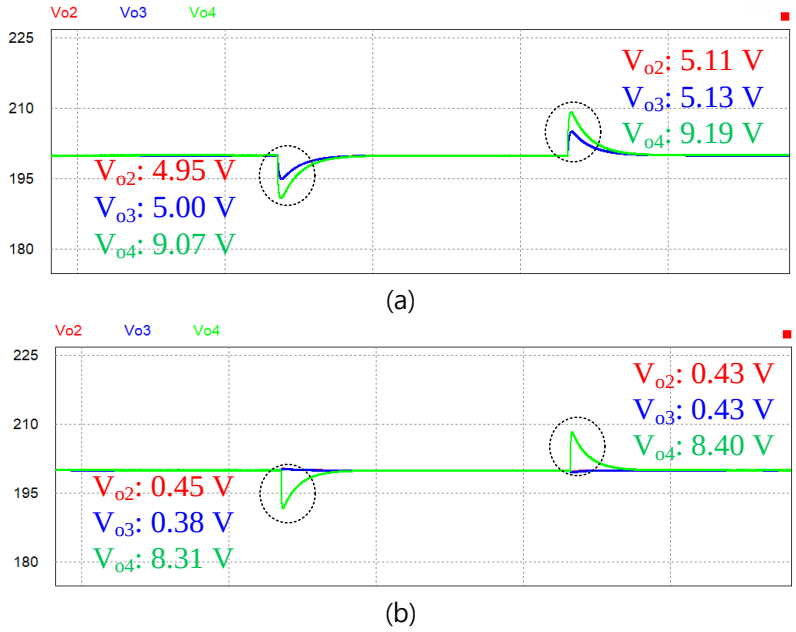

Fig. 3.16 Simulated voltage waveforms for power step in V_{o4}: (a) without decoupling control (b) with the proposed decoupling controller.

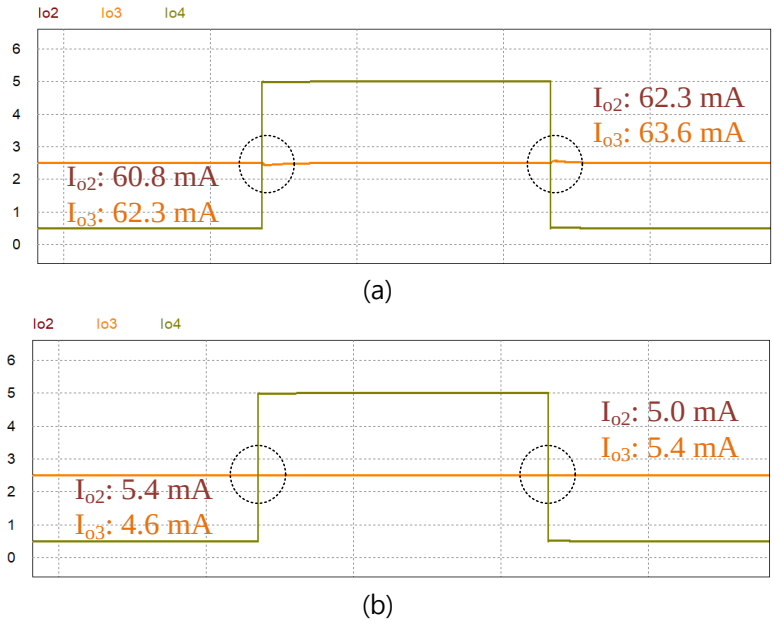

Fig. 3.17 Simulated current waveforms for power step in V_{o4}: (a) without decoupling control (b) with the proposed decoupling controller.

In terms of power simulation, power undershoots of 24.3 W and 25.9 W are observed in V_{o2} and V_{o4} when power in V_{o3} is stepped up from100 W to 1 kW without decoupling control. For power step down (1 kW – 100 W) in V_{o3}, power overshoots of 24.7 W and 25.7 W are seen in V_{o3} and V_{o4} without decoupling control. The power simulation waveforms without decoupling control are shown in Fig. 3.15 (a). The initial power undershoots in V_{o2} and V_{o4} for power step-up (100 W - 1k W) in V_{o3}, are reduced to 1.2 W and 1.4 W, respectively with the proposed decoupling controller. The results represent

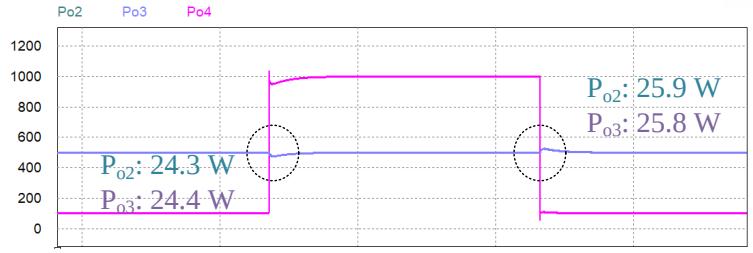

(a)

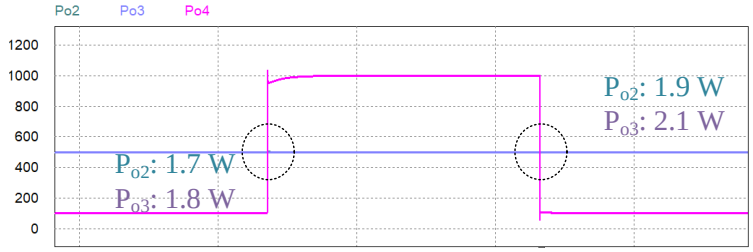

(b)

Fig. 3.18 Simulated power waveforms for power step in V_{o4}: (a) without decoupling control (b) with the proposed decoupling controller.

95.06% and 94.59% power decoupling performances in V_{o3} and V_{o4}, respectively. With the proposed decoupling controller, the initial power overshoots observed in V_{o2} and V_{o4} are reduced to 1.2 W and 0.9 W, respectively, when V_{o3}'s power is stepped down from1 kW to 100 W. The results represent 95.14% and 96.50% power decoupling performances in V_{o2} and V_{o4}, respectively. The power simulation waveforms with the proposed decoupling controller are shown in Fig. 3.15 (b).

In test case 3, power in V_{o4} is stepped up from 100 W to 1 kW and stepped down from 1 kW to 100 W with and without the proposed decoupling algorithm. When V_{o4}'s power is stepped up from 100 W to 1k W, voltage undershoots of 4.95 V and 5.11 V are observed in V_{o2} and V_{o3}, respectively without decoupling control. When V_{o4}'s power is stepped down (1 kW - 100 W), voltage overshoots of 5.00 V and 5.13 V are observed in V_{o2} and V_{o3}, respectively without decoupling control. The simulation waveforms for voltage without decoupling control are shown in Fig. 3.16 (a). With the proposed decoupling controller, the initial voltage undershoots observed in V_{o2} and V_{o3} are reduced to 0.46 V and 0.39 V, respectively, when V_{o4}'s power is stepped up from 100 W to 1 kW. The results represent 90.71% and 92.37% voltage decoupling performances in V_{o2} and V_{o4}, respectively. For power step down (1 kW – 100 W) in V_{o2}, the initial voltage overshoots in V_{o3} and V_{o3} are reduced to 0.40 V and 0.43 V, respectively with the proposed decoupling controller. The results represent 92.00% and 91.62% voltage decoupling performances in V_{o2} and V_{o3}, respectively. The voltage simulation waveforms with the proposed decoupling controller are shown in Fig. 3.16 (b).

For the current simulation, current undershoots of 60.8 mA and 62.3 mA are observed in V_{o2} and V_{o3} when power in V_{o4} is stepped up (100 W – 1 kW) without decoupling control. For power step down from 1 kW to 100 W in V_{o4}, current overshoots of 62.30 mA and 63.60 mA are captured in V_{o2} and V_{o3}

without decoupling control. The current simulation waveforms without decoupling control are shown in Fig. 3.17 (a). For power step up from 100 W to 1k W in V_{o4}, the initial current undershoots in V_{o2} and V_{o3} are reduced to 5.4 mA and 4.6 mA, respectively with the proposed decoupling controller. The results represent 91.12% and 92.62% of current decoupling performances in V_{o2} and V_{o3}, respectively. With the proposed decoupling controller, the initial current overshoots observed in V_{o2} and V_{o3} are reduced to 5.0 mA and 5.4 mA, respectively, when V_{o2}'s power is stepped down (1 kW – 100 W). The results represent 91.97% and 91.51% of current decoupling performances in V_{o2} and V_{o3}, respectively. The current simulation waveforms with the proposed decoupling controller are shown in Fig. 3.17 (b).

For power simulation, power undershoots of 24.3 W and 24.4 W are observed in V_{o2} and V_{o3} when power in V_{o4} is stepped up from 100 W to 1 kW without decoupling control. For power step down (1 kW – 100 W) in V_{o4}, power overshoots of 25.9 W and 25.8 W are observed in V_{o2} and V_{o3} without decoupling control. The power simulation waveforms without decoupling control are shown in Fig. 3.18 (a). The initial power undershoots in V_{o2} and V_{o3} for power step-up (100 W - 1k W) in V_{o4}, are reduced to 1.7 W and 1.8 W, respectively with the proposed decoupling controller. The results represent 93.00% and 92.62% power decoupling performances in V_{o2} and V_{o3}, respectively. With the proposed decoupling controller, the initial power overshoots observed in V_{o2} and V_{o3} are reduced to 1.9 W and 2.1 W, respectively, when V_{o4}'s power is stepped down from 1 kW to 100 W. The results represent 92.66% and 91.86% power decoupling performances in V_{o2} and V_{o3}, respectively. The power simulation waveforms with the proposed decoupling controller are shown in Fig. 3.18 (b). Summaries of all simulation results according to voltage, current, and power are provided in tables 3.2, 3.3, 3.4, 3.5, 3.6, 3.7, 3.8, 3.9, and 3.10.

Table 3.2: Voltage simulation results for step changes in V_{o2}

Step in V_{o2}	Alternate port	Without decoupling	With decoupling	Decoupling performance
100 W – 1 kW	V_{o3}	4.96 V	0.24 V	95.16 %
	V_{o4}	5.16 V	0.30 V	94.04 %
1 kW – 100 W	V_{o3}	5.03 V	0.22 V	95.74 %
	V_{o4}	5.09 V	0.22 V	95.68 %

Table 3.3: Voltage simulation results for step changes in V_{o3}

Step in V_{o3}	Alternate port	Without decoupling	With decoupling	Decoupling performance
100 W – 1 kW	V_{o2}	4.96 V	0.26 V	94.76 %
	V_{o4}	5.03 V	0.35 V	93.04 %
1 kW – 100 W	V_{o2}	5.11 V	0.23 V	95.50 %
	V_{o4}	5.06 V	0.27 V	94.66 %

Table 3.4: Voltage simulation results for changes step in V_{o4}

Step in V_{o4}	Alternate port	Without decoupling	With decoupling	Decoupling performance
100 W – 1 kW	V_{o2}	4.95 V	0.46 V	90.71 %
	V_{o3}	5.11 V	0.39 V	92.37 %
1 kW – 100 W	V_{o2}	5.00 V	0.40 V	92.00 %
	V_{o3}	5.13 V	0.43 V	91.62 %

Table 3.5: Current simulation results for step changes in V_{o2}

Step in V_{o2}	Alternate port	Without decoupling	With decoupling	Decoupling performance
100 W – 1 kW	I_{o3}	61.8 mA	2.7 mA	95.63 %
	I_{o4}	62.9 mA	3.2 mA	94.91 %
1 kW – 100 W	I_{o3}	64.2 mA	3.1 mA	95.17 %
	I_{o4}	63.0 mA	2.4 mA	96.19 %

Table 3.6: Current simulation results for step changes in V_{o3}

Step in V_{o3}	Alternate port	Without decoupling	With decoupling	Decoupling performance
100 W – 1 kW	I_{o2}	61.9 mA	3.4 mA	94.51 %
	I_{o4}	63.1 mA	4.0 mA	93.66 %
1 kW – 100 W	I_{o2}	64.3 mA	3.4 mA	94.71 %
	I_{o4}	63.7 mA	2.8 mA	95.60 %

Table 3.7: Current simulation results for step in changes V_{o4}

Step in V_{o4}	Alternate port	Without decoupling	With decoupling	Decoupling performance
100 W – 1 kW	I_{o2}	60.8 mA	5.4 mA	91.12 %
	I_{o3}	62.3 mA	4.6 mA	92.62 %
1 kW – 100 W	I_{o2}	64.6 mA	5.0 mA	91.97 %
	I_{o3}	63.6 mA	5.4 mA	91.51 %

Table 3.8: Power simulation results for step changes in V_{o2}

Step in V_{o2}	Alternate port	Without decoupling	With decoupling	Decoupling performance
100 W – 1 kW	P_{o3}	24.3 W	1.0 W	95.88 %
	P_{o4}	25.9 W	1.0 W	96.14 %
1 kW – 100 W	P_{o3}	24.7 W	1.2 W	95.14 %
	P_{o4}	25.5 W	0.9 W	96.47 %

Table 3.9: Power simulation results for step changes in V_{o3}

Step in V_{o3}	Alternate port	Without decoupling	With decoupling	Decoupling performance
100 W – 1 kW	P_{o2}	24.3 W	1.2 W	95.06 %
	P_{o4}	25.9 W	1.4 W	94.59 %
1 kW – 100 W	P_{o2}	24.7 W	1.2 W	95.14 %
	P_{o4}	25.7 W	0.9 W	96.50 %

Table 3.10: Power simulation results for step changes in V_{o4}

Step in V_{o4}	Power Step	Without decoupling	With decoupling	Decoupling performance
100 W – 1 kW	P_{o2}	24.3 W	1.7 W	93.00%
	P_{o3}	24.4 W	1.8 W	92.62 %
1 kW – 100 W	P_{o2}	25.9 W	1.9 W	92.66 %
	P_{o3}	25.8 W	2.1 W	91.86 %

3.6 Experiment and Experimental results

To verify the proposed decoupling controller in QAB converters, a 2 kW QAB converter prototype is developed. The QAB prototype is shown in Fig. 3.19. The parameters for the experiment are provided in Table 3.1. The converter is set to operate at a switching frequency of 20 kHz. The voltage ratings at all ports are set as 200 V and each port has a current and voltage sensor. In this experiment, six test cases are conducted. For the experiment conducted, power in a selected load is varied from 100 W to 868 W and then back to 100 W with and without the proposed decoupling controller. The experimental results are captured as waveforms using a high-precision oscilloscope.

In test case 1, the power in Vo2 is stepped from 100 W to 868 W with and without the proposed decoupling controller. Voltage and current waveforms are captured for both conditions. From the results shown in Fig. 3.20 (a), voltage undershoots of 14 V and 13.5 V are observed, and the corresponding current undershoots of 174 mA and 192 mA are observed in Vo3 and Vo4, respectively without decoupling control. With the prosed decoupling controller, the initial voltage undershoots are reduced to 1.5 V and 1.4 V, respectively. The corresponding current undershoots are also reduced to 22 mA and 16 mA respectively. The experimental results for test case 1 with the proposed decoupling controller are shown in Fig. 3.20 (b).

In test case 2, the power in Vo2 is stepped from 868 W to 100 W with and without the proposed decoupling controller. From the results shown in Fig. 3.21 (a), voltage overshoots of 16.5 V are observed,

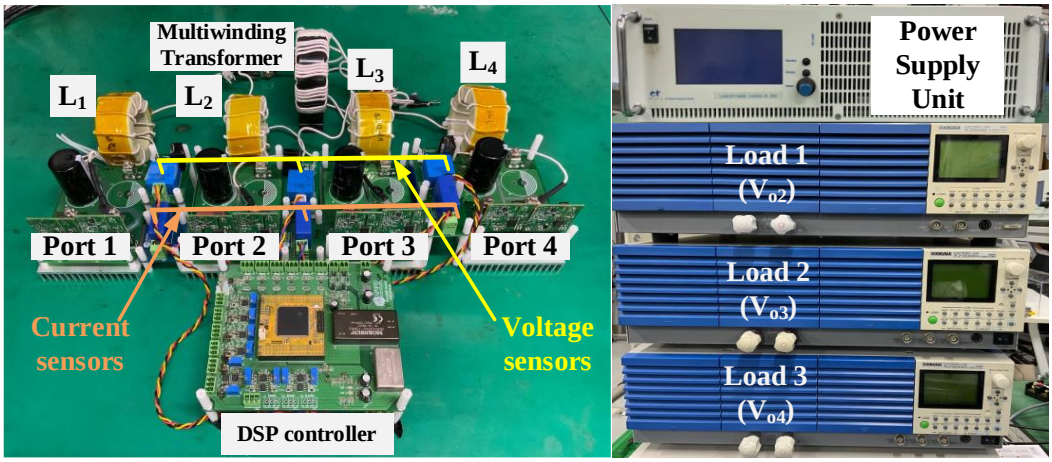

Fig. 3.19 Experiment setup: 2 kW QAB converter prototype, power supply unit, DC loads.

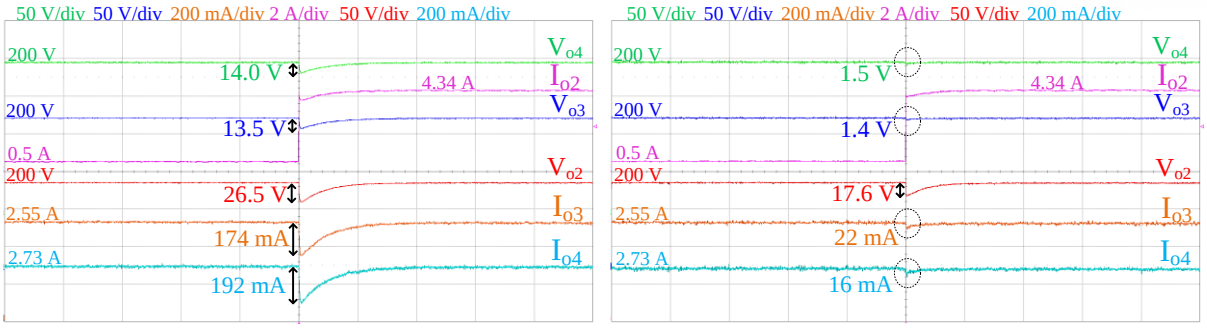

Fig. 3.20 Experimental waveforms for step-up in V_{o2}: (a) without decoupling control (b) with proposed decoupling controller.

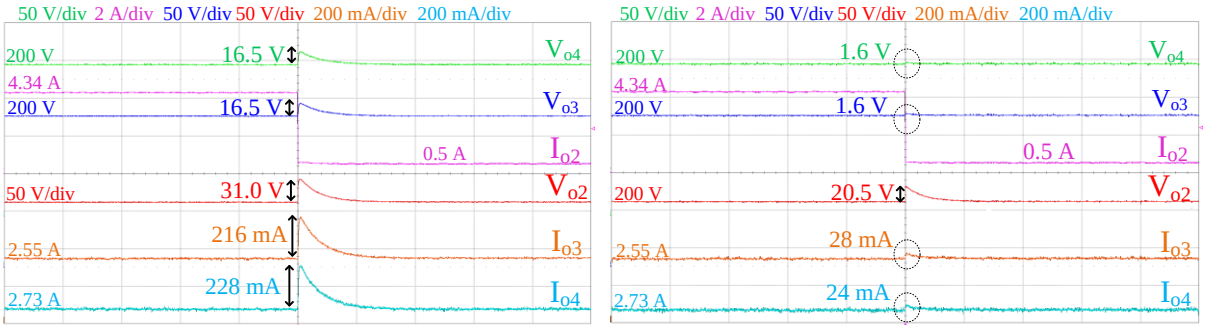

Fig. 3.21 Experimental waveforms for step down in V_{o2}: (a) without decoupling control (b) with proposed decoupling controller.

and corresponding current overshoots of 216 mA and 228 mA are observed in Vo3 and Vo4, respectively without decoupling control. With the prosed decoupling controller, the initial voltage overshoots are reduced to 1.6V. The corresponding current overshoots are also reduced to 28 mA and 24 mA, respectively. The experimental results with the decoupling controller are shown in Fig. 3.21 (b).

In test case 3, the power in V_{o3} is stepped up from 100 W to 868 W From the results shown in Fig. 3.22 (a), voltage undershoots of 13.5 V and 14 V are observed, and corresponding current undershoots of 188 mA and 184 mA are observed in V_{o2} and V_{o4}, respectively without decoupling control. With the prosed decoupling controller, the initial voltage undershoots are reduced to 1.3 V and 0.9 V, respectively. The individual current undershoots are also reduced to 23 mA and 18 mA respectively. The experimental results for this test case condition are shown in Fig. 3.22(b).

In test case 4, the power in V_{o3} is stepped down from 868 W to 100 W with and without the proposed decoupling controller. From the results shown in Fig. 3.23 (a), voltage overshoots of 16.5 V and 16 V are observed, and corresponding current overshoots of 236 mA and 228 mA are observed in V_{o2} and V_{o4}, respectively without decoupling control. With the prosed decoupling controller, the initial voltage overshoots are reduced to 1.9 V and 1.6 V, respectively. The individual current overshoots are reduced to 30 mA and 24 mA, respectively. The experimental results with the decoupling controller are shown

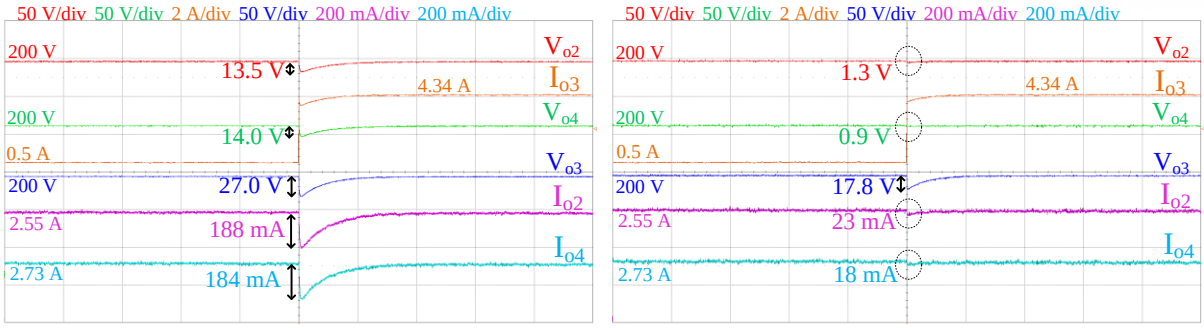

(a) (b)

Fig. 3.22 Experimental waveforms for step-up in V_{o3}: (a) without decoupling control (b) with proposed decoupling controller.

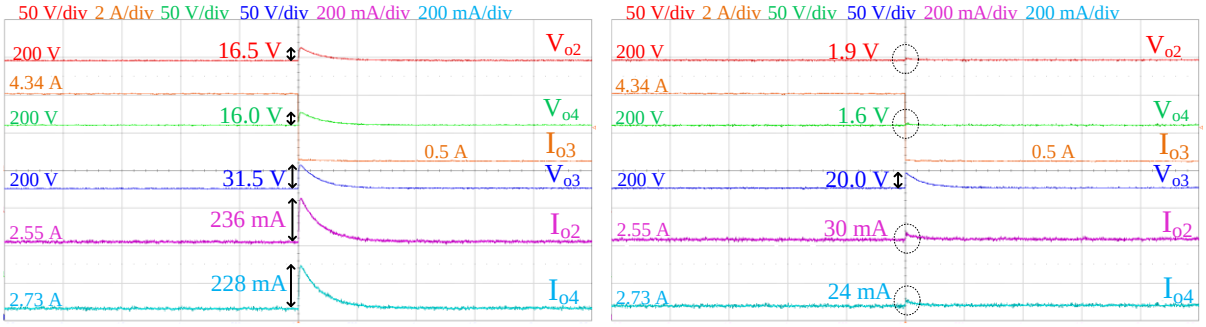

(a) (b)

Fig. 3.23 Experimental waveforms for step-down in V_{o3}: (a) without decoupling control (b) with proposed decoupling controller.

in Fig. 3.23 (b).

In test case 5, the power in V_{o4} is stepped up from 100 W to 868 W with and without the proposed decoupling controller. From the results shown in Fig. 3.24 (a), voltage undershoots of 14 V are observed and corresponding current undershoots of 188 mA and 176 mA are observed in V_{o2} and V_{o3}, respectively without decoupling control. With the prosed decoupling controller, the initial voltage undershoots are reduced to 1.9 V and 1.8 V, respectively. The corresponding current undershoots are also reduced to 34 mA and 30 mA, respectively. The experimental results for test case 5 with the proposed decoupling controller are shown in Fig. 3.24 (b).

In test case 6, the power in V_{o4} is stepped down from 868 W to 100 W with and without the proposed decoupling controller. From the results shown in Fig. 3.25 (a), voltage overshoots of 16.5 V and 17 V are observed, and corresponding current overshoots of 232 mA and 222 mA are observed in V_{o2} and V_{o3}, respectively without decoupling control. With the prosed decoupling controller, the initial voltage overshoots are reduced to 2.3 V and 2 V, respectively. The corresponding current overshoots are also reduced to 32 mA. The experimental results with the decoupling controller are shown in Fig. 3.25 (b). Summaries of the experimental results are provided in tables 3.11, 3.12, 3.13, 3.14, 3.15, and 3.16.

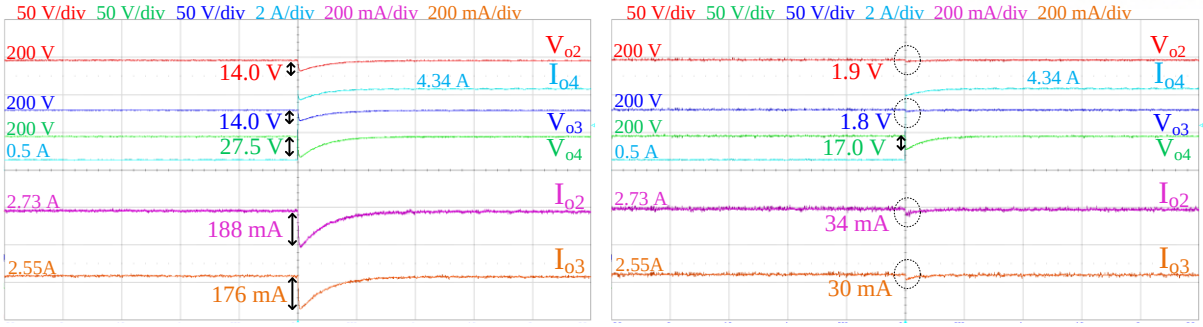

Fig. 3.24 Experimental waveforms for step down in V_{o3}: (a) without decoupling control (b) with proposed decoupling controller.

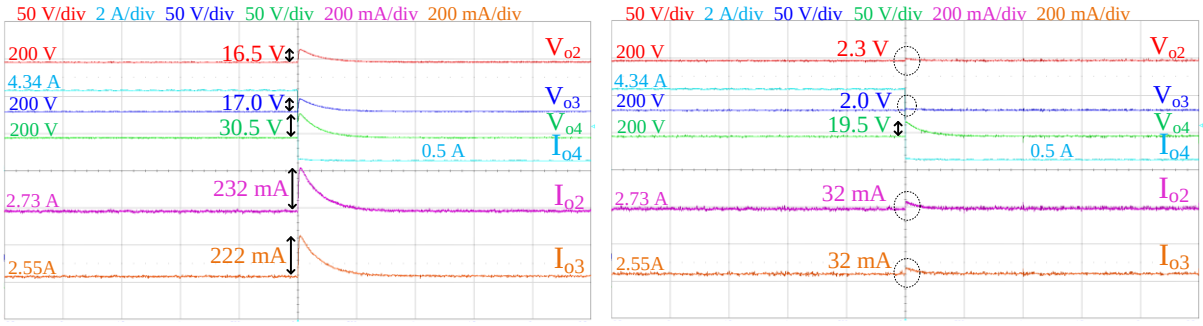

Fig. 3.25 Experimental waveforms for step down in V_{o3}: (a) without decoupling control (b) with proposed decoupling controller.

Table 3.11: Voltage experimental results for step changes in V_{o2}

Step in V_{o2}	Alternate port	Without decoupling	With decoupling	Decoupling performance
100 W – 868 W	V_{o3}	14.0 V	1.5 V	89.29 %
	V_{o4}	13.5 V	1.4 V	89.63 %
868 W – 100 W	V_{o3}	16.5 V	1.6 V	90.30 %
	V_{o4}	16.5 V	1.6 V	90.30 %

Table 3.12: Voltage experimental results for step changes in V_{o3}

Step in V_{o3}	Alternate port	Without decoupling	With decoupling	Decoupling performance
100 W – 868 W	V_{o2}	13.5 V	1.3 V	90.37 %
	V_{o4}	14.0 V	0.9 V	93.57 %
868 W – 100 W	V_{o2}	16.5 V	1.9 V	88.48 %
	V_{o4}	16.0 V	1.6 V	90.00 %

Table 3.13: Voltage experimental results for step changes in V_{o4}

Step in V_{o4}	Alternate port	Without decoupling	With decoupling	Decoupling performance
100 W – 868 W	V_{o2}	14.0 V	1.9 V	86.43 %
	V_{o3}	14.0 V	1.8 V	87.14 %
868 W – 100 W	V_{o2}	16.5 V	2.3 V	86.06 %
	V_{o3}	17.0 V	2.0 V	88.24 %

Table 3.14: Current experimental results for step changes in V_{o2}

Step in V_{o2}	Alternate port	Without decoupling	With decoupling	Decoupling performance
100 W – 868 W	I_{o3}	174 mA	22 mA	87.36 %
	I_{o4}	192 mA	16 mA	91.67 %
868 W – 100 W	I_{o3}	216 mA	28 mA	87.04 %
	I_{o4}	228 mA	24 mA	89.47 %

Table 3.15: Current experimental results for step changes in V_{o3}

Step in V_{o3}	Alternate port	Without decoupling	With decoupling	Decoupling performance
100 W – 868 W	I_{o2}	188 mA	23 mA	87.77 %
	I_{o4}	184 mA	18 mA	90.22 %
868 W – 100 W	I_{o2}	236 mA	34 mA	85.60 %
	I_{o4}	228 mA	30 mA	86.84 %

Table 3.16: Current experimental results for step changes in V_{o4}

Step in V_{o4}	Alternate port	Without decoupling	With decoupling	Decoupling performance
100 W – 868 W	I_{o2}	188 mA	34 mA	81.91 %
	I_{o3}	176 mA	30 mA	82.95 %
868 W – 100 W	I_{o2}	232 mA	32 mA	86.20 %
	I_{o3}	222 mA	32 mA	85.59 %

Table 3.17: Comparison between simulation and experimental results observed in V_{o2}

			Simulation		Experiment	
		Power Step	Without decoupling	With decoupling	Without decoupling	With decoupling
Step in V_{o3}	V	100 W – 868 W	10.96 V	0.42 V	13.5 V	1.3 V
		868 W – 100 W	11.88 V	0.38 V	16.5 V	1.9 V
	I	100 W – 868 W	137.0 mA	4.8 mA	188 mA	23 mA
		868 W – 100 W	147.3mA	5.2 mA	236 mA	34 mA
Step in V_{o4}	V	100 W – 868 W	10.90 V	0.74 V	14.0 V	1.9 V
		868 W – 100 W	11.83 V	0.69 V	16.5V	2.3 V
	I	100 W – 868 W	136.0 mA	7.7 mA	188 mA	34 mA
		868 W – 100 W	147.8 mA	8.5 mA	232 mA	32 mA

Table 3.18: Comparison between simulation and experimental results observed in V_{o3}

			Simulation		Experiment	
		Power Step	Without decoupling	With decoupling	Without decoupling	With decoupling
Step in V_{o2}	V	100 W – 868 W	10.90 V	0.37 V	14.0 V	1.5 V
		868 W – 100 W	11.85 V	0.38 V	16.5 V	1.6 V
	I	100 W – 868 W	136.9 mA	4.8 mA	174 mA	22 mA
		868 W – 100 W	147.9mA	5.1 mA	216 mA	28 mA
Step in V_{o4}	V	100 W – 868 W	11.10 V	0.62 V	14.0 V	1.8 V
		868 W – 100 W	11.86 V	0.68 V	17.0 V	2.0 V
	I	100 W – 868 W	138.0 mA	9.1 mA	176 mA	30 mA
		868 W – 100 W	148.0 mA	8.5 mA	222 mA	32 mA

Table 3.19: Comparison between simulation and experimental results observed in V_{o4}

			Simulation		Experiment	
		Power Step	Without decoupling	With decoupling	Without decoupling	With decoupling
Step in V_{o2}	V	100 W – 868 W	11.12 V	0.37 V	13.5 V	1.4 V
		868 W – 100 W	11.73 V	0.35 V	16.5 V	1.6 V
	I	100 W – 868 W	139.0 mA	4.7 mA	192 mA	16 mA
		868 W – 100 W	146.9mA	4.0 mA	228 mA	24 mA
Step in V_{o3}	V	100 W – 868 W	11.11 V	0.49 V	14.0 V	0.9 V
		868 W – 100 W	11.78 V	0.35 V	16.0 V	1.6 V
	I	100 W – 868 W	138.8 mA	6.1 mA	184 mA	18 mA
		868 W – 100 W	148.5 mA	4.5 mA	228 mA	30 mA

IV. Conclusion

In this thesis, a simple but effective power flow decoupling method is proposed in three-port and four-port dual-active-bridge (DAB) converters for DC microgrid applications. The proposed decoupling method adapts a LUT-based decoupling matrices network for dynamic decoupling of the triple-active-bridge (TAB) and quadruple-active-bridge (QAB) converters.

In section 2.1, the algorithm is designed for implementation in the TAB converter for grid-connected mode applications in DC microgrid systems. A 2 kW TAB converter prototype is developed to verify the effectiveness of the proposed decoupling controller. The proposed decoupling controller shows 98.67% and 97.92% decoupling g performance according to load variations in the lower voltage output port (V_3). The controller also shows 98.06% and 99.04% power decoupling performance according to load variations in the higher voltage output port (V_2).

In section 2.2, the proposed controller is adapted and implemented in the TAB converter for dc bus voltage regulation and TAB converter decoupling in islanding mode operation of DC microgrids. A 2 kW TAB converter prototype is developed to verify the effectiveness of the proposed decoupling controller. DC bus voltage functions according to load variations are reduced by 93.55% and 94.30% to keep the DC bus voltage within the allowable operating range. The controller shows a power decoupling performance of 98.95% and 99.00% according to load variations.

In section 3, a decoupling controller is proposed in the QAB converter for port decoupling. A 2 kW QAB converter prototype is developed to verify the effectiveness of the proposed decoupling controller. The proposed decoupling controller shows power decoupling performances of 98.65% and 98.74% in V_{o3} and power decoupling performances of 99.14% and 98.98% in V_{o4} according to load variations in V_{o2}. The controller also shows power decoupling performances of 98.82 and 98.34% in V_{o2} and power decoupling performances of 99.37% and 98.68% in V_{o4} according to load variations in V_{o3}. Finally, the proposed decoupling controller shows power decoupling performances of 97.55% and 98.08% in V_{o2} and power decoupling performances of 97.80% and 98.30% in V_{o3} according to load variations in V_{o4}. Simulation and experimental results show the effectiveness of the proposed decoupling controller in three-port and four-port dual-active-bridge converters for DC microgrid applications.

REFERENCES

1. Buraimoh, E.; Davidson, I.E.; Martinez-Rodrigo, F. Fault Ride-Through Enhancement of Grid Supporting Inverter-Based Microgrid Using Delayed Signal Cancellation Algorithm Secondary Control. Energies 2019, 12, 3994. https://doi.org/10.3390/en12203994 C. P. Steinmetz, "On the Law of Hysteresis," in Transactions of the American Institute of Electrical Engineers, vol. IX, no. 1, pp. 1-64, Jan. 1892.

2. Rohit R. Deshmukh and Makarand S. Ballal. (2020). Integrated control scheme for dynamic power management with improved voltage regulation in DC microgrid. Journal of Power Electronics, 20(6), 1550-1561

3. Han, M., Liu, X., Pu, H. et al. Real-time online optimal control of current-fed dual active bridges based on machine learning. J. Power Electron. 20, 43–52 (2020). https://doi.org/10.1007/s43236-019-00013-6

4. Tomar, A., Gaur, P., Kandari, R., & Gupta, N. (2021). *Control of standalone microgrid*. Elsevier Science et Technology.

5. Sim, J., Lee, JY & Jung, JH. Isolated three-port DC-DC converter employing ESS to obtain voltage balancing capability for bipolar LVDC distribution system. J. Power Electron. J. Power Electron.20, 802-810(2020).https://doi.org/10.1007/s43236-02000065-z

6. Liu, D. Zhu, J. Zhang, H. Liu and G. Cai, "A Bidirectional Dual Buck-Boost Voltage Balancer with Direct Coupling Based on a Burst-Mode Control Scheme for Low-Voltage Bipolar-Type DC Microgrids," Journal of Power Electronics, vol. 15, no. 6, pp. 1609-1618, 2015. DOI: 10.6113/JPE.2015.15.6.1609.

7. J. Sim, J. Lee, H. Choi and J. -H. Jung, "High Power Density Bidirectional Three-Port DC-DC Converter for Battery Applications in DC Microgrids," 2019 10th International Conference on Power Electronics and ECCE Asia (ICPE 2019 - ECCE Asia), 2019, pp. 843-848,doi:10.23919/ICPE2019ECCEAsia42246.2019.8797043.

8. Liu, Ran. (2018). A Novel Decoupled TAB Converter with Energy Storage System for HVDC Power System in More Electric Aircraft. The Journal of Engineering. 2018. 10.1049/joe.2018.0033

9. P. Wang, X. Lu, W. Wang and D. Xu, "Hardware Decoupling and Autonomous Control of Series-Resonance-Based Three-Port Converters in DC Microgrids," in IEEE Transactions on Industry Applications, vol. 55, no. 4, pp. 3901-3914, July-Aug. 2019, doi: 10.1109/TIA.2019.2906112.

10. C. Zhao, S. D. Round and J. W. Kolar, "An Isolated Three-Port Bidirectional DC-DC Converter with Decoupled Power Flow Management," in IEEE Transactions on Power Electronics, vol. 23, no.5, pp. 2443-2453, Sept. 2008, doi: 10.1109/TPEL.2008.2002056.

11. L. Wang, Z. Wang and H. Li, "Asymmetrical Duty Cycle Control and Decoupled Power Flow Design of a Three-port Bidirectional DC-DC Converter for Fuel Cell Vehicle Application," in IEEE Transactions on Power Electronics, vol. 27, no. 2, pp. 891-904,

12. I. Bisis, D. Kastha and P. Bajpai, "Small Signal Modeling and Decoupled Controller Design for a Triple Active Bridge Multiport DC–DC Converter," in IEEE Transactions on

Power Electronics, vol. 36, no. 2, pp. 1856-1869, Feb. 2021, doi: 10.1109/TPEL.2020.3006782.

13. Tao, H. (2008). Integration of sustainable energy sources through power electronic converters in small distributed electricity generation systems (dissertation). Technische Universiteit Eindhoven.

14. M. Michon, J. L. Duarte, M. Hendrix, and M. G. Simoes, "A three-portbi-directional converter for hybrid fuel cell systems," in Proc. IEEE Power Electronics Specialists Conference (PESC'04), Aachen, Germany, Jun. 2004,pp. 4736–4742.

15. Albertos, P. and Sala, A., 2010. *Multivariable control systems*. London: Springer.

16. K. Katagiri, K. Nishimoto, S. Nakagawa, S. Okutani, Y. Kado and K. Wada, "Decoupling Power Flow Control of Triple-Active Bridge Converter with Voltage Difference between Each Port for Distributed Power Supply System," 2018 20th European Conference on Power Electronics and Applications (EPE'18 ECCE Europe), 2018, pp. P.1-P.9.

17. K. Vangen, T. Melaa, and A. K. Adnanes, Soft-switched high-frequency, high power DC/AC converter with IGBT,in Proc. IEEE Power ElectronicsSpecialists Conference (PESC'92), Jun. 1992, pp. 26–33.

18. Y. Kado, R. Kasashima, N. Iwama, and K. Wada, "Implementation and Performance of Three-way Isolated DC/DC Converter using SiC-MOSFETs for Power Flow Control," *Proc. IEEE Int. Power Electronics for Distributed Generation Systems Conf.*, 2016, DOI: 10.1109/PEDG.2016.7527102

19. I. Kim, J.-Y. Sim, J.-Y. Lee, and J.-H. Jung, "Power Decoupled Multi-Port Dual-Active-Bridge Converter Employing Multiple Transformers for DC Distribution Applications," The Transactions of the Korean Institute of Power Electronics, vol. 25, no. 4, pp. 286–292, Aug. 2020.

20. R. W. Erickson and D. Maksimovic, "A multiple-winding magnetics model having directly measurable parameters," PESC 98 Record. 29th Annual IEEE Power Electronics Specialists Conference (Cat. No.98CH36196), 1998, pp. 1472-1478 vol.2, doi: 10.1109/PESC.1998.703254.

21. M. Qiang, W. Wei-yang and X. Zhen-lin, "A Multi-Directional Power Converter for a Hybrid Renewable Energy Distributed Generation System with Battery Storage," 2006 CES/IEEE 5th International Power Electronics and Motion Control Conference, 2006, pp. 1-5, doi: 10.1109/IPEMC.2006.4778337.

22. W.L.Luyben,"Distillationdecoupling,"AIChE,vol.16,no.2,pp.198–203,Mar.1970.

23. C. Yoo, W. Choi, I. Chung, D. Won, S. Hong and B. Jang, "Hardware-in-the-loop simulation of DC microgrid with Multi-Agent System for emergency demand response," 2012 IEEE Power and Energy Society General Meeting, 2012, pp. 1-6, doi: 10.1109/PESGM.2012.6345678.

24. N. Zhi, H. Zhang and X. Xiao, "Switching system stability analysis of DC microgrids with DBS control," 2016 IEEE Applied Power Electronics Conference and Exposition (APEC), 2016, pp. 3338-3345, doi: 10.1109/APEC.2016.7468346.

25. T. Wu, C. Kuo, L. Lin and Y. Chen, "DC-Bus Voltage Regulation for a DC Distribution System With a Single-Phase Bidirectional Inverter," in IEEE Journal of Emerging and Selected Topics in Power Electronics, vol. 4, no. 1, pp. 210-220, March 2016, doi: 10.1109/JESTPE.2015.2485300.

26. J. S. Morton, "Circuit Breaker and Protection Requirements for DC Switchgear used in Rapid Transit Systems," in IEEE Transactions on Industry Applications, vol. IA-21, no. 5, pp. 1268-1273, Sept. 1985, doi: 10.1109/TIA.1985.349553.

27. Chuanhong Zhao and J. W. Kolar, "A novel three-phase three-port UPS employing a single high-frequency isolation transformer," 2004 IEEE 35th Annual Power Electronics Specialists Conference (IEEE Cat. No.04CH37551), 2004, pp. 4135-4141 Vol.6, doi: 10.1109/PESC.2004.1354730.

28. P. Falb and W. Wolovich, "Decoupling in the design and synthesis of multivariable control systems," in IEEE Transactions on Automatic Control, vol. 12, no. 6, pp. 651-659, December 1967, doi: 10.1109/TAC.1967.1098737.

29. Gilbert, Elmer G. “The Decoupling of Multivariable Systems by State Feedback.” *SIAM Journal on Control*, vol. 7, no. 1, Feb. 1969, pp. 50–63, 10.1137/0307004. Accessed 7 June 2022.

30. Levine, W S. The Control Systems Handbook: Control System Advanced Methods, Second. Boca Raton, Fla., Crc Press, 2018.

ACKNOWLEGEMENT

I would like to show my deepest appreciation to my advisor Prof. Jee-Hoon Jung for his invaluable assistance and guidance throughout my Master's degree program. I am grateful for his patience and vital feedback that has led to the success of this thesis. I would also like to show my gratitude to Prof. JinGook Kim and Prof. Se-Un Shin for being a part of my defense committee and for their invaluable feedback that helped me improve this thesis. I would also like to show my gratitude to Prof. Katherine Kim for believing in me and offering her continuous support in my tertiary education journey.

Special thanks to my seniors, Dr. Mina Kim and Kyung-Wook Heo for their unflinching support throughout my master's degree program. To my labmates, Chano Jeon, Chang-Woo Yun and, Hyunji Kim, I say thank you for the various assistance given during my research process.

Finally, I am highly grateful to my parents and siblings for believing in me and providing all the necessary support for my academic journey. I would also like to express my profound gratitude to Dr. Emmanuel Osa Noi-Sanar for his unending support and encouragement and to Bruno Andreis for his invaluable support.

APPENDIX

A) Graph of approximations for quadratic term simplification

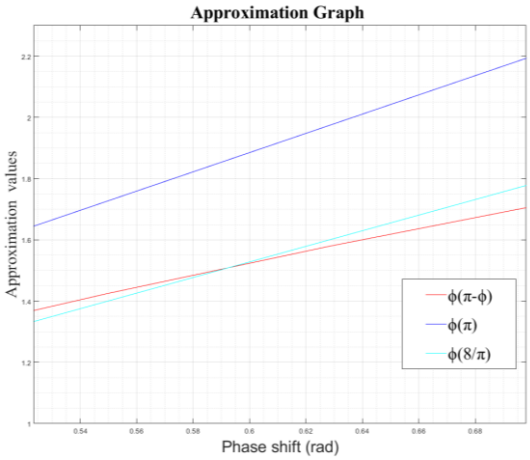

B) Simulation comparisons between the proposed decoupling method and the conventional method

Section 2:

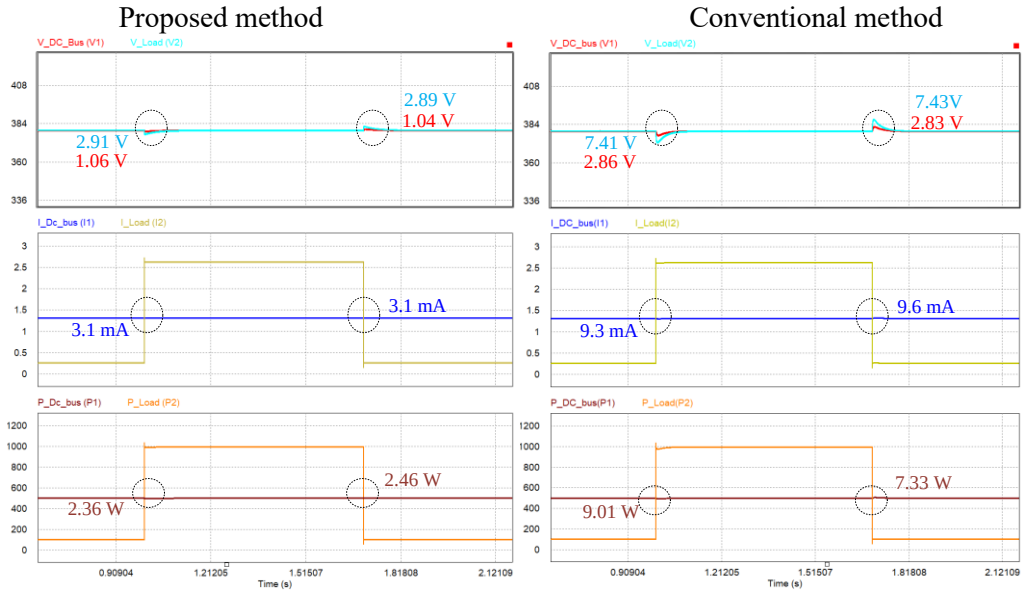

	Performance Metrics	Proposed Method		Conventional Method	
		V_2 (load)	**V_1 (DC bus)**	**V_2 (load)**	**V_1 (DC bus)**
Power Step in V_2	Voltage undershoot	2.91 V	1.06 V	7.41 V	2.86 V
	Settling time	1.29 E-001	5.81 E-002	1.31 E-001	6.49 E-002
	Voltage overshoot	2.89 V	1.04 V	7.43 V	2.83 V
	Settling time	1.32 E-001	6.27 E-002	1.37 E-001	6.75 E-002

Section 2.1	Performance Metrics	Proposed Method		Conventional Method	
		V_2	V_3	V_2	V_3
Power Step in V_2	Voltage undershoot	4.12 V	0.35 V	8.67 V	0.95 V
	Settling time	4.29 E-002	2.49 E-002	1.61 E-001	8.97 E-002
	Voltage overshoot	4.07 V	0.26 V	8.86 V	1.02 V
	Settling time	4.58 E-002	2.99 E-002	1.37 E-001	7.97 E-002
Power Step in V_3	Voltage undershoot	2.63 V	16.45 V	4. 22 V	20.12 V
	Settling time	3.15 E-002	1.32 E-001	1.57 E-001	1.52 E-001
	Voltage overshoot	2.76 V	17.23 V	4.36 V	23.05 V
	Settling time	4.29 E-002	9.49 E-002	1.61 E-001	1.51 E-001

Section 3:

Proposed method

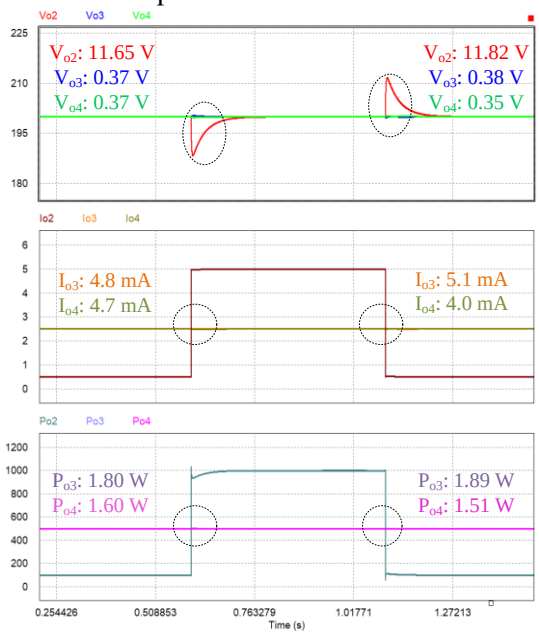

Conventional method

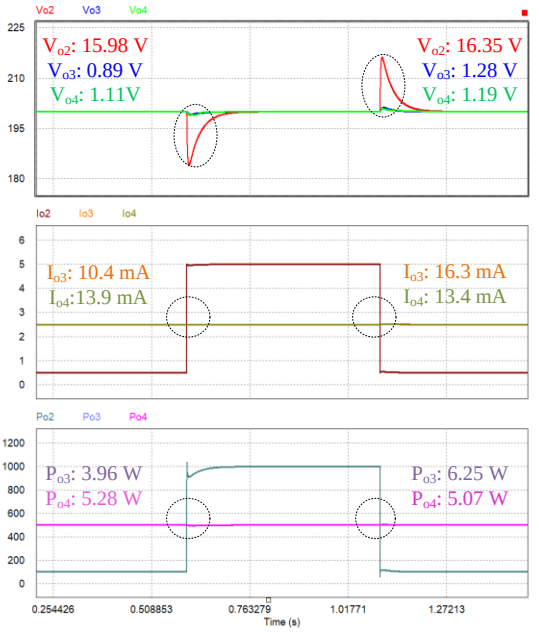

	Performance Metrics	Proposed Method			Conventional Method		
		V_{o2}	V_{o3}	V_{o4}	V_{o2}	V_{o3}	V_{o4}
Power Step in V_{o2}	Voltage undershoot	11.65 V	0.37 V	0.37 V	15.98 V	0.89 V	1.11 V
	Settling time	1.03E-001	3.54 E-002	3.54 E-002	1.51 E-001	4.54 E-002	6.29 E-002
	Voltage overshoot	11.82 V	0.38 V	0.35 V	16.35 V	1.28 V	1.19 V
	Settling time	1.53E-001	3.54 E-002	3.47 E-002	1.53 E-001	5.24 E-002	5.17 E-002
Power Step in V_{o3}	Voltage undershoot	0.42 V	11.64 V	0.49 V	0.85 V	15.95 V	1.13 V
	Settling time	4.54E-002	1.03 E-001	4.78 E-002	4.54 E-002	1.51 E-001	6.54 E-002
	Voltage overshoot	0.38 V	11.85 V	0.35 V	1.31 V	16.32 V	1.10 V
	Settling time	3.54E-002	1.11 E-001	3.47 E-002	6.54 E-002	1.52 E-001	6.54 E-002
Power Step in V_{o4}	Voltage undershoot	0.74 V	0.62 V	13.59 V	1.12 V	1.11 V	17.22 V
	Settling time	5.53E-002	5.44 E-002	1.26 E-001	6.53 E-002	6.54 E-002	1.55 E-001
	Voltage overshoot	0.69 V	0.68 V	13.78 V	1.24 V	1.32 V	17.33 V
	Settling time	4.12E-002	4.23 E-001	6.53 E-002	6.53 E-002	6.54 E-002	1.56 E-001